

AD-A181 092

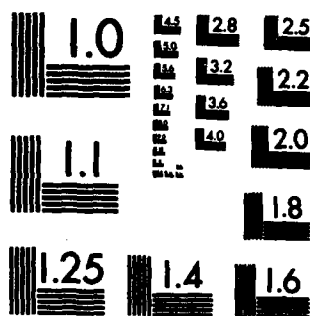
DETERMINISTIC AND STOCHASTIC WAVEFIELD IN THE
NEAR-FIELD FROM EXPLOSIVE S. (U) SOUTHERN METHODIST
UNIV. DALLAS TX DEPT OF GEOLOGICAL SCIENCES..
B W STUMP ET AL. 03 APR 87 SMUG-3

1/3

UNCLASSIFIED

F/G 8/11

NL



MICROCOPY RESOLUTION TEST CHART
NATIONAL BUREAU OF STANDARDS-1963-A

SECURITY CLASSIFICATION OF THIS PAGE

RESTRICTIVE MARKING PAGE

AD-A181 092 DTIC
SELECTED

15. RESTRICTIVE MARKING

DTIC FILE COPY 2

3. DISTRIBUTION/AVAILABILITY OF REPORT

Approved for public release,
distribution unlimited

4. PERFORMING ORGANIZATION REPORT NUMBER

SMUG-3

JUN 05 1987

5. MONITORING ORGANIZATION REPORT NUMBER(S)

AFOSR-TR-87-0004

6a. NAME OF PERFORMING ORGANIZATION

Southern Methodist Univ.
Dept. of Geological Sciences6b. OFFICE SYMBOL
(If applicable)

X

7a. NAME OF MONITORING ORGANIZATION

AFOSR

6c. ADDRESS (City, State, and ZIP Code)

Southern Methodist University
Department of Geological Sciences
Dallas, Tx. 75275

7b. ADDRESS (City, State, and ZIP Code)

Same as 8c.

8a. NAME OF FUNDING/SPONSORING
ORGANIZATION

AFOSR/NP

8b. OFFICE SYMBOL
(If applicable)

NP

9. PROCUREMENT INSTRUMENT IDENTIFICATION NUMBER

AFOSR-84-0016

8c. ADDRESS (City, State, and ZIP Code)

AFOSR/NP
Building 410
Bolling AFB, DC 20332

10. SOURCE OF FUNDING NUMBERS

PROGRAM
ELEMENT NO.PROJECT
NO.TASK
NO.WORK UNIT
ACCESSION NO.

101102F

2309

A1

11. TITLE (Include Security Classification)

Deterministic and Stochastic Wavefield in the Near-Field from Explosive
Sources" (U)

12. PERSONAL AUTHOR(S)

Brian W. Stump, Robert E. Reinke, Elizabeth C. Flynn

13a. TYPE OF REPORT

Annual

13b. TIME COVERED

FROM 15 Oct 85 TO 14 Oct 86

14. DATE OF REPORT (Year, Month, Day)

87 4 3

15. PAGE COUNT

107

16. SUPPLEMENTARY NOTATION Seismology, explosion source, moment tensors, elastic wave
propagation, body waves, surface waves, source depth effects, scatter-
ing, superposition.

17. COSATI CODES

FIELD GROUP SUB-GROUP

18. SUBJECT TERMS (Continue on reverse if necessary and identify by block number)

Seismology; scattering; moment tensors

19. ABSTRACT (Continue on reverse if necessary and identify by block number)

Work in four areas is reported. The first deals with the design and implementation of small scale chemical explosions for the purposes of constraining the physical characteristics of the equivalent elastic source. The second major area of work is the experimental quantification of the effect of source depth in generating body and surface waves in the near-field. The third contribution reports attempts to determine the effect of scattering on near-field waveforms. A geological site characterization procedure is proposed. Finally, superposition experiments for two identical explosive sources separated by 147 m/at 1/3 are described.

Keywords:

20. DISTRIBUTION/AVAILABILITY OF ABSTRACT

☒ UNCLASSIFIED/UNLIMITED ☐ SAME AS RPT.☒ DTIC USERS

21. ABSTRACT SECURITY CLASSIFICATION

UNCLASSIFIED

22a. NAME OF RESPONSIBLE PERSONAL

22b. TELEPHONE (Include Area Code) 22c. OFFICE SYMBOL

AFOSR-TN- 87-0694

**AIR FORCE OFFICE OF SCIENTIFIC RESEARCH (AFSC)
NOTICE OF TRANSMITTAL TO DTIC**

**This technical report has been reviewed and is
approved for public release IAW AFR 190-12.
Distribution is unlimited.**

**MATTHEW J. KERPER
Chief, Technical Information Division**

**Approved for public release;
distribution unlimited.**

INTERIM SCIENTIFIC REPORT

Grant AFOSR -84-0016

Brian W. Stump

Department of Geological Sciences

Southern Methodist University

Dallas, Texas 75275

For the Period 1 Oct. 85 - 1 Oct. 86

Accession For	
NTIS CRA&I	<input checked="checked" type="checkbox"/>
DTIC TAB	<input type="checkbox"/>
Unannounced	<input type="checkbox"/>
Justification	
By	
Distribution /	
Availability Codes	
Dist	Avail and/or Special
A1	



Table of Contents

- 1. Introduction**
- 2. Experimental Seismology: In Situ Source Experiments**
- 3. Mathematical Representation and Physical Interpretation of a Contained Chemical Explosion in Alluvium**
- 4. Effects of Source Depth on Near Source Seismograms**
- 5. Stochastic Geologic Effects on Near-Field Ground Motions in Alluvium**
- 6. Experimental Confirmation of Superposition from Small Scale Explosions**

INTRODUCTION

During the course of the past year work has progressed in four distinct areas. The first has dealt with the utilization of experiments designed to quantify the effects of explosive sources in generating ground motions. Two papers which have been accepted for publication in the Bulletin of the Seismological Society of America summarize these results (1) Experimental Seismology: In Situ Source Experiments and (2) Mathematical Representation and Physical interpretation of a Contained Explosion in Alluvium.

The second area of work has quantified the effect of source depth on the generation of body and surface waves in the near-field. A paper has been submitted to the Journal of Geophysical Research and is entitled: Effects of Source Depth on Near Source Seismograms.

Experimental techniques for quantifying the stochastic effects of geological structure on near-field ground motions are reported in: Stochastic Geologic Effects on Near-Field Ground Motions in Alluvium (submitted to Bulletin of the Seismological Society of America).

Finally experimental evidence for superposition of ground motion from two explosive charges spaced as closely as $147 \text{ m/kt}^{1/3}$ is reported in: Experimental Confirmation of Superposition from Small Scale Explosions (submitted Bulletin of the Seismological Society of America).

The digital data analysis package, slopcor, which is used for data display and study (reported on last year) has been implemented on the HP-9000 at AFWL/NTES, Kirtland AFB, New Mexico. Products of this research has been made operational for this AF installation.

Ongoing work continues in establishing scaling relations for small scale chemical explosions. A second graduate student project is extending the stochastic site characterization work to new geological media. A third graduate student is investigating the use of surface waves in the near-field in constraining near surface shear wave velocities.

**EXPERIMENTAL SEISMOLOGY:
IN SITU SOURCE EXPERIMENTS**

**Brian W. Stump
Department of Geological Sciences
Southern Methodist University
Dallas, Texas 75275**

**Robert E. Reinke
Air Force Weapons Laboratory/NTESG
Kirtland AFB, New Mexico 87117-6008**

ABSTRACT

The utility of small-scale chemical explosion experiments in characterizing the seismic source is explored. An experiment using a 253 lb. TNT charge detonated at a depth of 11.5 m was designed to address: (1) The importance of free surface interactions on the explosion source function; (2) The source characterization of chemical explosions; (3) The separation of isotropic and deviatoric source components; and (4) The utility of motion data from within the linear and non-linear regime. The initial P pulse from the explosion grows from a rise time of 25 ms at $82 \text{ m/kt}^{1/3}$ to 50 ms at $215 \text{ m/kt}^{1/3}$. The corner frequency of the linear data ($992\text{--}2976 \text{ m/kt}^{1/3}$) is approximately 20 Hz. The interaction of the initially spherical wavefront with the free surface results in spall. This non-linear process redistributes energy into the 5 Hz band and appears as a spectral peak for ranges greater than $992 \text{ m/kt}^{1/3}$. Transverse motions at ranges greater than $992 \text{ m/kt}^{1/3}$ were 3 to 35 percent of the radial and vertical accelerations. The radial and vertical motions changed little with azimuth supporting a cylindrically symmetric source.

INTRODUCTION

Controlled small scale in situ explosive experiments provide an opportunity to isolate and study individual aspects of the seismic source-propagation problem. Inferences placed upon the seismic source are dependent on a wide range of phenomenology. These phenomena include wave propagation effects such as generation of body and surface waves, attenuation, dispersion, and scattering. Near source media properties, source depth, source temporal characteristics, and source spatial finiteness also contribute to the observed seismograms. Small scale chemical explosion tests can be designed to study individual aspects of the source-propagation problem. In this manner a single phenomenon can be isolated and explored.

This paper addresses the range of explosion source phenomenology which can be studied by means of small scale field tests as well as procedures for test design and implementation. One particular test will be discussed in detail. This test was designed to address the following: (1) The importance of free surface interactions on the explosion source function; (2) The characterization of chemical explosions; (3) The separation of isotropic and deviatoric source components in a medium with well calibrated propagation effects; and (4) The utility of motion

data from within the non-linear and linear regime in
interpretating the seismic source function.

The linear and non-linear wave fields resulting from this small
scale test will be displayed and the resulting constraints upon
the source model determined. A companion paper (Stump, 1987
referred to as Paper II) discusses the modeling of the observed
wave field, preferred source model, and comparisons with other
sources including large nuclear explosions.

SOURCE PHENOMENOLOGY

Small scale experimental source studies provide the potential for isolating the many factors which contribute to the observed waveforms. These factors include the transition from the non-linear to linear motion regimes, dynamic material properties of the emplacement medium, stochastic effects, finite spatial source effects and interaction of the initial wavefront with the free surface.

One of the most important questions to be addressed when studying explosions is identification of the region where the transition from non-linear to linear motion occurs. The determination of the equivalent elastic source function is critically dependent upon identification of the range at which this transition occurs.

Trulio (1978) and Larson (1982) carefully addressed this problem in salt by means of field and laboratory experiments and concluded that whole space linear elastic decay is not observed within a range of $250\text{m}/\text{kt}^{1/3}$. Simultaneous with this observation, Larson finds that linear superposition holds at a scaled range of $168\text{ m}/\text{kt}^{1/3}$. Stump and Reinke (1987) show from analysis of a small scale field test that superposition holds in alluvium at a scaled range of $147\text{ m}/\text{kt}^{1/3}$.

Dynamic material properties of the emplacement medium are an important governing factor in the behavior of the equivalent elastic source region. Historically, in situ chemical explosions have been used to determine dynamic geologic material properties

(Crawford et.al., 1986; Rinehart, 1985). Small to intermediate scale chemical explosions can be conducted in different materials to improve the quantification of the effects of material type on the source characterization (Mueller and Murphy, 1971; Murphy, 1977; and Werth and Herbst, 1963).

Source burial depth has a significant influence on the radiated seismic energy. For shallow source depths the explosion vents, releasing some of the energy to the atmosphere. A deeper contained explosion couples more energy into the ground. McLaughlin et al (1985) quantified the effects of source depth on body wave magnitudes for nuclear cratering events. Flynn (1986) examined data from a suite of chemical explosions in alluvium and determined the relative and absolute coupling of energy into body and surface waves as a function of source depth. Similar tests in other media could further constrain these source depth effects.

Explosion source models as they now exist are purely parametric. Questions concerning source repeatability with separation of stochastic and deterministic effects have been discussed only briefly (McLaughlin, 1982; Reinke and Stump, 1987). Further studies employing ensembles of small scale field experiments could yield additional insight into these questions.

C The explosive source is most often modeled as a point source in space with a finite temporal characterization. In many cases spatial finiteness may become important in the source representation. Evidence for finite spatial source effects in the

seismic signal excited by quarry blasts has been presented by Greenhalgh (1980). The two-burst experiments reported by Stump and Reinke (1987) are an initial attempt to determine the importance of these effects. Higgins et al (1978) utilized finite arrays of explosives as simulators of propagating earthquake faults. The ground motions produced by these simulators were used to exercise scale model structures.

Small field experiments offer the opportunity to separate up and down going energy from the source with appropriate gage locations. In particular, the interaction of the upgoing compressive wave with the free surface and the resulting tensile failure of the near surface material can be quantified. Since this spall phenomenon is dependent upon the material tensile strength, its relative importance will vary with geology. (Viecelli, 1973; Sobel, 1978; Stump and Reinke, 1984)

In a carefully controlled test the propagation path effects can be isolated and trade-offs between source and propagation path minimized. The ability to control the experiment prevents the misinterpretation of such trade-offs. Small scale explosions can be used to identify the relative importance of deviatoric and isotropic source contributions (Masse, 1981). Experiments can be designed so that driven motions along planes of weakness can be separated from tectonic strain release.

EXPERIMENTAL DESIGN

A small scale contained explosion test in alluvium named CHEAT (Contained High Explosive Alluvium Test) was conducted at a test site with a well constrained P wave velocity structure so that source and propagation path trade-offs could be minimized. The experiment was designed to study the following : (1) Free surface interactions and their relation to spall effects; (2) Seismic source effects of chemical explosions; (3) The relative importance of isotropic and deviatoric source components; and (4) The utility of motion data from within the linear and non-linear regimes.

The large scale of most nuclear test events precludes adequate gage placement for the characterization of both the linear and non-linear motion regimes in three dimensions. In a small scale chemical explosion the complete motion field may be economically instrumented. Such experiments may be performed in a wide variety of geologies. Differences do exist in the source physics for chemical and nuclear sources. In a chemical explosion the explosive by-products from the chemical reaction raise the cavity pressure and couple energy into the surrounding material. Nuclear explosions generate large quantities of thermal energy and x-rays which are both deposited into the emplacement medium leading to the generation of cavity pressure and ground motion (Rodean, 1981). For both the chemical and nuclear cases these processes are complete after the first few microseconds of the

event. The phenomenology which follows, including non-linear material response, non-isotropic effects, and free surface interactions is similar for both source types.

The test instrumentation for CHEAT was divided into two distinct arrays - one close-in to the source and one in the linear region. The close-in array consisted of a radial set of accelerometers (Figure 1). At the three meter range, gages were placed at three azimuths to determine the degree of source symmetry (Figure 2). The objectives of this close-in array were to quantify the initial coupling of the explosion into the alluvium and to investigate the interaction of the initially compressive pulse with the free surface. This interaction with the free surface results in spall (Rinehart, 1959) and a repartitioning of the energy present in the initially spherical, minimum phase wavelet. Gages were placed to determine the depth, range, and symmetry of this process.

A cross sectional diagram for the CHEAT close-in gages is shown in Figure 1. A plan view of the gage locations is shown in Figure 2. Each solid triangle represents a radial and vertical accelerometer. The open triangles indicate where single vertical accelerometers were placed. The gage cannisters were placed in boreholes and then filled with uniformly rained sand. The emplacement of gages within drill holes is a process that has been studied by many authors. In alluvial material, for relatively low accelerations ($<50g$), it has been shown that gages placed in rained sand respond the same as gages cemented in place

with grout which approximately matches the in situ material properties (Ake, 1980). The raining technique yields densities for the sand within the borehole which closely match those of the surrounding material. Based upon these results, the rained sand gage placement technique was used for all gages within the non-linear zone. The gages used in this array were piezoresistive accelerometers flat in acceleration response to 750 Hz. The signals produced by the gages were recorded on high speed analog tape drives and later digitized. The data from within a scaled range of $364 \text{ m/kt}^{1/3}$ were digitized at 5000 samples per second after application of a 5-pole Butterworth filter at 1250 Hz.

The gage array in the linear regime ($992 \text{ m/kt}^{1/3}$ to $2976 \text{ m/kt}^{1/3}$) was designed to yield both azimuthal and range data for the purpose of characterizing the equivalent elastic source in terms of moment tensors (Stump and Johnson, 1984). The station representation was selected after an exploration of covariance matrices associated with the source representation. The station distribution shown in Figure 3 yields a condition number for source inversions near 50 which is found acceptable for model determination under moderate noise conditions (Stump, 1986). Other source expansions such as the spherical harmonic representation of Workman et al (1981) may require a different station distribution. Utilizing covariance and resolution matrices in the array design allows the quantification of error propagation in these studies. Each solid triangle in Figure 3 represents a three-component force balance accelerometer. The instruments were flat to acceleration between 0.02 to 50 Hz. The gages were placed

in holes 15 cm deep which were then backfilled with native soil. Signals from the accelerometers were recorded by digital event recorders at a rate of 200 samples per second with a 5-pole Butterworth filter applied at 50 Hz.

The acceleration waveforms from both arrays of gages were integrated during post test processing to yield velocity. During this integration procedure, the accelerations were corrected for a static offset which would appear as a ramp in velocity. No additional corrections were required. The two gage arrays gave a total of 81 possible motion measurements from the experiment.

The charge used in this experiment was a 253 pound sphere of TNT 0.51m in diameter. The charge was placed at a depth of 11.5 m and the emplacement hole was backfilled with sand. In order to make comparisons between the nuclear and chemical sources it is necessary to determine the rate and degree of symmetry for the explosive burn. The standard burn rate for TNT is 6097 m/sec giving an estimated detonation time of 42 μ s. In order to check the accuracy of this estimate for the charge configuration used in the CHEAT experiment a number of similar TNT spheres were instrumented with time of arrival crystals which break when the explosive front reaches them. The data from these crystals for a 1000 pound TNT sphere are given in Figure 4. Subtracting the 8.7 μ s required for the crystal to break, the observed burn time for the sphere is 55.8 μ s with a 2.8 μ s variation across the sphere. This variation is only 4% of the mean burn time for the sphere validating the spherical symmetry of the explosive source.

OBSERVATIONAL DATA

An overview of the observational data set provides a pictorial view of the various physical processes associated with the explosion source. The waveforms obtained in the non-linear zone are particularly instructive in separating the various contributions to the seismograms recorded in the elastic region. Forty-five of the 48 gages fielded in the region bounded by 364 $\text{m/kt}^{1/3}$ provided useable data.

The waveform in Figure 5 from the closest gage to the explosion ($82.97 \text{ m/kt}^{1/3}$) illustrates the initial P pulse from the source. The acceleration, velocity and displacement traces are shown. The reflection from the free surface is apparent after the arrival of the direct P pulse. The displacement rise time is approximately 25 ms with an apparent overshoot.

The vertical propagation of the P wave, its surface reflection, and the tensile failure of the near surface material are all illustrated in Figure 6. Acceleration data recorded from previous surface explosions at this site had exhibited spall phenomena which were not a result of the classic free-surface tensile reflection (Stump and Reinke, 1984). However, one can see in this figure that the spall occurs first nearest the free surface and then propagates down into the material consistent with a free surface tensile reflection model. The characteristic minus one g dwell is difficult to discern at the scale of Figure 6 so the shallowest gage is reproduced in larger scale in Figure 7. At

this range the material is in free fall for 130-150 ms. Spall rejoin is seen to occur first at depth and propagate to the free surface as expected from the increased overburden stress with depth. Growth of the initial P wave pulse width as it propagates vertically is also evident in the set of data shown in Figure 6.

Utilizing criteria given by Stump and Reinke (1984) the spall zone surrounding the CHEAT explosion was delineated. The gage locations where spall behavior was observed are given by solid circles in Figure 8. The primary criteria used to determine if spall had occurred at a particular accelerometer location were: (1) Minus one g (-0.5 to -2.0 g) dwell on vertical records; (2) Impulsive rejoin signals on all components; and (3) No horizontal acceleration dwell (<0.2g). With these criteria, the spall zone is found to extend horizontally to between 10.85 and 18.35 m and to depths of between 4.3 and 7.5 m. The average dwell times measured from the velocity records are given in Figure 8 along with the peak velocity prior to tensile failure. The dwell times are largest directly above the explosion near the free surface and diminish away from this point. Similarly, the related escape velocity is also greatest directly above the explosion. This set of observational data has been used to constrain the mass and momentum captured by the spall process (Stump, 1985). The resulting estimates are :

$$M = 2.73 \text{ to } 4.20 \times 10^6 \text{ kg}$$

$$I = M V = 1.45 \text{ to } 2.23 \times 10^{11} \text{ dyne-cm}$$

where M is mass, V is velocity and I is momentum

The finite spatial extent of the spall process and the fact that spall initiation and termination times vary spatially results in a smooth seismic source time function estimates (Stump, 1985). Thus the non-linear data allow the quantification of one aspect of the seismic source - spall. The relative importance of the process is dependent on the spall time function.

The spall mass and momentum estimates made above assume azimuthal symmetry. The three vertical records at the 3 m range support this symmetry assumption (Figure 9). At this range, the P wave peak accelerations are 9.3, 9.1 and 9.1 gs. The P pulse widths are 19, 16 and 15 ms as measured on the accelerograms. The spall dwell times are measured to be 123, 126 and 121 ms. The spall initiation times are 38, 33 and 32 ms.

The velocity and displacement records for the vertical and radial gages at the 1, 3, 6.5 and 10.85 m ranges, 0.23 m depth, are shown in Figure 10. These records document the development of the explosion pulse as it propagates. The proximity of these accelerometers to the free surface means that these pulses will include interactions of the explosion generated waves with the free surface including spall. No corrections have been made to the data prior to or during the integration procedure, thus accounting for the long period drift observed in several displacement records.

The dotted lines on each vertical record in Figure 10 indicate the estimated spall dwell time. At the 1 m range (0.23 m depth) the maximum spall dwell time occurs with a displacement pulse

width of 180-190 ms. This pulse width is controlled by the total time material was in free fall anywhere within the test bed. This point is substantiated by the fact that the displacement pulse width remains constant as one moves radially away from ground zero and down in depth despite the fact that the dwell time of spall decreases. At the 1 m range and 7.5 m depth, no spall occurs but the displacement pulse width remains at 190 ms. Similar results hold for the 18.35 m range data.

Within the spall zone, the vertical velocity records can be characterized by the initial rise time of the P pulse, followed by free fall, ending with rejoin. Moving out of the spall zone, the velocity field is characterized by a P pulse width near 50 ms followed by a negative dwell approximately 150 ms in length. This interpretation leads to a source wavelet with a displacement rise time of 50 ms (compared to an initial rise time of 25 ms) followed by the longer period phenomenon indicative of energy imparted to the material from spall (Figure 11). This pulse construction clearly illustrates the role of the initial compressive wave and the spall phenomenon in the equivalent elastic source. This interpretation is further strengthened when a comparison of the velocity pulse at 18.3 m is made with the far-field source function determined from the inversion of the observational data at 50-150 m (Paper II).

Moving into the linear regime, the array data portrayed in Figure 3 are summarized. Of the 33 instruments in this array, 28

provided useable data. All components were lost at station 9 while vertical records were not obtained at stations 4 and 6.

Figure 12, which shows the radial and vertical accelerograms for the three stations at the 50 m range, illustrates the symmetry of the motion field. The similarity of both the peak accelerations and the waveforms at the three azimuths support a cylindrically symmetric source. This symmetry is retained in the vertical and radial components at increasing ranges. The symmetry pattern observed at 3 m in the non-linear regime has continued into the elastic region.

The motion field is not completely symmetric as shown by the existence of transverse accelerations (Figure 13). The occurrence of transverse motions from contained nuclear events has been noted previously (McLaughlin et al, 1983). For nuclear explosions, transverse near source motions have been observed to be as large as the radial and vertical components. Unlike the nuclear data, the CHEAT transverse motions are between 3 and 35 percent of the radial amplitudes (Figure 13). A coherent radiation pattern for the transverse motions was not found. As evident in Figure 13, there is wide variability in the transverse waveforms.

The development of the waveform over the 50-150 m range is illustrated in Figure 14. The high frequency body waves are followed by the relatively longer period surface waves. This interpretation is supported by a change from rectilinear to retrograde elliptical particle motion with time. At the 50 m range the body waves dominate both the radial and vertical

velocities. Between 75 - 100 m the surface waves become the largest contributor to the observed motions.

A characteristic displacement spectrum of one radial acceleration record is given in Figure 15. The noise intersects the data between 1 and 2 Hz and above 60 Hz. The source study discussed in Paper II is therefore constrained to the 2 - 60 Hz band. The spectrum in Figure 15 is typical of other ranges and is characterized by a corner frequency near 20 Hz and a spectral peak near 5 Hz. These two frequencies are characteristic of the initial P pulse and spall time seen in the close-in data. This observation argues that characteristics of the data in the 992 - 2976 m/kt^{1/3} range are controlled by processes in the near-source region.

CONCLUSIONS

The CHEAT experiment has demonstrated the feasibility of performing small chemical explosions in situ to study aspects of source phenomenology. The design of this particular experiment was based on a desire to characterize the motion field in both the linear and non-linear regimes. At ranges smaller than $364 \text{ m/kt}^{1/3}$ a three dimensional accelerometer array quantified the initial P pulse followed by the repartitioning of energy by the free surface. Observed displacement rise times begin at 25 ms at a scaled range of $82 \text{ m/kt}^{1/3}$ and increase to 50 ms at $215 \text{ m/kt}^{1/3}$. The pulse width, which is controlled by spall phenomena, is approximately constant at 190 ms throughout the array.

The data in the linear region ($992\text{--}2976 \text{ m/kt}^{1/3}$) exhibit the temporal effects observed in the non-linear regime. A characteristic spectrum has a corner near 20 Hz with a spectral peak at 5 Hz. The similarity of the radial and vertical waveforms from azimuth to azimuth at the $992 \text{ m/kt}^{1/3}$ range shows that the source is cylindrically symmetric. Transverse motions on the order of 3-35 percent of the radial and vertical accelerations suggest a small deviatoric source contribution. In contrast, near source transverse accelerations from full scale nuclear events are often equal to the radial and vertical components.

The detonation time of the explosion was shown to be small (μs) compared to the equivalent elastic source rise time (ms).

Available experimental evidence shows that the explosive detonates in a symmetrical manner.

The quantification of the relative contributions of the various effects to the equivalent elastic source function is described in Paper II. This requires forward and inverse modelling of the linear data set. The physical interpretations associated with these equivalent elastic source functions are constrained by the experimental data discussed in this paper.

Various aspects of the explosive source function can be constrained with an experiment similar to the CHEAT test described in this paper. The primary advantage of this procedure over other types of studies is that a single physical process can be isolated and resolved with a properly designed experiment. A significant advantage of small chemical explosions performed in the field over laboratory experiments is that geologic materials of interest are exercised in situ.

REFERENCES

- Ake, J. P. (1980). Letter Report and Preliminary Data Analysis, "Ground Motion in a Non-Airblast Environment." Engineering Research Institute, University of New Mexico, Albuquerque, New Mexico 87131.
- Crawford, R. E., C. J. Higgins and E. H. Bultman (1986). "The Air Force Manual for Design and Analysis of Hardened Structures," AFWL-TR-74-102, Air Force Weapons Laboratory, Kirtland AFB, New Mexico 87117-6008.
- Flynn, E. (1986). Effects of Source Depth on Near Source Seismograms, M. S. Thesis, Southern Methodist University, Dallas , Texas 75275.
- Greenhalgh, S. A. (1980). Effect of delay shooting on the nature of P-wave seismograms, Bull. Seis. Soc. Am. 70, 2037-2050.
- Higgins, C. J., R. L. Johnson, G. E. Triandafilidis (1978). "The Simulation of Earthquake-like Ground Motions with High Explosives", Report CE-45 (78) NSF-507-1, Department of Civil Engineering, University of New Mexico, Albuquerque, New Mexico 87131.
- Larson, D. B. (1982). Inelastic wave propagation in sodium chloride, Bull. Seis. Soc. Am. 72, 2107-2130.

Masse, R. P. (1981). Review of seismic source models for underground nuclear explosions, *Bull. Seis Soc. Am.* 71, 1249-1268.

Mueller, R. A. and J. R. Murphy (1971). Seismic characteristics of underground nuclear detonations, Part I. Seismic spectrum scaling, *Bull. Seis. Soc. Am.* 61, 1675-1692.

Murphy, J. R. (1977). Seismic source functions and magnitude determinations for underground nuclear detonations, *Bull. Seis. Soc. Am.* 67, 135-158.

McLaughlin, K. L. (1982). Spatial Coherency of Seismic Waveforms, Ph. D. Thesis, University of California, Berkely, 275p.

McLaughlin, K. L., L. R. Johnson, T. V. McEvilly (1983). Two-dimensional array measurements of near-source ground accelerations, *Bull. Seis. Soc. Am.* 67, 349-375.

McLaughlin, K. L., I. N. Gupta and R. Wagner (1985). "Finite Difference Cratering Support: Magnitude Determination of Cratering and Non-Cratering Nuclear Explosions," TGAL-85-3, Teledyne Geotech, Alexandria, Virginia.

Perret, W. R. and R. C. Bass (1975). "Free-Field Ground Motion Induced by Underground Explosions," SAND74-0252, Sandia Laboratories, Albuquerque, New Mexico.

Reinke, R. E. and B. W. Stump (1987). Stochastic geologic influences on near-field ground motions in alluvium, submitted *Bull. Seis. Soc. Am.*

Rinehart, J. S. (1959). "Spalling and Large Blasts, Proceedings of the 2nd Plow Share Symposium, San Francisco, May 13-15, 1959, part I, Rep UCRL-5675, pp 135-155, Lawrence Livermore Lab., Livermore, California.

Rinehart, E. and G. Veyera (1985). "MP-2 Review and Final Data Analysis," CRTA-TR-3751-1, California Research and Technology, Chatsworth, California.

Rodean, H. C. (1981). Inelastic Processes in Seismic Wave Generation by Underground Explosions, p97-190. Identification of Seismic Sources - Earthquake or Underground Explosion, Ed. by E. Husebye and S. Mykkeltveit, D. Reidel, Holland.

Sobel, P. A. (1978). "The Effect of Spall on m_b and M_s ," Teledyne Geotech Report SDAC-TR-77-12, Dallas, Texas.

Stump, B. W. and R. E. Reinke (1984). Spall observations and mechanisms in alluvium, J. Geophys. Res. 89, 11495-11506.

Stump, B. W. and L. R. Johnson (1984). Near-field source characterization of contained nuclear explosions in tuff, Bull. Seis. Soc. Am 74, 1-26.

Stump, B. W. (1985). Constraints on explosive sources with spall from near-source waveforms, Bull. Seis. Soc. Am. 75, 361-377.

Stump, B. W. (1987). Mathematical representation and physical interpretation of a contained chemical explosion in alluvium, Bull. Seis. Soc. Am. , accepted for publication.

Stump, B. W. (1986). Resolution of complex explosive source functions in the frequency domain, submitted *Geophys. J. Roy. astr. Soc.*

Stump, B. W. and R. E. Reinke (1987). Experimental confirmation of superposition from small scale explosions, submitted *Bull. Seis. Soc. Am.*

Trulio, J. G. (1978). "Simple Scaling and Nuclear Monitoring, " Applied Theory, Inc. Report ATR-77-45-2, Los Angeles, California.

Viecelli, J. A. (1973). Spallation and the generation of surface waves by an underground explosion, *J. Geophys. Res.* 78, 2475-2487.

Werth, G. C. and R. F. Herbst (1963). Comparison of amplitudes of seismic waves from nuclear explosions in four mediums, *J. Geophys. Res.* 68, 1463-1474.

Workman, J. W. , J. G. Trulio, E. S. Stokes (1981). "Trajectory Analysis, an Aid in Defining the MX System Ground Motion, Vol. 1: Methods of Determining Strain Paths in Axisymmetric Fields of Motion, Vol 2: Plan for a Key Proof Test: 10t HE Event, AFWL-TR-80-56, Air Force Weapons Laboratory, Kirtland AFB, New Mexico 87117-6008.

Figure Captions

Figure 1: Side view of the gages at scaled ranges of $364 \text{ m/kt}^{1/3}$ (18.35 m) and less.

Figure 2: Surface view of the gages at scaled ranges of $364 \text{ m/kt}^{1/3}$ (18.35 m) and less.

Figure 3: The gage array in the $992 \text{ m/kt}^{1/3}$ (50 m) to $2976 \text{ m/kt}^{1/3}$ (150 m) range.

Figure 4: Observed arrival times of the explosive front in a 1000 lbs TNT sphere.

Figure 5: Observed acceleration, velocity and displacement at the gage nearest to the source (scaled range of $82 \text{ m/kt}^{1/3}$).

Figure 6: The vertical propagation of the initial P pulse, its free surface reflection, and spall of near surface layers as observed on vertical accelerometers directly above the explosion.

Figure 7: The vertical acceleration at the free surface directly above the explosion. The initial P pulse, spall (-1g dwell), and spall rejoin can be observed.

Figure 8: The depth and range of spall in one two-dimensional plane. The first number next to each gage is the spall dwell time in ms and the number in parenthesis is the velocity at spallation in cm/s.

Figure 9: The three vertical accelerations from the 3 m range at azimuths of 0°, 120° and 240°.

Figure 10: The radial (R) and vertical (Z) velocity (light line) and displacement (heavy line) at the 1 m, 3 m, 6.5 m, 10.85 m and 18.35 m ranges and all observed depths. The dotted lines next to the vertical velocity records are representative of minus one g dwell.

Figure 11: The model representative of the source pulse growth in the non-linear region. The dotted lines represent spall dwell times at each range.

Figure 12: The azimuthal symmetry of the vertical and radial accelerations observed at the $992 \text{ m/kt}^{1/2}$ (50 m) range.

Figure 13: The observed transverse accelerations in the $992 \text{ m/kt}^{1/2}$ to $2976 \text{ m/kt}^{1/2}$ (50-150 m) range. 1s of data is displayed.

Figure 14: The radial and vertical velocity records from the $992 \text{ m/kt}^{1/2}$ to $2976 \text{ m/kt}^{1/2}$ (50-150 m) range.

Figure 15: The radial acceleration waveform and the displacement spectrum from the 50 m range. Noise dominates the spectrum below 1 Hz. and above 60 Hz.

Acknowledgements

The experimental program involved the following people: Paul Minto, Al Leverette, Joe Repichowski and Tony Tagliaferro. Lane Johnson and Tom McEvilly are due special thanks for support in fielding the far-field array. The review of Roy Berger added greatly to the paper. This work was supported under Grant AFOSR-84-0016 to Southern Methodist University.

AFWL CLOSE-IN STATIONS CHEAT

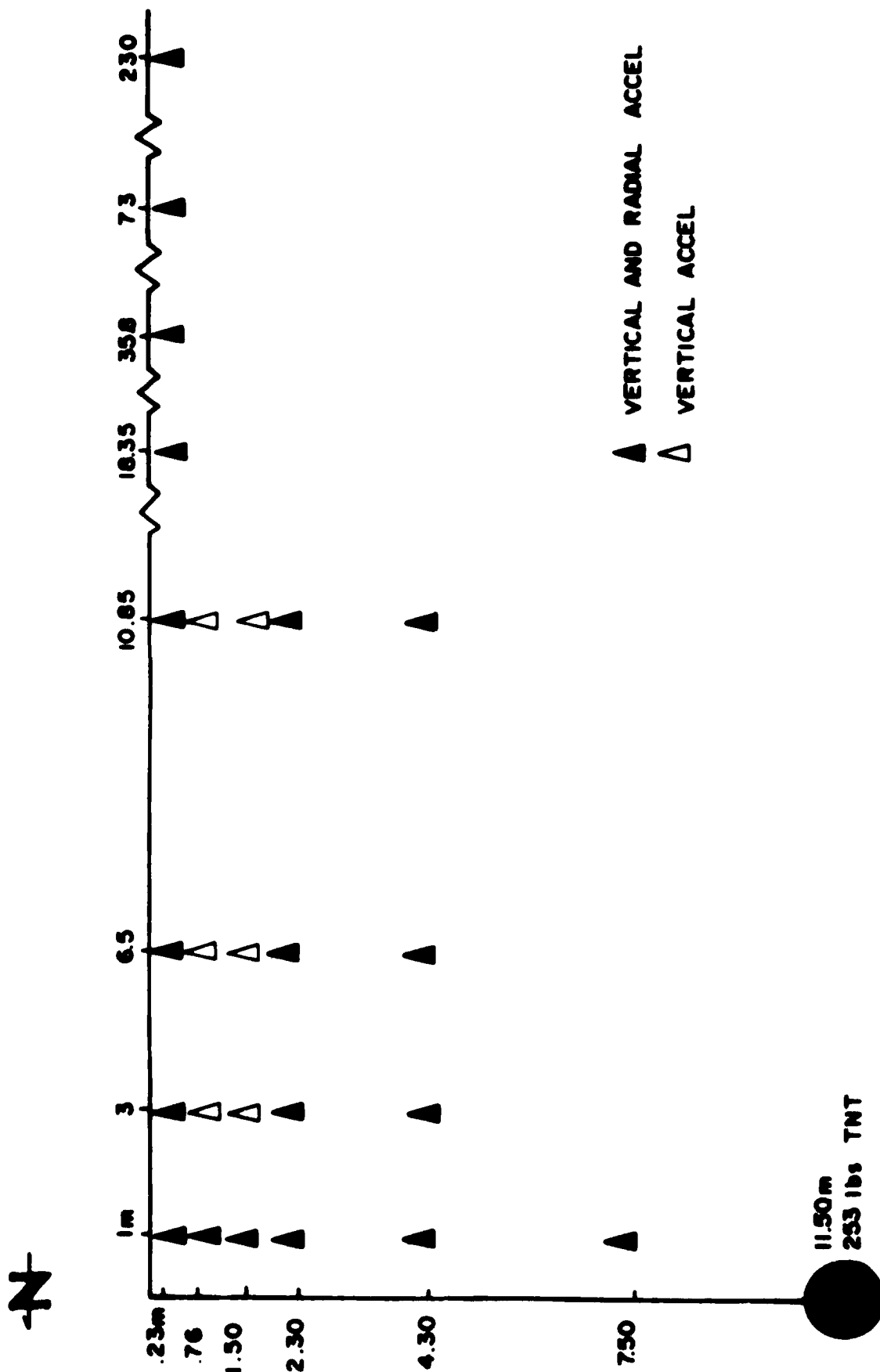


Figure 1
17

AFWL CLOSE-IN STATION PLANS CHEAT

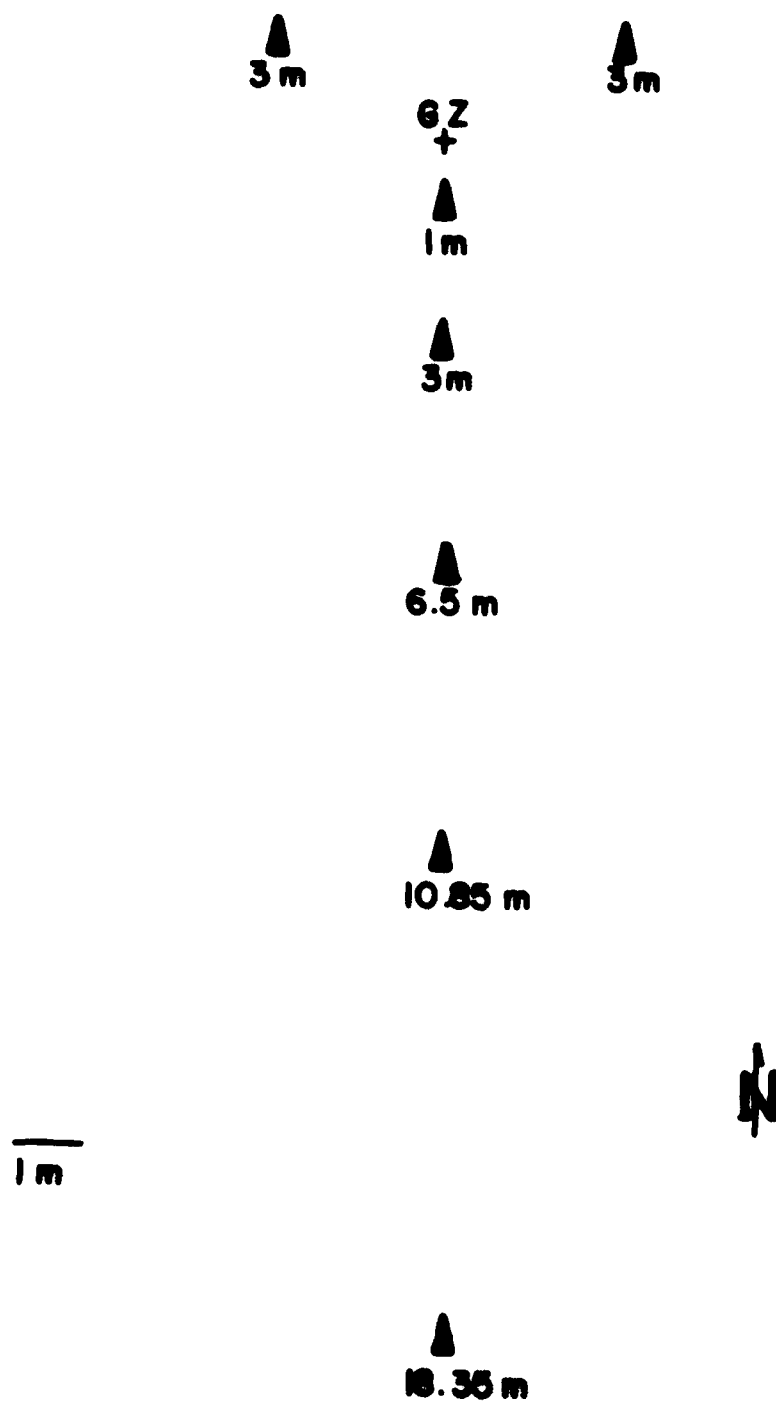


Figure 2
18

CHEAT DISTANT STATIONS

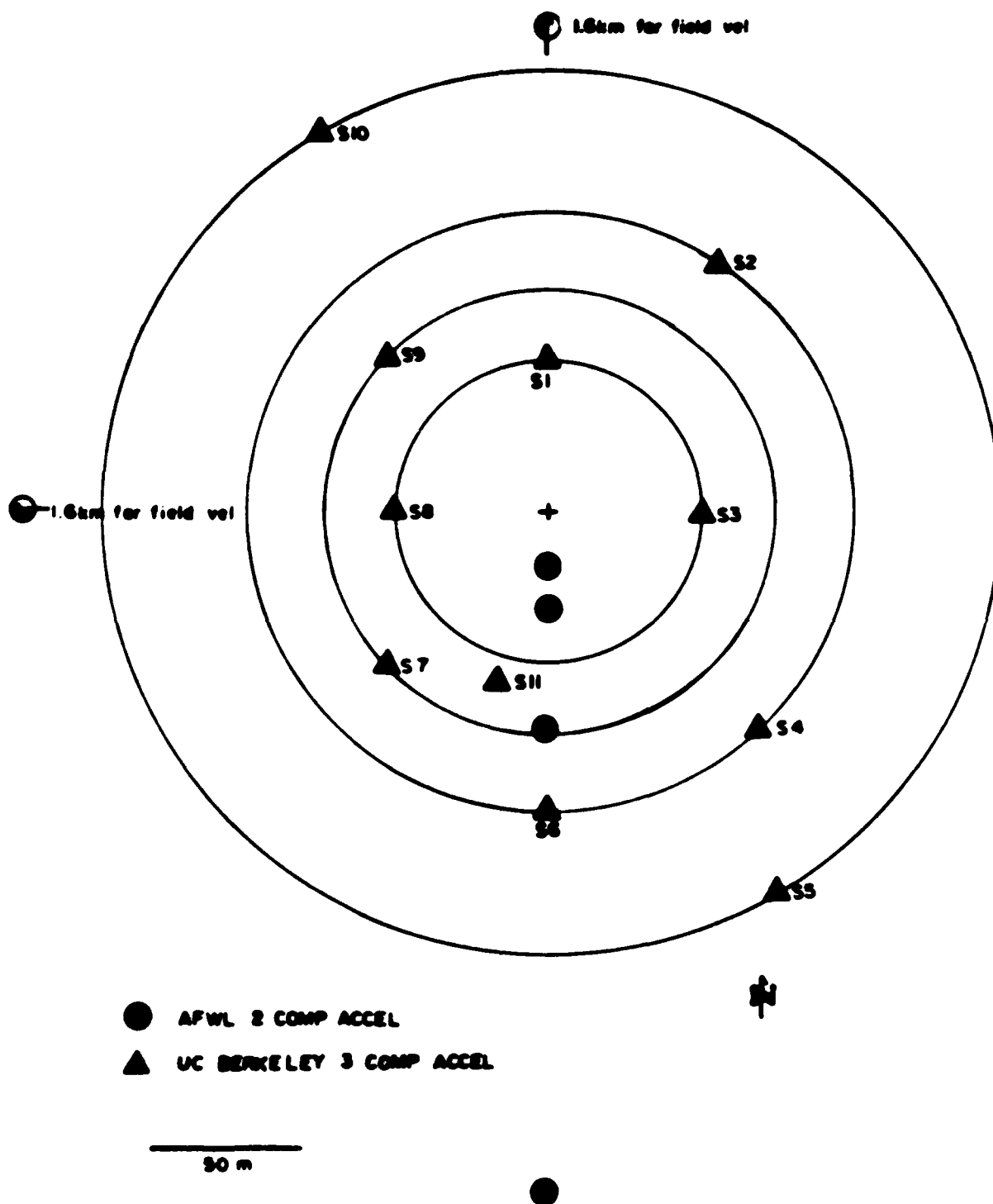


Figure 3
19

DETONATION TIMES of TNT SPHERE

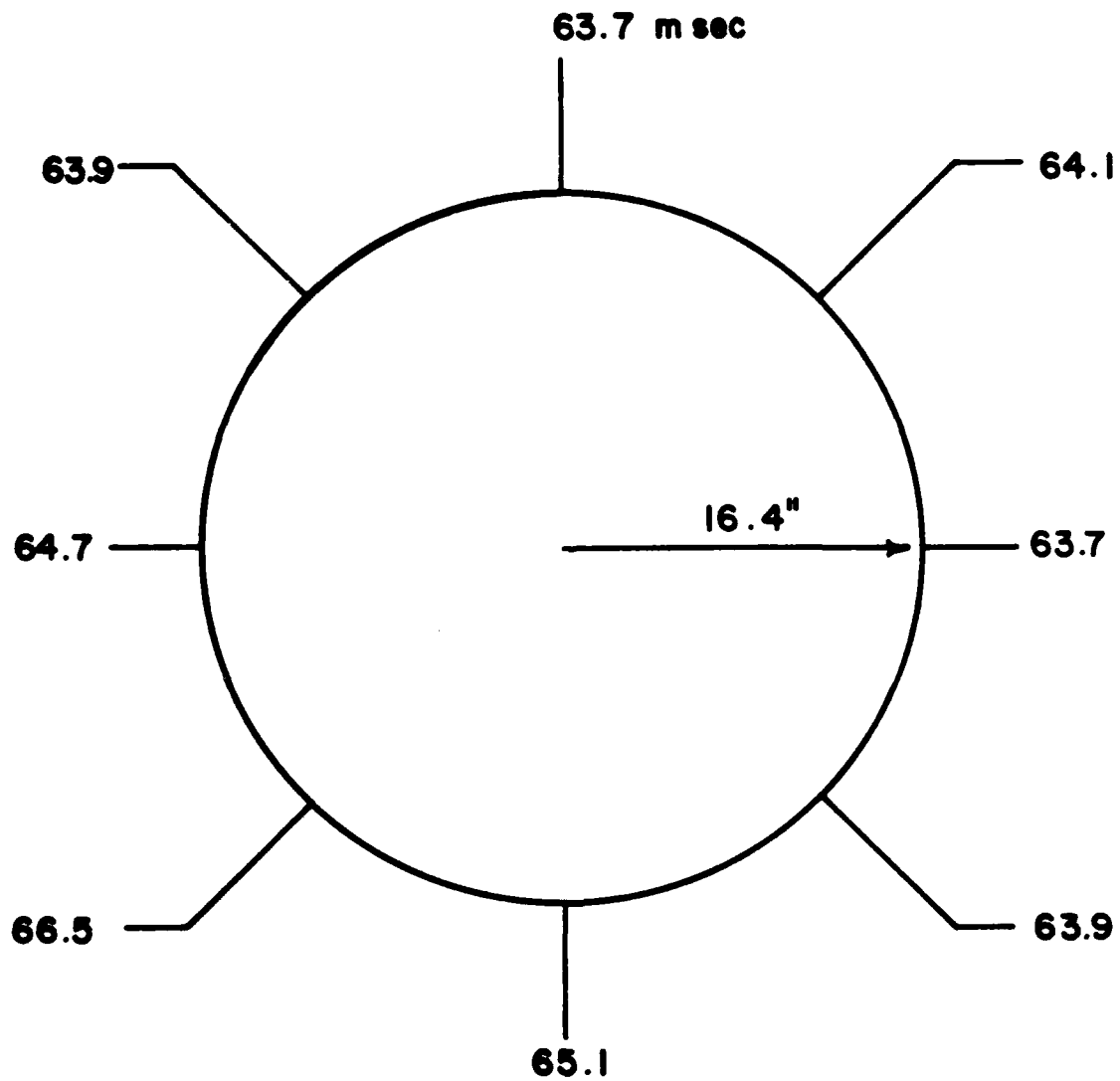


Figure 4

CHEAT CLOSE - IN OBSERVATIONS

R = 1.0m DEPTH = 7.5m RADIAL

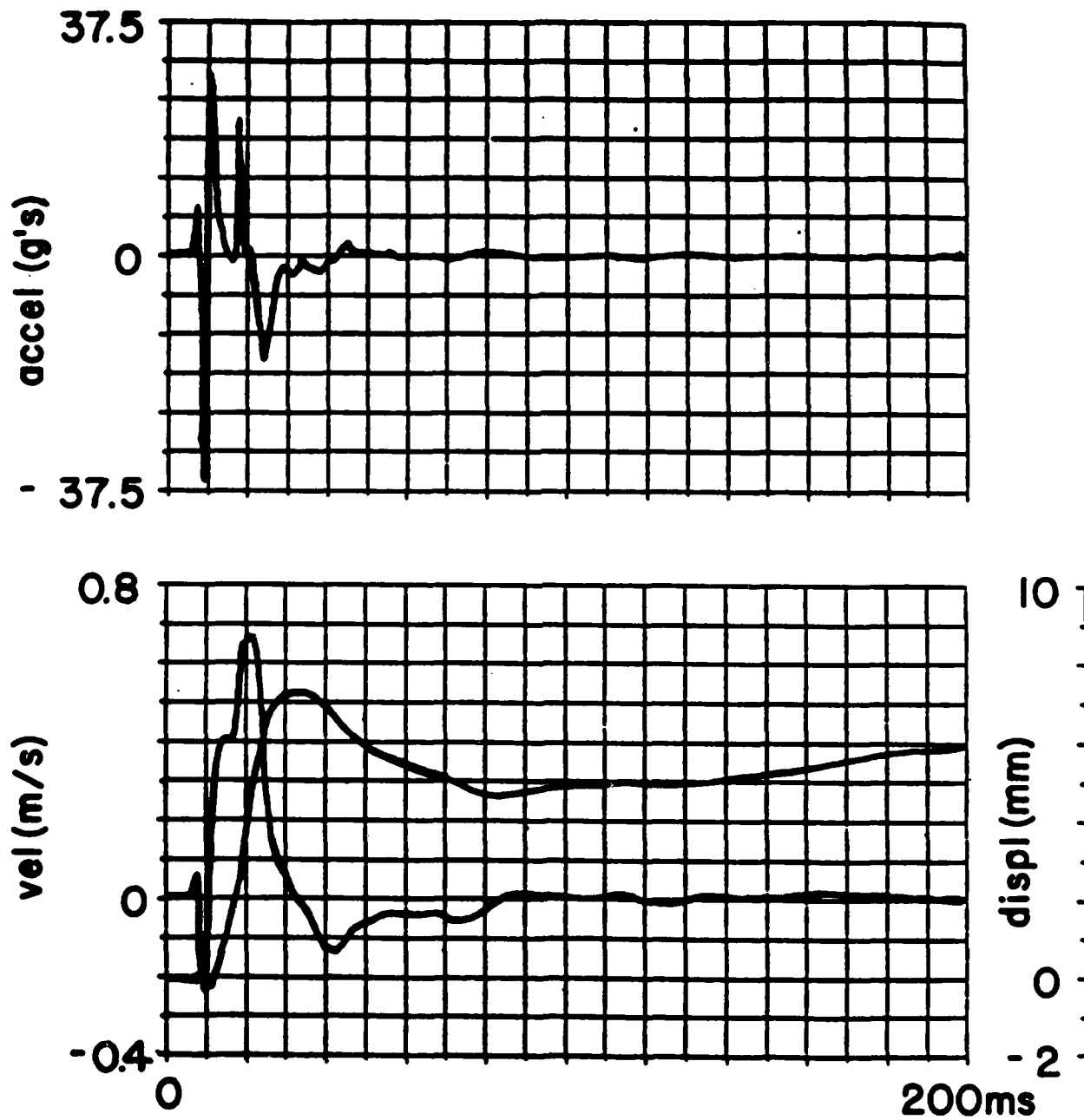


Figure 5

CHEAT SPALL RECORDS $r=1m$

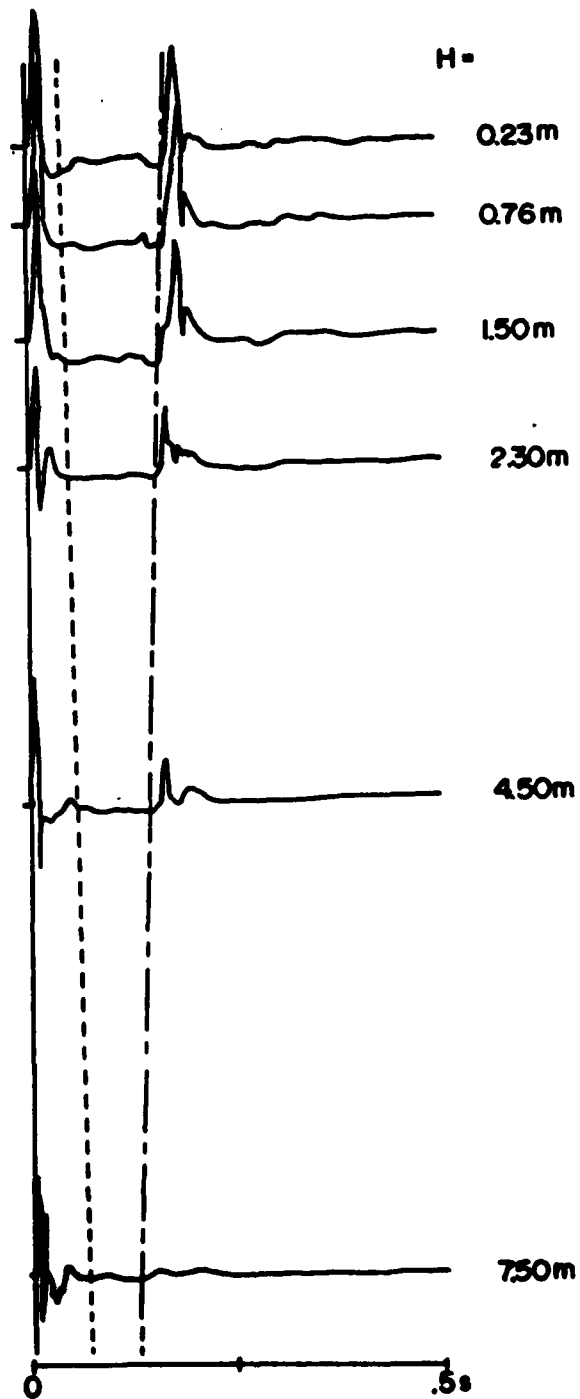


Figure 6

CHEAT CLOSE IN
1m radius, .23m depth

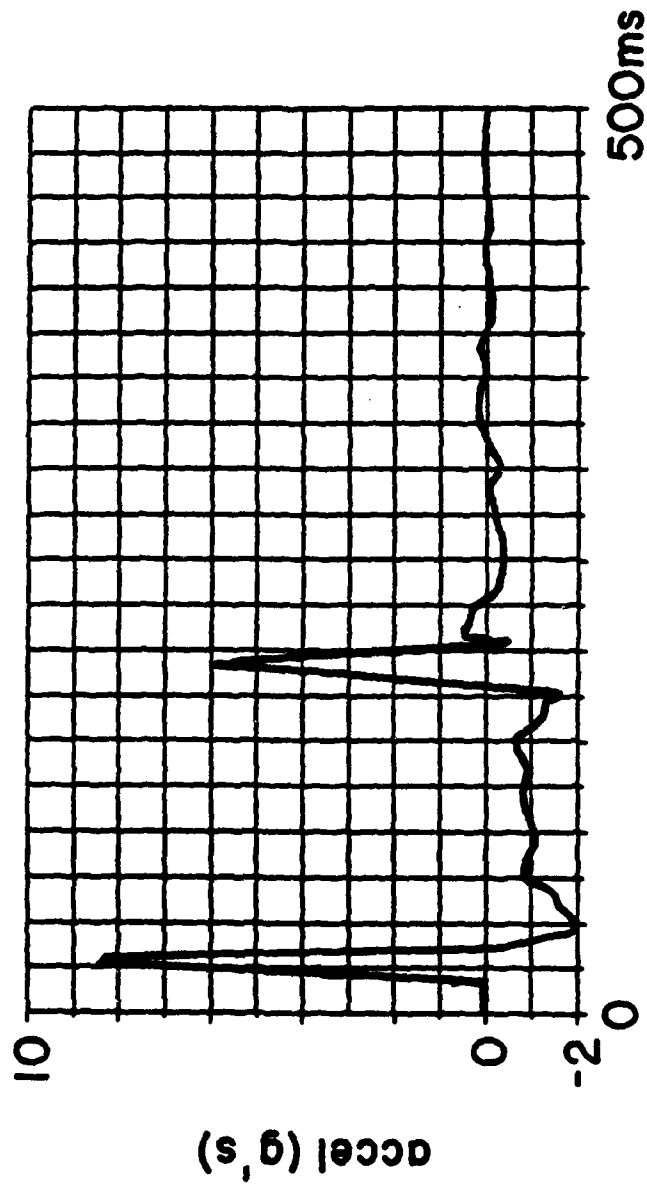


Figure 7
23

CHE, i SPALL RANGE, TIME, and ESCAPE VELOCITY

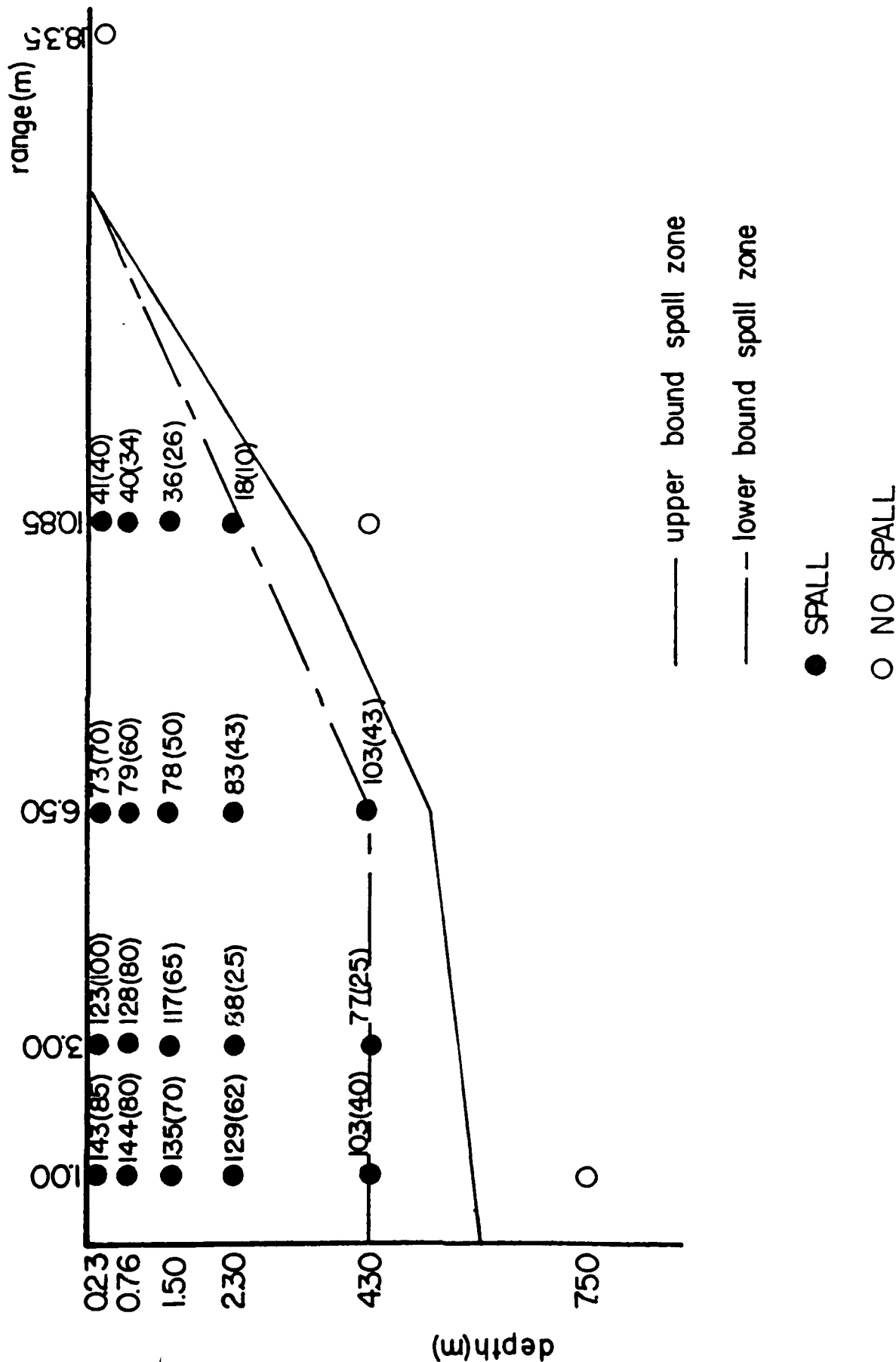


Figure 8
24

SPALL SYMMETRY

$r=3.0\text{m}$ $h=0.23\text{m}$

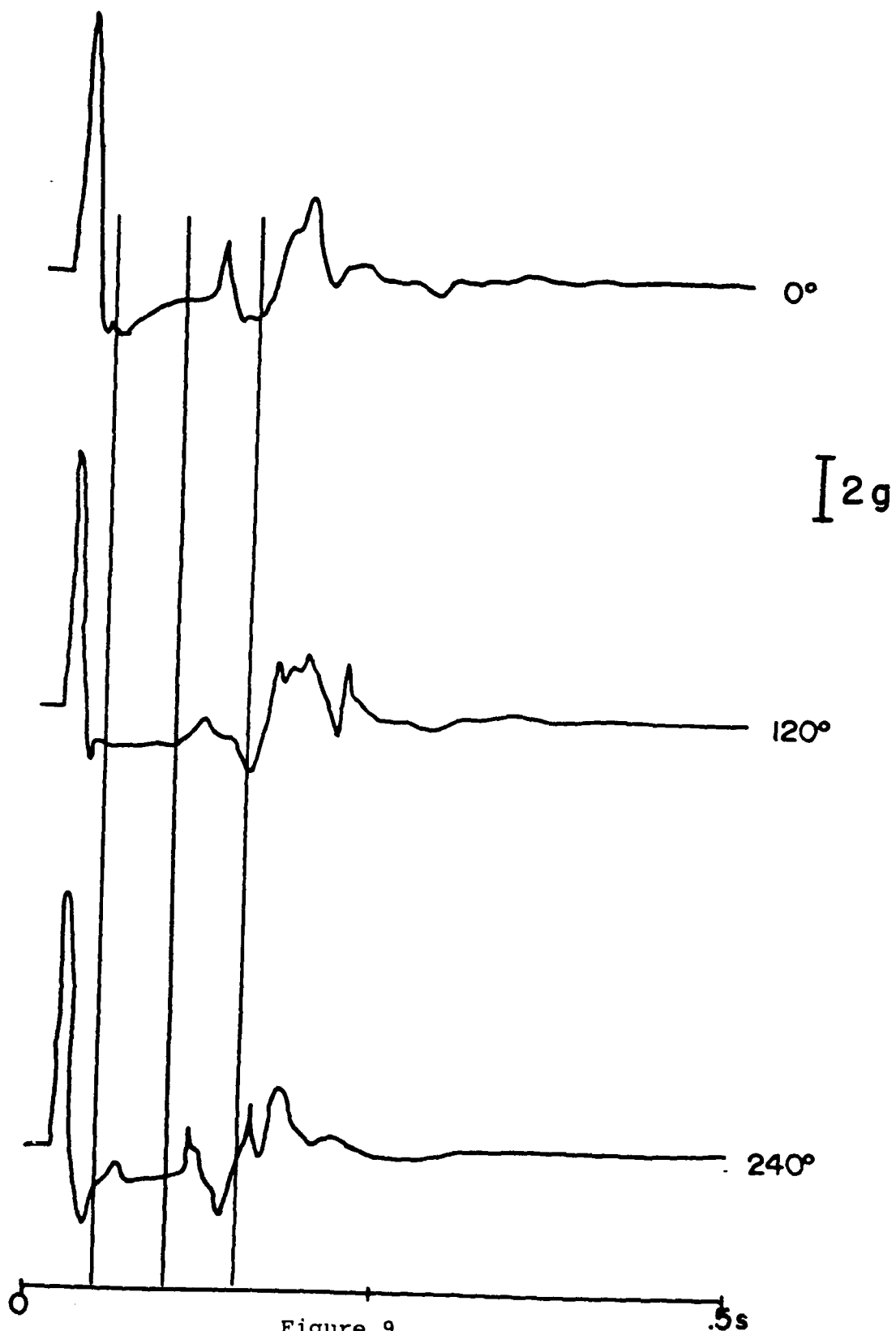


Figure 9
25

CHEAT 1m range

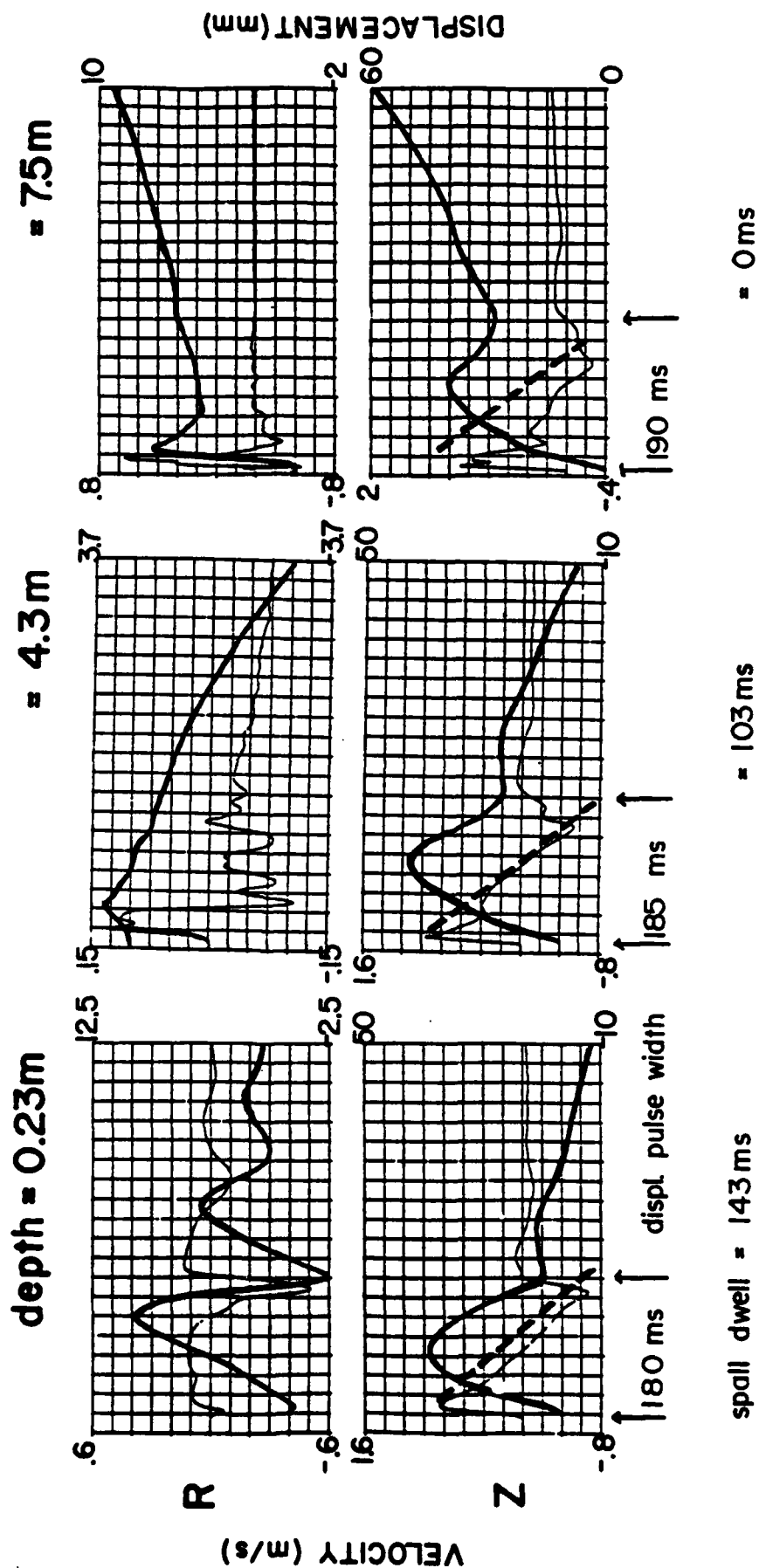


Figure 10
26

CHEAT 3m range

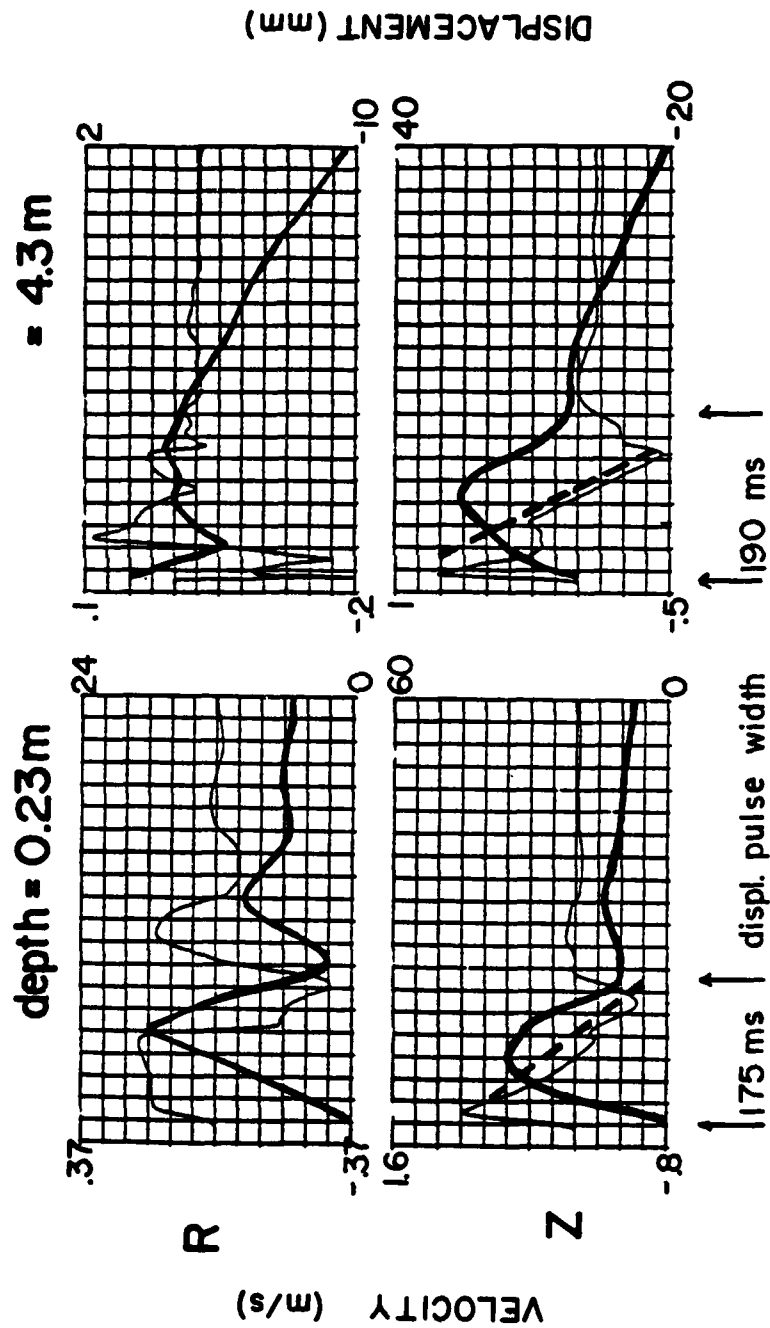


Figure 10b
27

CHEAT 6.5m range

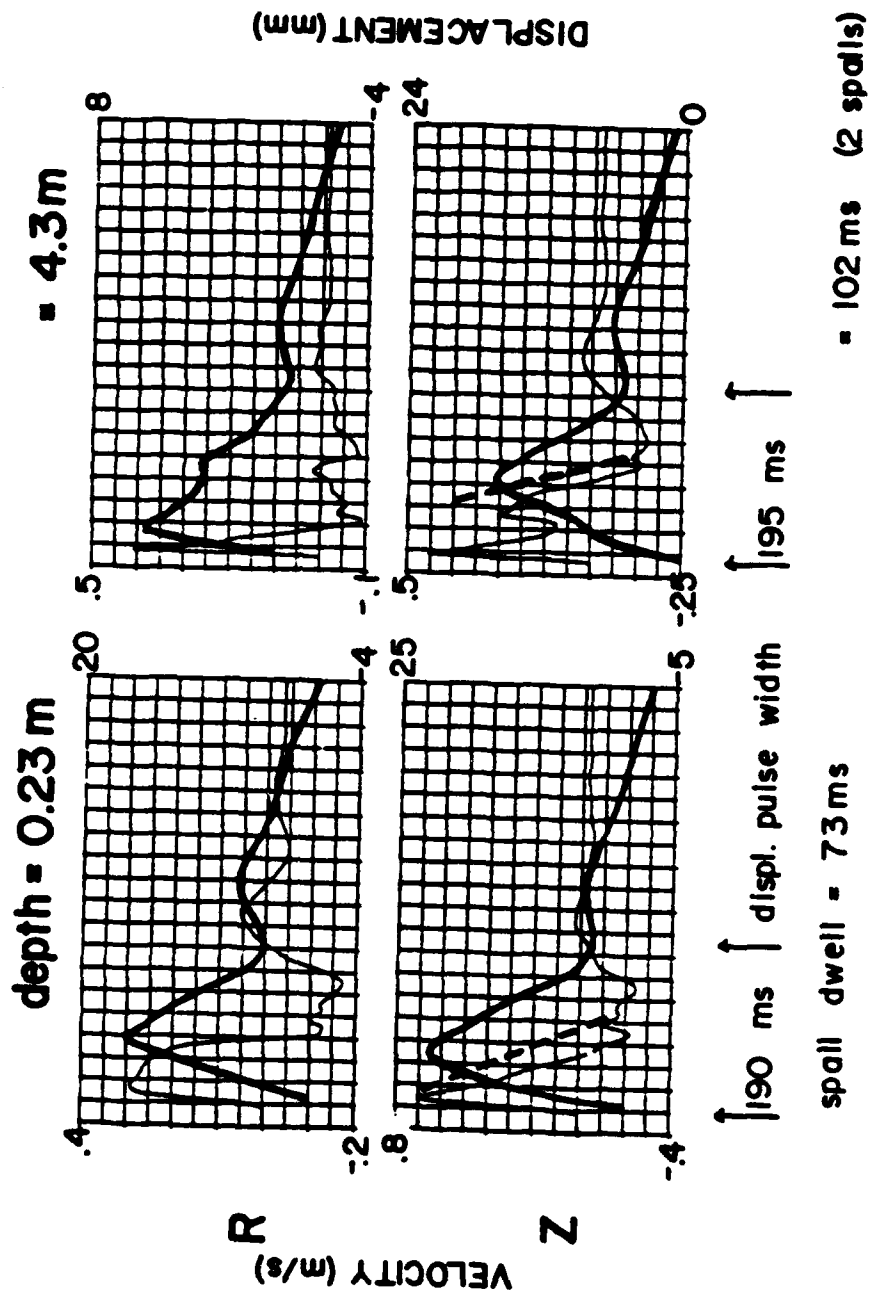
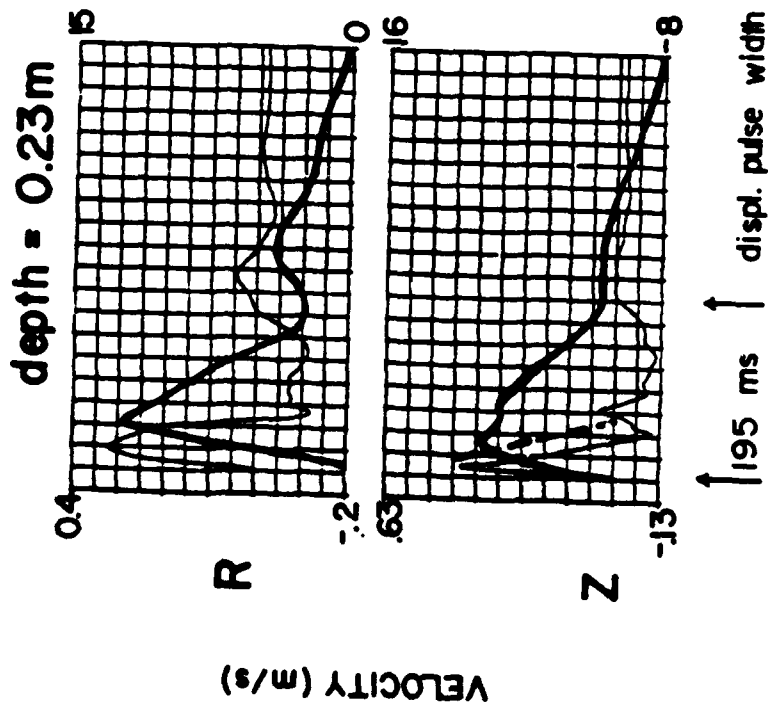
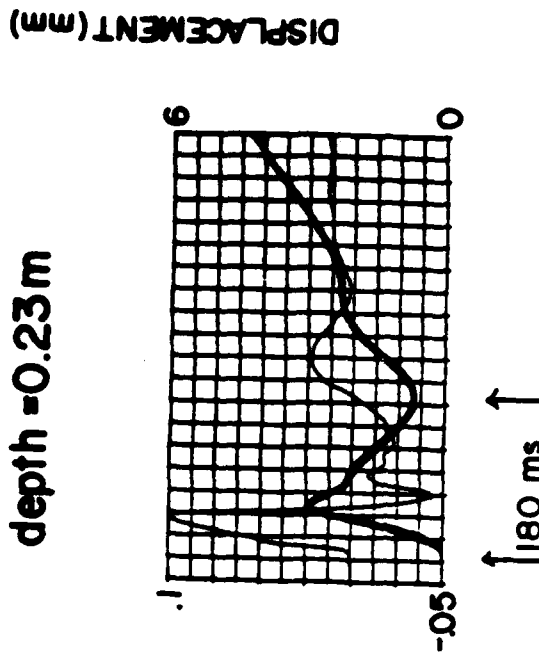


Figure 10c

CHEAT 10.85 m range



18.35m range
depth = 0.23m



spall dwell = 41ms

= 0 ms



Figure 10d
29

PULSE GROWTH IN THE NONLINEAR REGIME (VELOCITY)

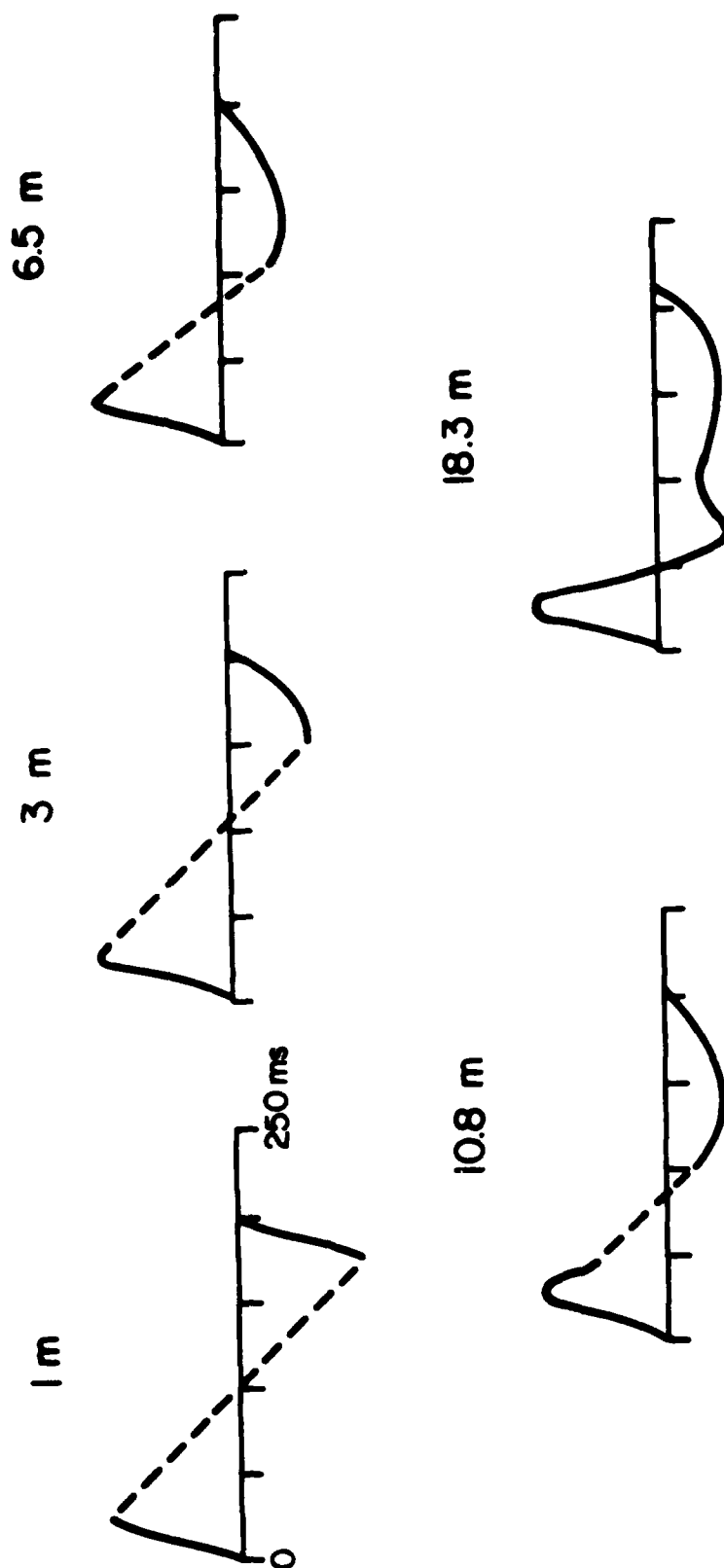
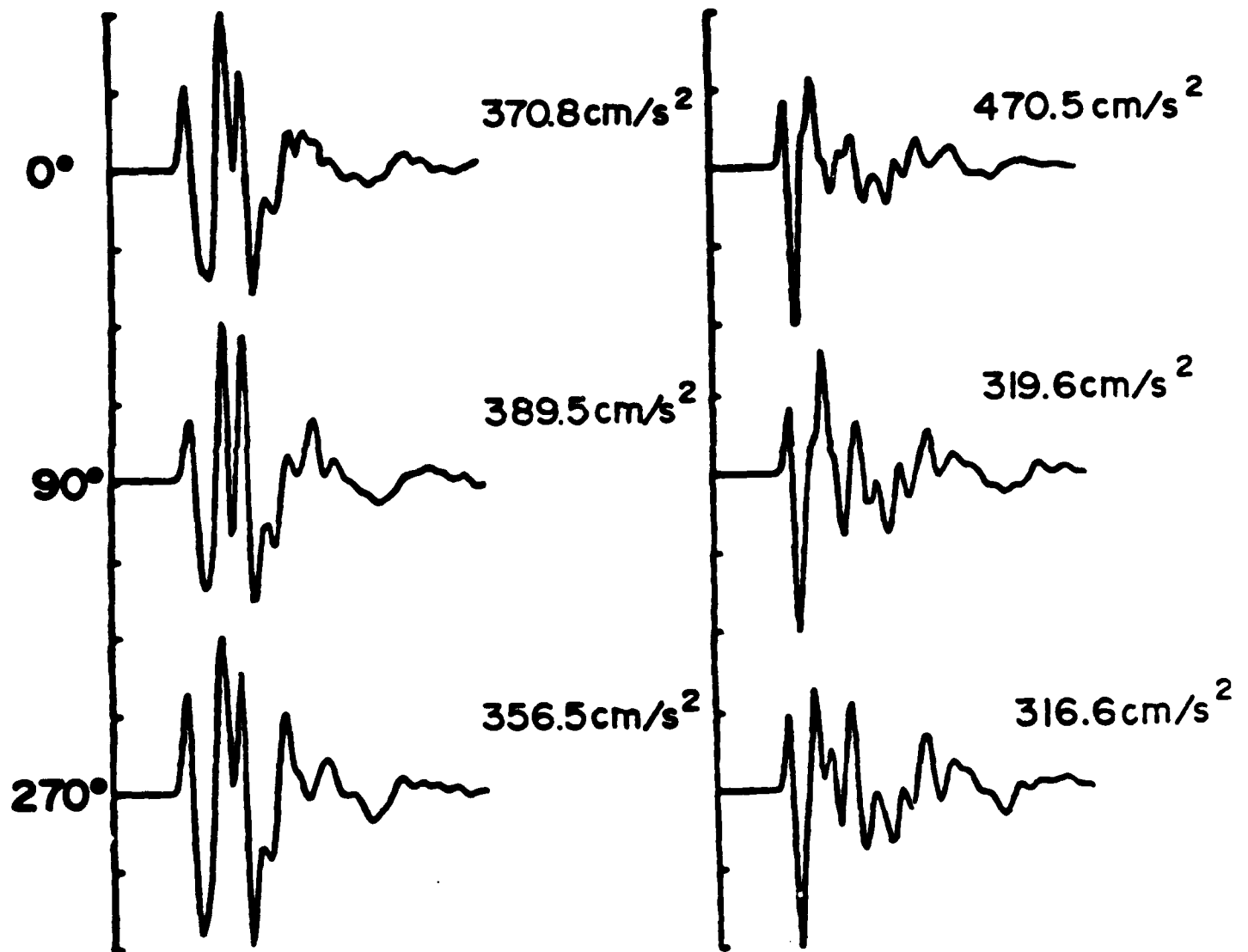


Figure 11
30

CHEAT 50m ACCELERATION

RADIAL

VERTICAL



0 20 40 60ms

Figure 12
31

CHEAT TRANSVERSE

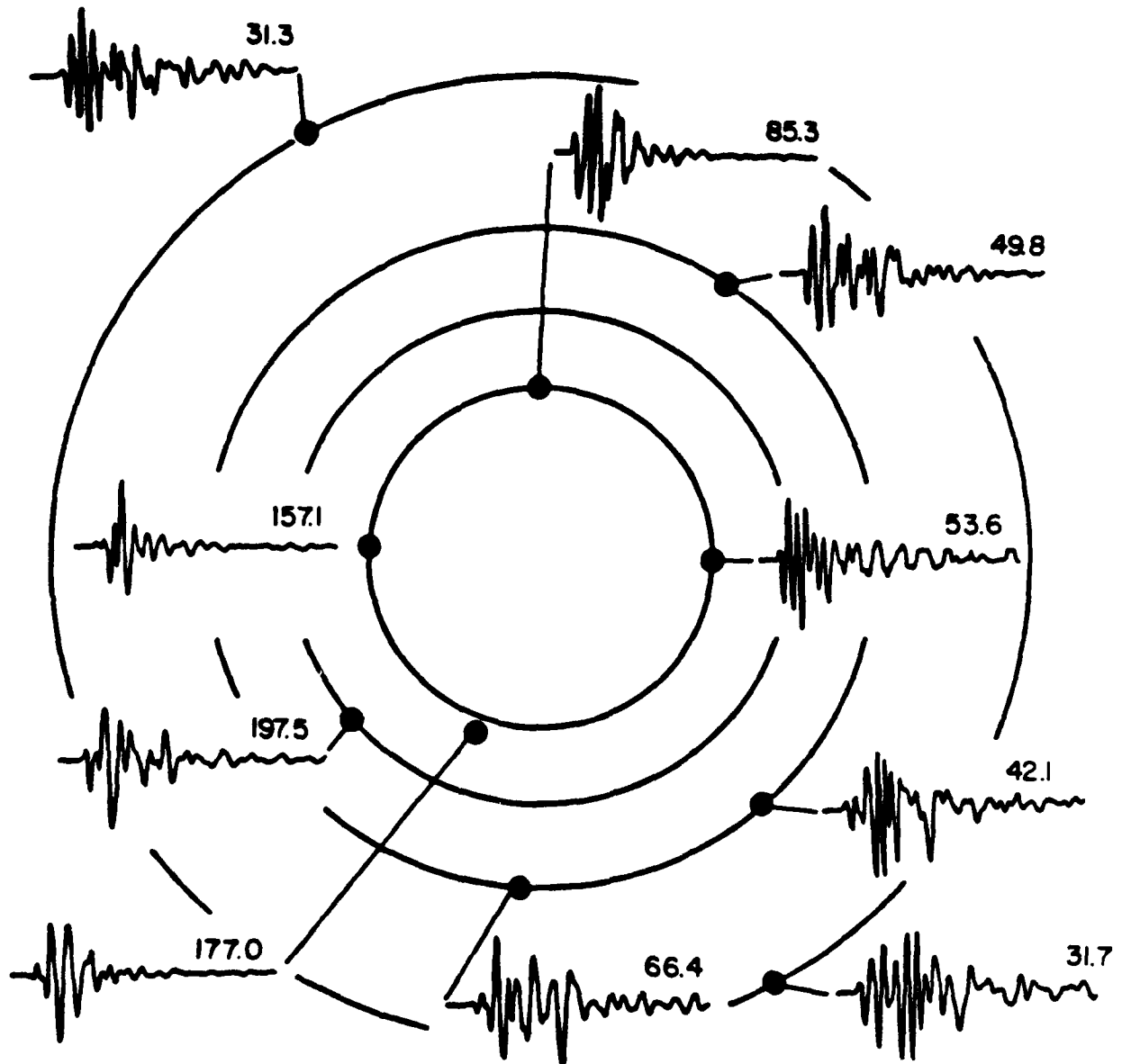


Figure 13
32

CHEAT RECORDS

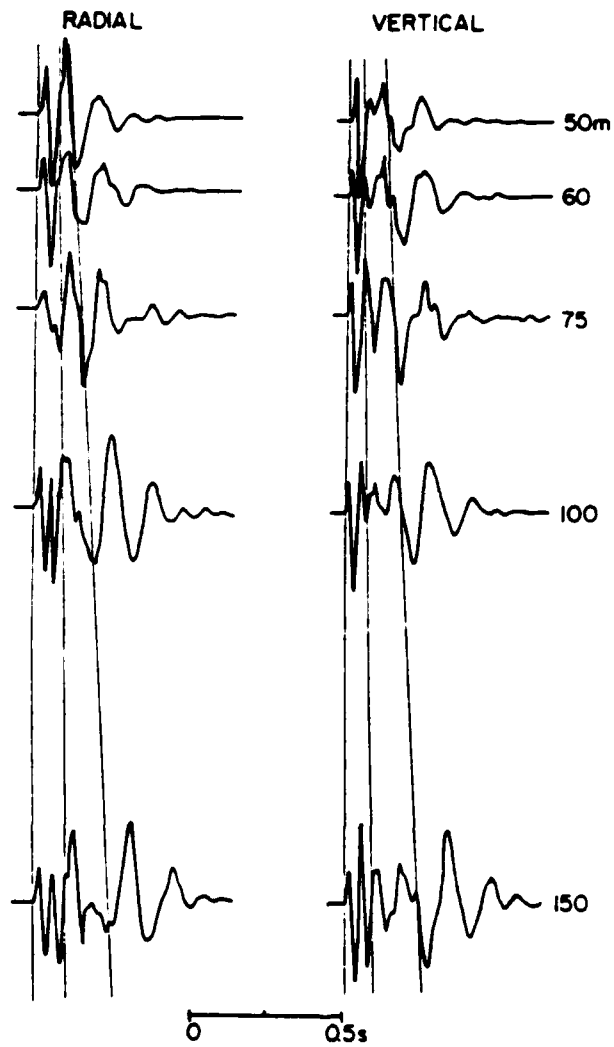


Figure 14
33

CHEAT R8 SPECTRUM

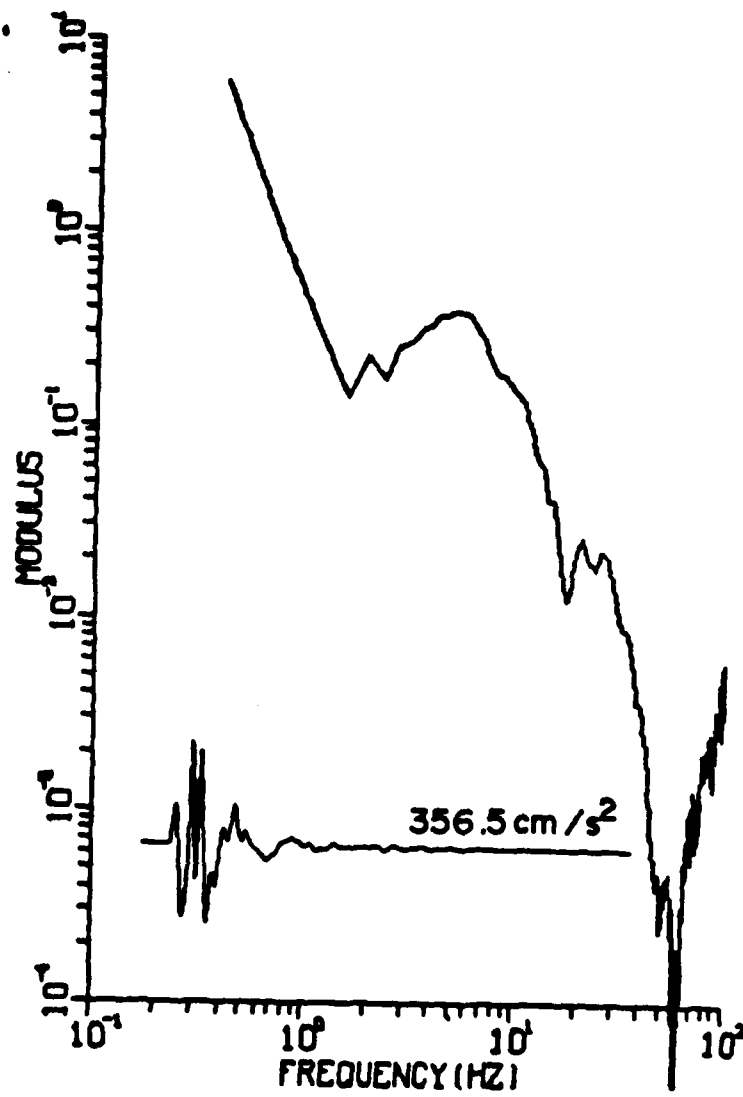


Figure 15
34

**MATHEMATICAL REPRESENTATION AND
PHYSICAL INTERPRETATION OF A CONTAINED
CHEMICAL EXPLOSION IN ALLUVIUM**

**Brian W Stump
Department of Geological Sciences
Southern Methodist University
Dallas, Texas 75275**

ABSTRACT

The characterization of the equivalent elastic source for a small (253 lb TNT) chemical explosion detonated in alluvium is given. The representation is constrained by a well known propagation path. Data from the nonlinear region ($<215 \text{ m/kt}^{1/3}$) are used in interpreting the moment tensor representation. The results of this study are: (1) The applicability of frequency domain moment tensor representation is shown; (2) The source is composed of two parts - the initially spherical explosion followed by the cylindrically symmetric spall; and (3) The deviatoric source components are an order of magnitude smaller than the spherical explosion and cylindrical spall contributions. The spherical explosion is shorter in duration (50-80 ms) than the spall source (200 ms) which is delayed in time. The initial explosion can be modeled by the isotropic moment tensor while the spall source is represented as the moment tensor elements with the ratio: $M_{11} = 1$, $M_{22} = 1$, $M_{33} = 2$. Comparison of these results with those from nuclear explosions suggests that similar phenomena occur in these cases also.

INTRODUCTION

The determination of the explosion source function in geological materials has remained a problem that has not been completely quantified. Questions still remain concerning source overshoot (Burdick et al, 1984; Douglas and Hudson, 1983), corner frequency scaling (Mueller and Murphy, 1971), high frequency roll-off (Stump and Johnson, 1984; Peppin, 1977; Rodean, 1981; von Seggern and Blandford, 1972), quantification of nonlinear processes such as spall (Day et al, 1983; Stump, 1985; Viece111, 1973; Bakun and Johnson, 1973) and nonisotropic source processes (Lay et al, 1984; Aki and Tsai, 1972). The inability to resolve these aspects of the explosion source has resulted from observational data which is inadequate for source quantification. Explosion studies have primarily relied upon teleseismic and to a lesser degree near-source data from the explosion.

In no case has a complete experiment been designed and analyzed with the primary goal being the characterization and modeling of the three-dimensional motion field beginning in the nonlinear regime and extending to the near-source linear zone. This paper will illustrate the inverse modeling of a 253 lb TNT sphere detonated at a depth of 11.5 m in alluvium. The design of the experiment and a

discussion of the observational data is given in Stump and Reinke (1986) (referred to as Paper I). The test site was chosen to minimize trade-offs between propagation path and source. The design goals of the experiment were to constrain the following: (1) The importance of free surface interactions on the explosion source function; (2) The characterization of the chemical explosion; (3) The separation of isotropic and deviatoric source components in a media with well constrained propagation path effects; and (4) The utility of motion data from within the nonlinear and linear regime in interpreting the seismic source function.

The mathematical model of the source which results from this inverse modeling exercise will be physically interpreted with the aid of insights gained from the analysis of the nonlinear data. This data resolves some of the nonuniquenesses in such interpretations. The reader is referred to Paper I for details of station distribution, recording characteristics, and explosive characterization.

VELOCITY STRUCTURE AND SYNTHETICS

The alluvial test site was chosen because of intensive site characterization work that has been completed (Stump and Reinke, 1982). In addition, a number of depth of burial experiments were conducted near-by (Flynn, 1986). The alluvial test site in combination with the chemical explosive led to the test acronym, Contained High Explosive Alluvium Test (CHEAT).

The results of several refraction surveys in the test area are summarized in 1a. The near surface P wave velocities begin at 400 m/s and increase to nearly 900 m/s. The interpretation of this data led to the velocity model given in Figure 1b consisting of 3 layers over a half-space. The layer P velocities are 366, 671, 823 m/s with the half-space at 23m with a velocity of 1120 m/s. The only deeper structure in the test area is the water table at 75 to 80 m where a slight increase in P velocity is expected. Based upon the range of data to be modeled (50-150m) this structural complication was not included.

The first arrival data from the CHEAT experiment is in agreement with the refraction data. The P velocity structure for the test bed is well resolved. Unfortunately, like many geologic site characterization studies, the shear

velocity structure is less constrained. Cross hole shear surveys were conducted, but led to results with a good deal of scatter. The data indicate shear velocities beginning near 200 m/s at the free surface followed by a positive gradient with depth. The shear velocity may reach 400 m/s near the shot depth as supported by a shear refraction study.

The site characterization information is important for the computation of synthetic seismograms. This part of the study was approached in two ways. The first was to compute the simplest possible path effects for each distance range. In view of the simple observational seismograms (Figures 12 and 14, Paper I), the first set of models were for an elastic half-space. An average velocity model was chosen which led to the best fit to the slope of the refraction data and the Sv-P times on the CHEAT data at all ranges. This model was $V_p = 920$ m/s, $V_s = 350$ m/s, $\rho = 1.9$ gm/cc and is summarized in Table 1. The second iteration on this half-space model was to pick a P and Sv velocity at each range in order to better replicate the time of arrival data. In this case the P time of arrival data was from the depth corrected refraction data and the Sv-P times measured from the CHEAT data. The resulting models yielded a P velocity which began at 558 m/s (50m) and increased to 788 m/s (150m). Poissons ratio for the 50 m range was 0.325 and decreased to 0.255 at the 150 m range.

Greek
Rho - ρ

A modified reflectivity technique for synthetic computation was employed so that both body and surface wave contributions could be included in the response from a plane layer velocity model. A variety of iterations in modeling were attempted prior to the final structure in Figure 2. The primary variables in these trials were the shear velocities since it was the least resolved in the site exploration work. The use of a low shear velocity gradient was supported by a desire to reduce trapped energy in the model that led to long ringing seismograms quite unlike those observed in the test. The shallow shear refraction data also supported this conclusion.

These three sets of Green's functions(single half-space, range varying half-space, layered reflectivity) were developed for the study since they span the range of possible models for matching the observational data. Figure 3 illustrates the synthetics for the layered structure. The major differences between the layered and half-space models are the development of a complex P signature beyond 75 m in the reflectivity seismograms and the dispersion of the surface wave trains, in particular the Love waves.

FIRST DEGREE MOMENT TENSOR MODELING

The primary purpose of the CHEAT experiment was the determination of the equivalent elastic source function and the relation of this mathematical model to the physical source processes as constrained by the nonlinear data. The first step in achieving the equivalent elastic source function is a parameterization of the forward problem. Previous studies have utilized the first degree moment tensor representation (Stump and Johnson, 1984) for explosions:

$$U_{\alpha}(x,t) = G_{\alpha 1, j}(x,t; \Omega, 0) \otimes M_{1, j}(\Omega, t) \quad (1)$$

⊗
convolution
sign.

The isotropic part of the moment tensor is taken to be proportional to volume changes in the source region and thus the spherical explosion component of the source. The deviatoric part of the moment tensor is taken as the source component not accounted for by the spherical representation of the source.

The nonlinear motion data (Paper I) has illustrated the importance of spall. In an attempt to explicitly include this process in the source parameterization Day et al (1983) added a set of vertical point forces such that total momentum is conserved. Since spall is spatially separated

from the explosion its centroid is different. In order to include these effects equation (1) becomes:

$$U_k(X,t) = G_{k3}(X,t;X_3,0) \otimes f_3(X_3,t) + \\ G_{k1,3}(X,t;\Omega,0) \otimes M_{1,3}(\Omega,t) \quad (2)$$

Where x_3 indicates that the spall source is at a different depth than the explosion. Stump (1985) studied equation (2) in a forward calculational procedure and determined that the zeroth degree moment contribution could account for 50% of the observed near-source waveforms from explosions. The size of the contribution was dependent upon the spatial finiteness of the source which was modeled as a source rise time effect. The finite spatial effects yielded a reduction of the high frequency contribution of this secondary source. In light of these results, the CHEAT data set was designed to be used in an inversion procedure to determine the complete source. Equation (2) transformed into the frequency domain then yields the necessary set of linear equations:

Greek
Omega 'w'

$$U_k(X,w) = G_{k3}(X,w;X_3,0) f_3(X_3,w) + \\ G_{k1,3}(X,w;\Omega,0) M_{1,3}(\Omega,w) \quad (3)$$

$U_k(X,w)$ are the observed near source seismograms for CHEAT,
(G_{k3} and $G_{k1,3}$ are the material Green's functions discussed

and f_3 and M_{13} are the source characterization we wish to determine.

The application of the inverse procedure for the determination of f_3 and M_{13} are dependent upon the linear independence of the Green's functions associated with these two sources at different depths. Stump (1986) shows that in the near-source region these terms are not independent. The following proportionality is shown through a set of forward models and inversions of synthetic data:

Greek letter
alpha ' α '

$$G_{K3} \propto G_{K1,1} + G_{K2,2} + 2G_{K3,3} \quad (4)$$

This linear dependence leads to a condition in which both the zeroth and first degree moments cannot be uniquely recovered. Even though the forward modeling and nonlinear data indicate the spall process is important the linearity shown in equation (4) forces the inclusion of only the first degree moment tensor. Vertical asymmetries in the resulting first degree moment tensor can then be interpreted in terms of the spall contribution utilizing equation (4). After the isotropic source and the vertical asymmetry has been removed from the moment tensor that which remains will be interpreted as the deviatoric component.

The synthetic calculations of force and force couple sources indicate that to convert a point force model to a force couple one must integrate the point force source (to account

for spatial derivative difference in the Green's functions) and multiply the result by 4×10^5 to yield dyne-cm (Stump, 1983). The spall momentum estimates from CHEAT reported in Paper I when combined with an appropriate spall rise time to account for finite spatial effects yields a force couple strength of 2.0×10^{14} dyne-cm. This source strength will be checked against the results of the inversions.

SOURCE INVERSIONS

The three velocity models were each used in the inversions. Two inversions were completed for each velocity model. The first included all near-source data (992-2976 m/kt^{1/3}) totaling 28 seismograms. The second inversion was completed with the data from 50, 60, 75 m range excluding all the 100 and 150 m data (15 seismograms). These two sets were used to investigate the importance of station distribution in resolving the source function.

In all inversions, the data modeled were velocity records. The degree of fit for all radial and vertical components was good. In general, the transverse motions were not adequately modeled suggesting that they may result from waves scattered by geologic inhomogeneities. The observed and calculated seismograms from the range varying half-space Green's functions at station 3 are given in Figure 4. These observations and synthetics are for the 50m range and illustrate the good fits to the radial and vertical records and the poor fit to the transverse. The fit to the complete observational data set is summarized by the average correlation coefficients for the R, T, Z components in Table 2. As the Table illustrates, the layered velocity model led

to the best fits although the significance of the difference is small. The most marked change in the correlation coefficients occurs for the vertical seismograms when the data at the 100 and 150m ranges are deleted. One vertical record at 150 m range is very poorly modeled, with a correlation coefficient of .01, accounting for the majority of the discrepancy. This particular station may be strongly affected by local geologic conditions, improper installation, or instrumentation problems. The choice of one velocity model and resulting Green's functions is difficult based upon the data fits summarized in Table 2. The layered structure may be chosen in light of its small improvement in fits to the observational data.

The isotropic moment tensors (moment and moment rate) from the inversion utilizing all the data (50-150m) and the three sets of Green's functions are given in Figure 5. The comparison of the three time functions are remarkably similar in light of the differences in the Green's functions. In each inversion the source consists of an initial pulse of duration 50-80 ms followed by a second pulse with duration near 200 ms.

The spectral characterization of the isotropic source function is given in Figure 6. The spectrum of the source shows a corner frequency near 20 hz followed by a high frequency roll-off with a slope of 3. The high frequency

(roll-off is comparable to that observed in the data. A second peak in the spectrum near 5 hz is indicative of the second pulse seen in the source function. The increase in spectral level beyond 60 hz indicates the frequency at which the variances in the moment tensor begin to be as large as the estimate itself.

PHYSICAL SOURCE INTERPRETATION

The interpretation of the isotropic component of the CHEAT explosive source is that the initial part of the explosion consists of a pulse with a duration of 50-80 ms, followed by a secondary source with a duration of 200ms. This representation follows directly from the analysis of the data within the nonlinear regime ($215 \text{ m/kt}^{1/3}$) reported in Paper I and validates the fact that these aspects of the moment tensor representation are actual manifestations of physical processes occurring in the source region. The first pulse results from the spherically symmetric explosion followed by a second longer period pulse representing the cylindrically symmetric spall contribution.

Further support for this interpretation comes from the comparison of the source from the moment tensor inversion with the velocity record at 18.35m ($364 \text{ m/kt}^{1/3}$). A general representation equation for seismic sources includes terms representing initial conditions, boundary conditions, or body forces (Aki and Richards, 1980). The moment rate tensor, \dot{M}_{ij} , utilizes the body force representation and should be comparable to very near-source velocity records. In Figure 7, a comparison of wave shapes between the moment rate tensor as determined from observational data at the 50-150m ranges to the near-source velocity record at 18.35m is

given. The comparison is excellent including the initial pulse from the spherical explosion followed by the longer period spall contribution.

The peak values for the moment and moment rate tensors for the six inversions completed in this study are given in Table 3. Since both the P and S velocities vary between the three models, there is an order of magnitude variation in peak moment. The best velocity models (range varying half-space and layered) yield a factor of 2-3 variation in absolute moment. It is this absolute variation which is representative of the scatter in source size estimates. The primary reason for this variation is the unresolved shear structure and the fact that the layered structure can return down going energy back to the free surface while the half-space model cannot.

In all inversions summarized in Table 3, the M_{33} component is larger than the nearly equal M_{11} , M_{22} . This fact is shown in the time series given in Figure 8b. The initial pulse is symmetric on the M_{11} , M_{22} , M_{33} components while the secondary source attributed to spall introduces the vertical asymmetry. The frequency shift between the two sources yields a moment rate tensor (Figure 8a) with peak values which are nearly symmetric while the moment tensor (Figure 8b) has a M_{33} component as much as two times larger

than M_{11} and M_{22} . Such a long-period asymmetry matches the spall model.

That part of the moment tensor which is left after accounting for the spherical explosion and cylindrical spall is quite small as illustrated in Figures 8a and 8b. The off-diagonal elements of the moment tensor are a factor of 10 smaller than the other components. This fact coupled with the inability to model the transverse observations (correlation coefficients 0.25-0.38) allows one to speculate that the cause of this radiation is not a single coherent source. An alternate explanation is that the radiation is a result of scattering in the test bed. Site characterization which included trenching near the test bed has isolated discontinuous caliche beds in the shallow structure. These caliche beds, although randomly distributed with scale lengths of 0.5 to 1.0m, exhibit a two-fold increase in P velocity over surrounding material.

IMPLICATIONS AND CONCLUSIONS

The utility of carefully designed seismic experiments in characterizing explosive sources has been illustrated. This experiment, a small scale chemical explosion, has allowed the seismic source as determined by an inversion procedure to be related to observed physical processes in the source region. The data inside a scaled range of $215 \text{ m/kt}^{1/3}$ has experimentally shown the growth of the source pulse. The new result that has been supported by this unique data set is the quantification of the spall process as a contribution to the equivalent elastic seismic source. The potential for quantifying effects such as source size, source depth, and source medium are great in similar experiments.

The utilization of the moment tensor source representation in an inversion procedure has been validated by the analysis of this new data set. The selection of the appropriate velocity model for synthetic seismogram calculation introduces an absolute factor of 2-3 variation in the overall source strength when comparing the best homogeneous half-space to a complete plane-layered model.

The explosion source model which has resulted from this study consists of two distinct parts. The first source is the initially spherical explosion. This component dominates

the moment rate tensor and is between 50-80 ms in duration. The second part of the source is the cylindrically symmetric spall which results from the interaction of the initially spherical compressive wave with the free surface. Through the inversion and the analysis of the nonlinear data, this spall process creates a cylindrically symmetric source delayed in time from the initial compressive wave. In addition, the spall process adds a longer period component to the source (in this case 200 ms). This frequency shift is controlled by the time near surface layers remain in free fall once tensile failure has occurred. The amount of frequency shift will be dependent upon the tensile strength of the near surface layers. The spall part of the explosion is characterized by the diagonal moment tensor elements $M_{11} = 1$, $M_{22} = 1$, $M_{33} = 2$. This secondary source because of its longer period components is maximized on the moment tensor. The M_{33} component of the layered inversion predicts a source strength of 1.03×10^{16} dyne-cm. This value compares with estimates from the spall zone in the nonlinear regime of 2×10^{16} dyne-cm. Not only is the timing and spatial characterization of this secondary source validated by the inversion but also its absolute size.

This study motivates similar analysis on nuclear sources to attempt to separate the various source components. Source inversions utilizing linear data from nuclear explosions has been reported but without the confirming evidence of the

nonlinear data. Figure 24 contains the moment tensors from the nuclear explosion FARM detonated in tuff (Stump and Johnson, 1984). This source has an initial pulse followed 1.5 s by the cyclic long period energy. One possible interpretation for this secondary source which is largest on the M_{33} component is that it is a result of spall. There is a clear need for data from within the spall zone of nuclear explosions to further constrain such models. There is evidence from aerial photography of nuclear explosions (Walker, 1982) that the spall process is not always cylindrically symmetric. Such a process would no longer be represented by a moment tensor with the ratio $M_{11} = 1$, $M_{22} = 1$, $M_{33} = 2$. This variation is hypothesized to result from lateral variations in velocity structure, source asymmetries, three-dimensional surface structures, and variations in material strength.

This study of a small scale chemical explosion appears to have significant implications on the source characterization of nuclear sources. These conclusions need to be checked against observational data. Finally in the case of large nuclear explosions the teleseismic body wave contribution of spall needs to be addressed.

References

Aki, K. and P. G. Richards (1980). **Quantitative Seismology, Theory and Methods**, Vol. 1 and 2, W. H. Freeman and Company, San Francisco.

Aki, K. and Y. B. Tsai (1972). Mechanism of Love-wave excitation by explosive sources, *J. Geophys. Res.* 77, 1452-1475.

Bakun, W. H. and L. R. Johnson (1973). The deconvolutin of teleseismic P waves from explosions Milrow and Cannikin, *Geophys. J. Roy. astr. Soc.* 34, 321-342.

Burdick, L. J., T. Wallace, T. Lay (1984). Modeling near-field and teleseismic observations from the Amchitka test site, *J. Geophys. Res.* 89, 4373-4388.

Day, S. D., N. Rimer, and J. T. Cherry (1983). Surface waves from underground explosions with spall: analysis of elastic and nonlinear source models, *Bull. Seis. Soc. Am.* 73, 247-264.

Douglas, A. and J. A. Hudson (1983). Comments on "Time Functions Appropriate for Nuclear Explosions," by L. J. Burdick and D. V. Helmberger and "Seismic Source Functions

and Attenuation from Local and Telesismic Observations of the NTS Events Jorum and Handley," by D. V. Helmberger and D. M. Hadley, *Bull. Seis. Soc. Am.* 73, 1255-1264.

Flynn, E. (1986). Effects of Source Depth on Near Source Seismograms, M. S. Thesis, Southern Methodist University, Dallas, Texas.

Lay, T., T. C. Wallace, and D. V. Helmberger (1984). The effects of tectonic release on short-period P waves from NTS explosions, *Bull. Seis. Soc. Am.* 74, 819-842.

Mueller, R. A. and J. R. Murphy (1971). Seismic characteristics of underground nuclear detonations, Part I. Seismic spectrum scaling, *Bull. Seis. Soc. Am.* 61, 1675-1692.

Peppin, W. A. (1977). A near-regional explosion source model for tuff, *Geophys. J. Roy. astr. Soc.* 48, 331-349.

Rodean, H. C. (1981). Inelastic Processes in Seismic Wave Generation by Underground Explosions, p97-190.

Identification of Seismic Sources - Earthquake or Underground Explosion, Ed. by E. Husebye and S. Mykkeltveit, D. Reidel, Holland.

Stump, B. W. and R. E. Reinke (1982). "Spall-Like Waveforms Observed in High-Explosive Testing in Alluvium," AFWL-TR-82-15, Air Force Weapons Laboratory, Kirtland AFB, New Mexico, 122p.

Stump, B. W. (1983). Source characterization of buried surface bursts, *Bull. Seis. Soc. Am.* 73, 979-1003.

Stump, B. W. and L. R. Johnson (1984). Near-field source characterization of contained nuclear explosions in tuff, *Bull. Seis. Soc. Am.* 74, 1-26.

Stump, B. W. and R. E. Reinke (1984). Spall observations and mechanisms in alluvium, *J. Geophys. Res.* 89, 11495-11506.

Stump, B. W. (1985). Constraints on explosive sources with spall from near source waveforms, *Bull. Seis. Soc. Am.* 75, 361-377.

Stump, B. W. and R. E. Reinke (1986). Experimental seismology: Insitu source experiments, accepted *Bull. Seis. Soc. Am.*

Stump, B. W. (1986). Resolution of complex explosive source functions in the frequency domain, submitted *Geophys. J. Roy. astr. Soc.*

Viecelli, J. A. (1973). Spallation and the generation of surface waves by an underground explosion, J. Geophys. Res. 78, 2475-2487.

von Seggern, D. and R. Blandford (1972). Source time functions and spectra for underground nuclear explosions, Geophys. J. Roy. astr. Soc. 31, 83-97.

Figure Captions

Figure 1a: Sample refraction result from test area.

b: Model developed from refraction data.

Figure 2: Final layered velocity model for calculation of reflectivity seismograms.

Figure 3: Reflectivity Green's functions convolved with the CHEAT instrument response. The radial (R) and vertical (Z) explosion (EX) Green's functions as well as the transverse (T) dip-slip (DS) Green's functions are given.

Figure 4: The observed and calculated velocity records at station 3 (50 m range) from the inversion utilizing all of the data and the range varying Green's functions.

Figure 5: Isotropic moment rate tensor (\dot{M}_{TRN}) and moment tensor (M_{TRN}) from the CHEAT inversions utilizing all data between 50-150m along with the single half-space, range varying half-space, and reflectivity Green's functions.

Figure 6: The spectral characterization of the isotropic moment tensor from the single half-space, all data inversion.

Figure 7: Comparison between the isotropic moment rate tensor and the velocity record observed at 18.35m range.

Figure 8: The moment rate tensor (a) and moment tensor (b) from the inversion of all the linear data utilizing the range varying half-space Green's functions. All moments are relative to the M_{33} component which has the peak amplitude of 10.4×10^{27} dyne-cm/s in (a) and 5.10×10^{26} dyne-cm in (b).

Figure 9: The moment tensors, including the isotropic component, for the nuclear explosion FARM. The numbers above the traces should be multiplied by 10^{23} to yield dyne-cm.

Acknowledgements

The review of Roy Berger added greatly to the paper. Success in the field program and extensive discussion of the source characterization is attributable to Robert Reinke. This work was supported under Grant AFOSR-84-0016.

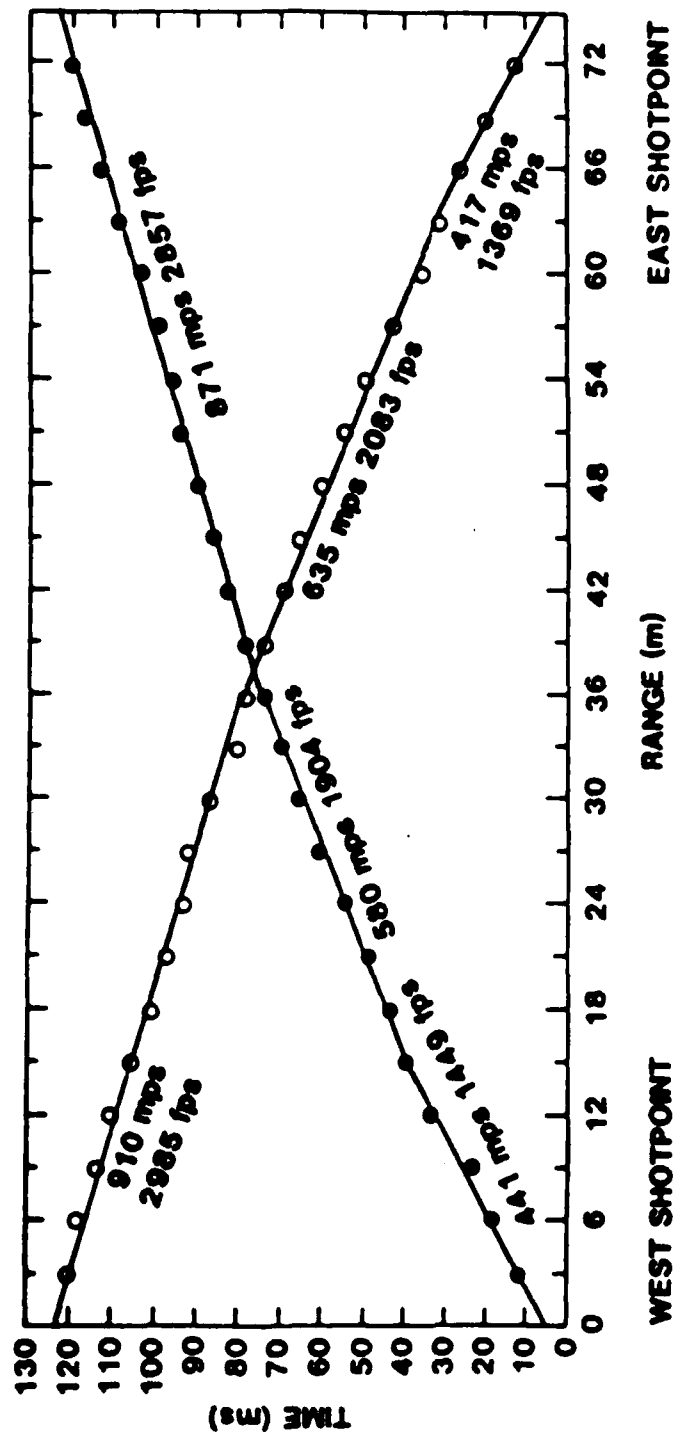


Figure 1a

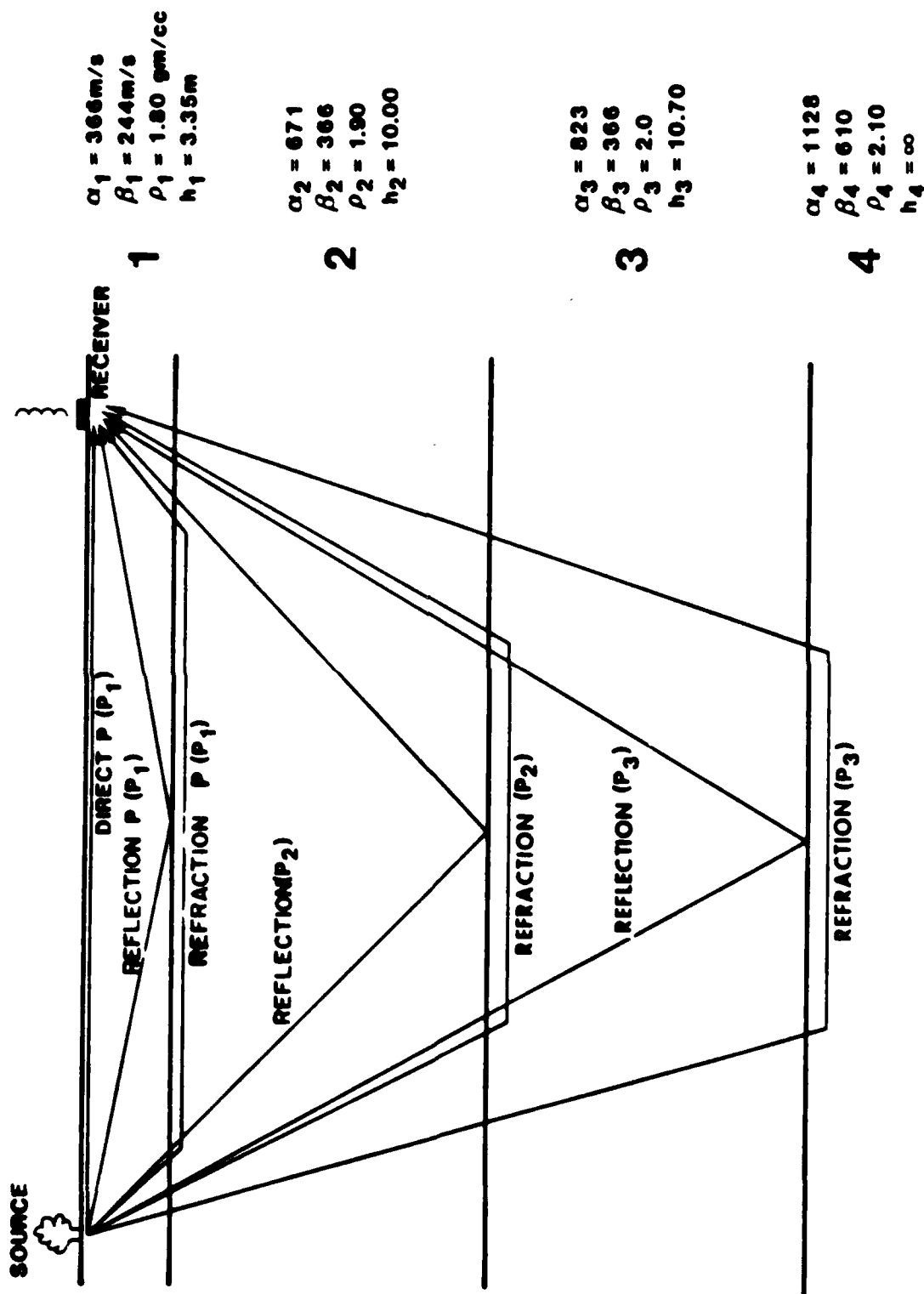


Figure 1 b

CHEAT LAYERED VELOCITY MODEL

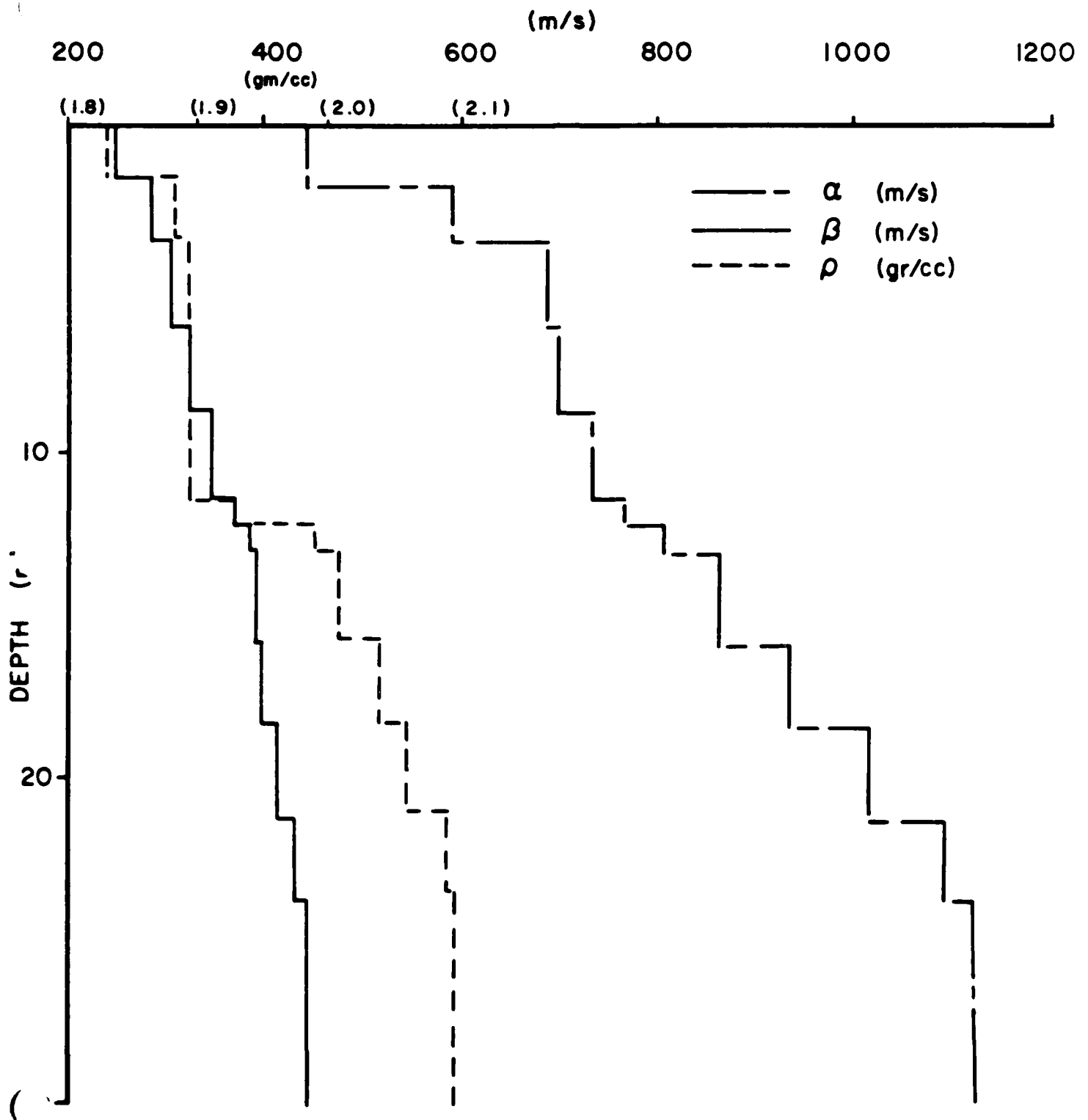


Figure 2

REFLECTIVITY MODEL

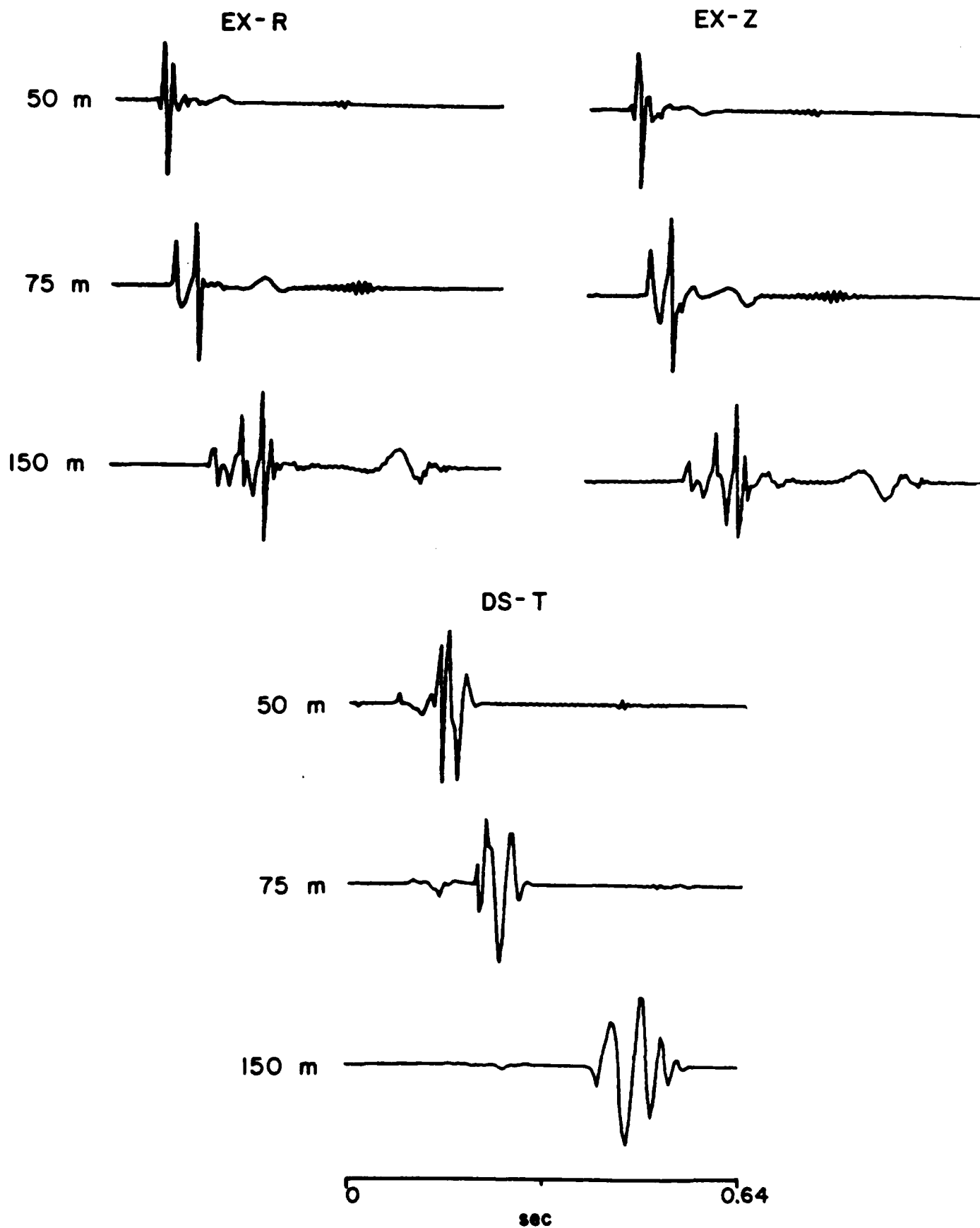


Figure 3
20

CHEAT FITS STATION 3

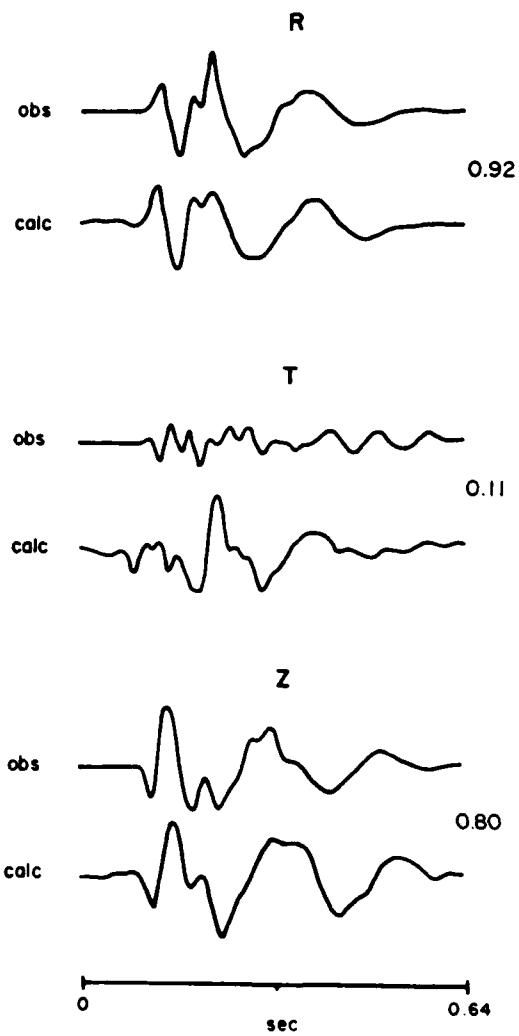


Figure 4

ISOTROPIC MOMENT TENSORS

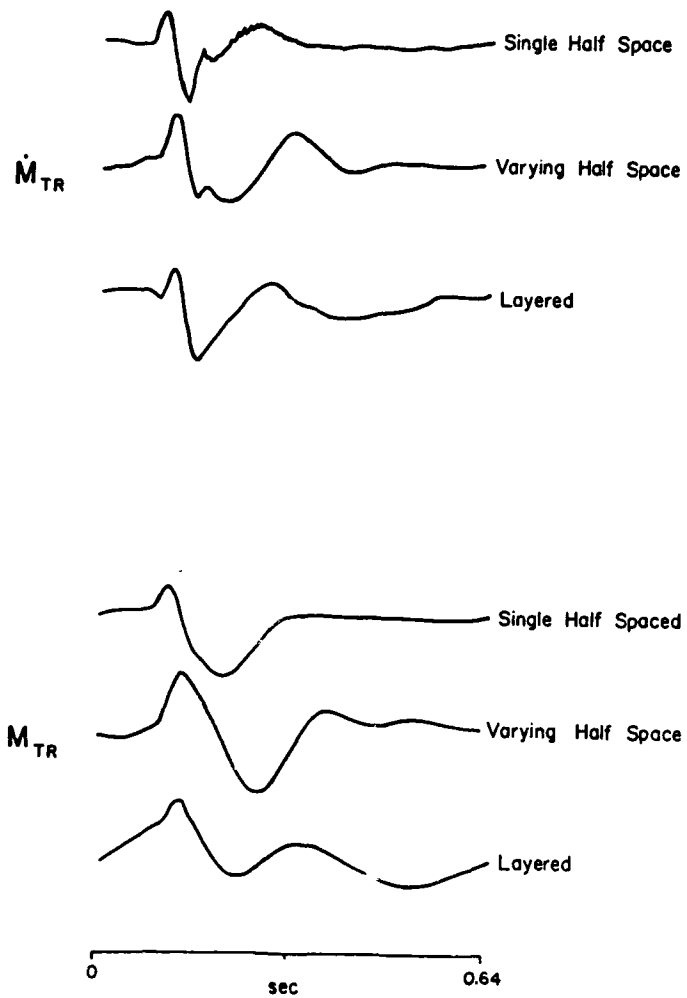


Figure 5
22

CHEAT $M_{tr}(all)$
SPECTRUM

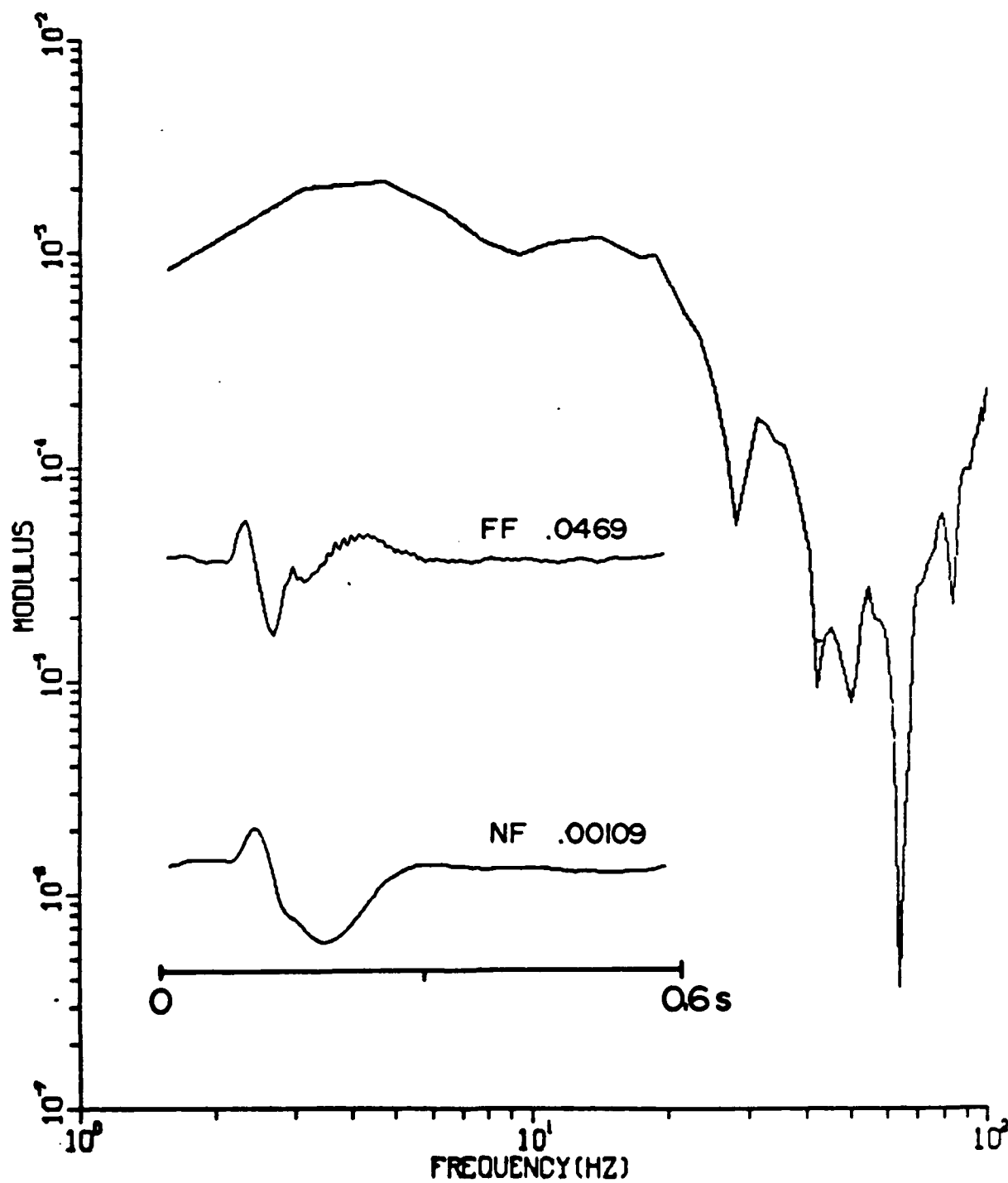


Figure 6

**ISOTROPIC SOURCE AND NEAR
SOURCE VELOCITY COMPARISON**

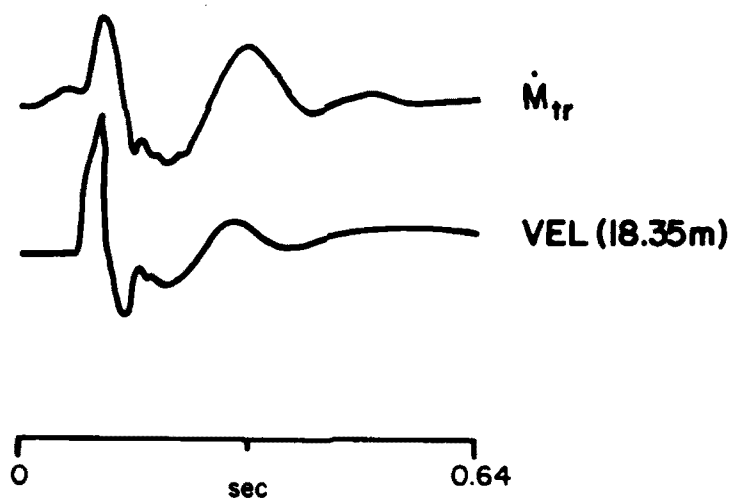


Figure 7

FAR-FIELD MOMENT TENSORS

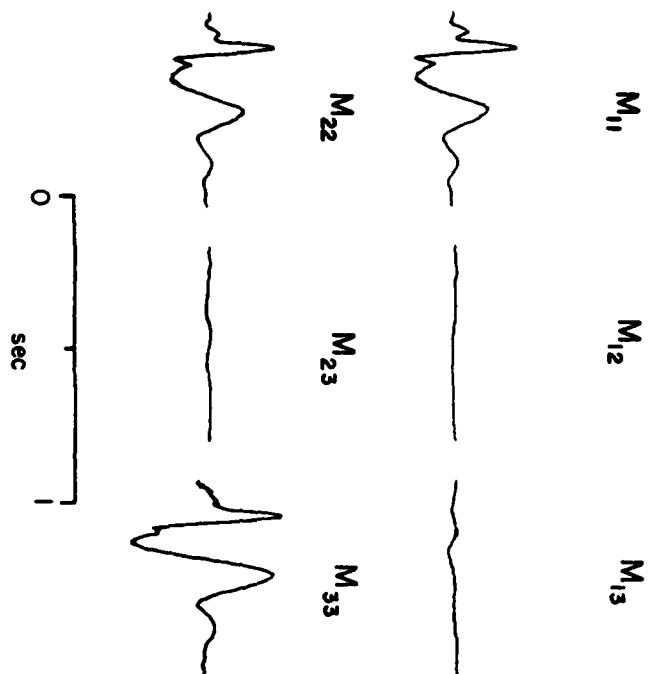
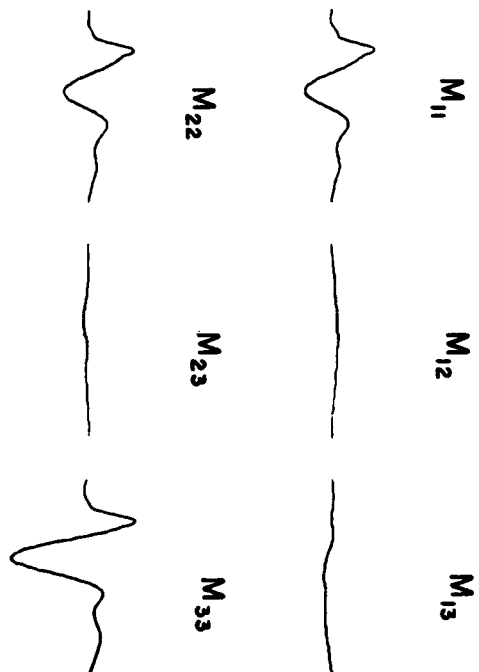


Figure 8a

NEAR-FIELD MOMENT TENSORS



0
sec

Figure 8b

FARM

M



TR

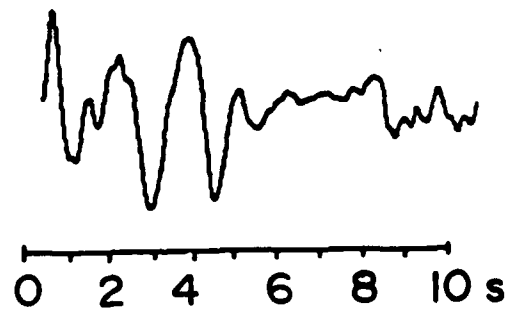


Figure 9

Table 1

All ranges	920 m/s	350 m/s	1.9 gm/cc
------------	---------	---------	-----------

Each range

50	558	284	1.9
60	582	312	1.9
75	617	343	1.9
100	689	390	1.9
150	788	452	1.9

Table 2:
Correlation Coefficients

		<u>R</u>	<u>T</u>	<u>Z</u>
Single Half-Space				
Model	50-150m	.8122	.2503	.6402
Range Varying Half	50-75m	.8884	.3740	.8910
Space Model	50-150m	.7560	.2672	.6452
Layered Velocity	50-75m	.9360	.3797	.8675
Model	50-150m	.8494	.2812	.6008

Table 3

Moment From CHEAT Inversions
Nearfield - 10^{16} dyne-cm
(Farfield - 10^{17} dyne-cm/s)

INVERSION	M ₁₁	M ₁₂	M ₁₃	M ₂₂	M ₂₃	M ₃₃	M _{TR}	ψ (m ³)
50-60m Single Half- Space	13.6 (47.4)	0.279 (0.312)	1.44 (1.21)	13.3 (47.2)	0.798 (0.733)	19.2 (50.0)	15.3 (48.2)	.757
50-150m Single Half- Space	11.3 (56.2)	0.506 (0.515)	0.654 (0.889)	10.9 (55.7)	0.326 (0.628)	17.1 (57.4)	13.1 (56.4)	.649
50-75m Varying Half-Space	2.78 (7.80)	0.426 (0.299)	0.484 (0.827)	2.89 (0.836)	0.249 (0.224)	4.51 (9.59)	2.88 (8.35)	.354
50-150m Varying Half-Space	2.76 (8.23)	0.384 (0.296)	0.474 (8.54)	2.85 (8.54)	0.310 (0.402)	5.10 (10.4)	2.87 (8.68)	.288
50-75m Layered	1.11 (2.54)	0.479 (0.259)	0.519 (0.424)	1.20 (2.56)	0.135 (6.19)	1.75 (3.17)	1.35 (2.76)	.106
50-150m Layered	0.851 (2.41)	0.144 (0.137)	0.175 (0.187)	0.928 (2.31)	0.1012 (0.147)	1.03 (2.57)	0.936 (2.42)	.0733

PAPER 3

EFFECTS OF SOURCE DEPTH ON

NEAR SOURCE SEISMOGRAMS

Elizabeth C Flynn

Department of Geological Sciences
Southern Methodist University
Dallas, Texas 75275

Brian W Stump

Department of Geological Sciences
Southern Methodist University
Dallas, Texas 75275

ABSTRACT

Source depth effects are examined for five 115 kg TNT explosions buried at depths ranging from the optimum cratering depth of 1.8 m to the fully contained depth of 11.5 m. Data were recovered at near source ranges from 17 to 228 m. The waveforms are dominated by P and Sv-Rayleigh energy. Depth effects are evident in the increase of P to Sv-Rayleigh amplitude ratios and in the two-fold increase of high frequency energy for the deeper sources. Theoretical propagation depth effects are modeled by Green's functions calculated for a velocity gradient which approximates the velocity structure of the experimental site. The effects of depth on the explosion source function are predicted using the scaling laws of Mueller and Murphy (1971). These models did not reproduce the observed two-fold increase of high frequency energy. The discrepancy between the model and observations is attributed to increased coupling of high frequency P wave energy for fully contained sources. Energy calculations confirm that the shallowest event coupled 40% and the fully contained event 80% of the total seismic energy into the P wave. Source coupling efficiencies ranged from 0.7-1.0% for the near surface source to 1.5-2.9% for the fully contained explosion.

INTRODUCTION

The object of this study is a quantitative and theoretical investigation of the physical processes which act as a function of source depth in producing near-source explosion waveforms. An understanding of these processes is essential to the problem of characterizing the depth of the seismic event. The ability to determine source depth is important to discrimination and yield studies where estimates of yield are dependent on the burial depth of the source (Mueller and Murphy, 1971).

The problem of characterizing the depth of a seismic event is one which involves two broad aspects; propagation effects which act as a function of depth, and changes in the nature of the source function as its burial depth changes. A spherically symmetric explosion is a good source of compressional wave energy, while a cylindrically symmetric explosion, one that is close to the free surface and only partially contained, is a richer source of Sv and Rayleigh wave energy. Thus there is a relationship between the P and Rayleigh wave energy of an explosion that is dictated to some extent by the burial depth of the event.

The free surface contributes the most important propagation effects to the source depth problem. Rayleigh wave excitation is directly attributed to the presence of the free surface boundary. The source's proximity to this boundary affects its ability to excite surface wave energy. The dependence of Rayleigh amplitudes on earthquake source depths has been observed by many authors. Eissler and Kanamori (1986) estimated source depths of Hawaiian earthquakes from the ratios of body to surface wave amplitudes. On a smaller scale, Dobrin et al (1951) quantified the decay of Rayleigh amplitudes for explosions buried from 20 to 300 feet. The Rayleigh decay is predominantly a function of the change in propagation path with depth, but for very shallow sources an increase in source coupling serves to increase the Rayleigh amplitude with depth.

The interference of pP and other free surface reflections with the direct P arrival is another phenomenon dependent on the depth of the source. The free surface reflection creates interference phenomena that present difficulties in the frequency domain where spectral techniques are used to estimate various source parameters (Langston, 1978).

With both source and propagation effects contributing a depth dependence to the P and the surface wave, the relationship between these two arrivals can be a complicated function of source depth. This study is intended to quantitatively assess the effects of the depth of the source on P and Rayleigh arrivals, and to distinguish the effects of depth on the source function and the propagation terms.

This study is unique to those mentioned above for two reasons. First, this investigation focuses on near-source observations for which the scale is much smaller although the physical phenomena are the same. The near-source observations are dominated by upgoing rather than downgoing energy, and are thus strongly influenced by the free surface and near surface structure. Second, the experimental configuration is well controlled; the source depths and recording distances are accurately known, as is the velocity structure of the experimental site. The data set provides not only depth-dependent observations, but also range dependent observations which allow the characterization of spatial propagation effects.

The separation of source and propagation effects is attempted by matching observed depth effects with theoretical depth effects. Propagation effects are calculated by theoretical Green's functions. Source effects for fully contained events are calculated from the depth effects proposed by Mueller and Murphy (1971). The increase in source coupling with increased containment is used in the calculation of total seismic energy as a function of burial depth.

AD-A181 092

DETERMINISTIC AND STOCHASTIC WAVEFIELD IN THE
NEAR-FIELD FROM EXPLOSIVE S... (U) SOUTHERN METHODIST
UNIV DALLAS TX DEPT OF GEOLOGICAL SCIENCES..

2/3

UNCLASSIFIED

B W STUMP ET AL. 03 APR 87 SMUG-3

F/G 8/11

NL



MICROCOPY RESOLUTION TEST CHART
NATIONAL BUREAU OF STANDARDS-1963-A

OBSERVATIONAL DATA

Range Effects

The data set was generated by five 115 kg chemical explosions fired in dry alluvium and buried from 1.8 to 11.5 m below the free surface. The explosions ranged from partially contained, 1.8 m being the optimum cratering depth, to a fully contained event at a depth of 11.5 m. Radial (to the source) and vertical acceleration was recorded at 17, 37, 73, and 228 m from each of the five events. The data was sampled at 2000 samples per second. The recording ranges and source depths are summarized in Figure 1. The velocity waveforms for one range (73 m) are shown in Figure 2 which displays the radial and vertical components for each explosion. The complete data set is displayed in Flynn (1986).

The waveforms are dominated by a P phase and a Sv-Rayleigh phase. The Sv and Rayleigh arrivals are treated as one because at the closest ranges their arrival times are separated by only a few hundredths of a second, while the Sv-Rayleigh pulse width is on the order of 0.2 s. In Figure 2 the Sv-Rayleigh pulse is distinguished by a large amplitude and a shift to longer periods relative to the P arrival. Propagation effects at the farthest range (228m) have separated the P and Sv-Rayleigh phases by some intermediate multipathed arrivals, but as close as 37 and 73 m the waveforms consist almost entirely of the P and the Sv-Rayleigh phases (Figure 4a). At the closest range (17 m) even the P and Sv-Rayleigh phases are not completely separated.

The dominance of P and Sv-Rayleigh motion is verified by particle motion diagrams. In Figure 3 the 228 m radial and vertical components are plotted with particle motions for the indicated P and Sv-Rayleigh windows. Particle motion in the P window is rectilinear, with the radial and vertical motions roughly equal. In the indicated Sv-Rayleigh window, the radial and vertical components have fallen out of phase and particle motion has become retrograde, representing surface wave motion.

The effect of range in separating the body and surface wave phases is illustrated in Figure 4 by the particle motions of a single event. At 17 m the P wave motion is not strongly linear, nor is it sharply distinguished from the onset of the Sv-Rayleigh wave. The separation of body and surface

waves becomes more distinct with the evolution of the strongly linear and retrograde motions observed at the more distant ranges.

The effect of propagation distance is evident in the decay of the P and Sv-Rayleigh amplitudes. In Figure 5 the decay rates of the phases are estimated by a linear least-squares fit to the log of the amplitude versus the log of the range. The P and Sv-Rayleigh waves display slightly faster decay rates than are expected for spherical and cylindrical wavefronts respectively. Radial P decays as $r^{(-1.6)}$, vertical P as $r^{(-1.3)}$, and radial Rayleigh decays as $r^{(-1.0)}$, vertical Rayleigh as $r^{(-0.9)}$.

OBSERVATIONAL DATA

Depth Effects

Time Domain: In the time domain the P and Sv-Rayleigh arrivals were identified by the particle motion diagrams. The vertical P wave amplitude increases by two to six fold (depending on range) from a source depth of 1.8 m to a depth of 11.5 m (Figure 6). The radial P wave amplitude shows a less pronounced depth dependence, increasing by 1.5 to 3 fold over the range of source depths. The Sv-Rayleigh waves display very little depth dependence, decreasing by 20 to 40% over the range of source depths. The ratios of P to Sv-Rayleigh amplitudes that are plotted in Figure 7 are largely a reflection of the depth dependence of the P wave amplitudes.

Frequency Domain: The displacement spectra for each event as recorded at 73 m are given in Figure 8. The signal is above background noise in the 2 to 60 hz band. The displacement spectra at each range are characterized by a long period level and a corner frequency that were estimated from an overlay of a four pole Butterworth filter. From Table 1 it is seen that an average 2 or 3 hz increase in corner frequency accompanies the increase of source depth from 1.8 to 11.5 m. No appreciable increase or decrease in the long period level of the spectra occurs with changing source depth.

A comparison in Figure 9 of the spectra of the deepest and the shallowest events illustrates the change in spectral shape that coincides with an increase of source burial depth. The higher corner frequency of the deeper event is reflected in the increase of high frequency spectral amplitudes. At the long periods the two spectra converge.

Spectral ratios of the deepest to the shallowest sources were calculated in the frequency domain and smoothed by a five point running mean (Figure 10). The increase in high frequency spectral amplitude for the deeper event is represented by a spectral ratio greater than one. At low frequencies (<10hz) the spectral ratios are not consistently smaller or greater than one, but at high frequencies (10-40hz) the deepest event has a factor of two increase in spectral amplitude. Time domain windows of the P and Sv-Rayleigh waveforms and Fourier analysis identifies the 10-40 hz band as the P contribution and the 4-10 hz band as the Sv-Rayleigh contribution (Flynn, 1986). The increase of the

10-40 hz spectral amplitudes that accompanies an increase of source depth agrees with the time domain P amplitudes in suggesting a larger contribution of P wave energy for the deeper events. The low frequency band of 4-10 hz lacks a consistent increase or decrease of spectral amplitudes with depth, suggesting that for the events under study the amount of Sv-Rayleigh energy produced is not a strong function of source depth.

MODELING OF SOURCE AND PROPAGATION EFFECTS

The depth effects that have been outlined in the time and frequency domains contain both source and propagation depth effects. The observations can be expressed in general terms as a convolution of the source function with the propagation path effects, or in the frequency domain as;

$$U(f) = G(f) S(f) \quad (1)$$

where U are the observations, S the source function, and G the Green's function or impulse response of the medium.

Source Effects: In an attempt to create a reference against which the data can be judged, the Mueller-Murphy (1971) source model was used to predict source effects for source depths between 1.8 and 11.5 m. This model is for fully contained sources and acts as a standard against which the cratering explosions can be compared. Shown in Figure 11 are the predicted effects of source depth on the far-field source potential. From 1.8 to 11.5 m source depth, the corner frequency of the source is predicted to increase by approximately a factor of two, a much larger increase than observed in the data. The long period level of the spectra drop by a factor of 2 from the 1.8 to the 11.5 m source. The observations show no consistent decrease in the long period level (Table 1). The spectral ratio of the 1.8 to 11.5 m sources has a two-fold increase in the high frequency amplitudes (Figure 12) and is comparable to the observed amplitude ratios (Figure 10). The observations appear to demonstrate some of the predicted source depth effects, but they lack other of the predicted source effects, namely the drop in long period level.

Propagation Effects: The contribution of propagation effects to the depth-dependent observations can be tested with synthetic waveforms generated by idealized propagation models. The velocity model which best fit the test site (Stump and Reinke, 1982) consisted of compressional velocity, shear velocity, and density which increased smoothly from surface values of 375 m/s, 244 m/s, and 1.67 gm/cc respectively to values of 1128 m/s, 610 m/s, and 2.1 gm/cc in the half-space at twenty five meters depth (Figure 13).

Green's functions were calculated by a modified reflectivity method and convolved with the theoretical source function for the 11.5 m depth. The resulting waveforms are given in Figure 14. The P amplitude can be seen to increase with source depth relative to the Sv-Rayleigh amplitude. The model produces a factor of 1.7 to 4.0 increase in P amplitude with source depth which is comparable to the increase of observed P amplitudes (2 to 6). The Sv-Rayleigh amplitude decreases by a factor of 3 to 5 which is more pronounced than the 20-40% decrease that was observed.

In the frequency domain the corner frequency decreases by approximately 2 hz which is unlike the shift to higher frequencies observed in the data. The long period level displays a slight increase with source depth.

In summary, the Green's functions can account for an increased P wave amplitude with depth, but they can not account for an increasing corner frequency or a non-decaying long period level, and they produce an Sv-Rayleigh wave that is too strongly depth-dependent.

Combined Source/Propagation Effects: Predicted source depth effects were combined with theoretical propagation depth effects by convolving the Green's functions with the appropriate Mueller-Murphy source function derived for each source depth. The Mueller-Murphy predictions are strictly for fully contained sources. The spectral ratios resulting from these combined source and propagation effects are given in Figure 15. The shift of source energy to high frequencies is roughly balanced by the decrease in high frequency energy for the deeper propagation path. At long periods the spectral ratio is slightly greater than 1.

Comparing the observed (Figure 10) and calculated (Figure 15) spectral ratios it is evident that the observations contain depth effects beyond those that can be accounted for by theory. The depth effects that were not satisfactorily modeled include the two to one spectral ratio at high frequencies and, going back to the amplitude data, the almost negligible decay of Sv-Rayleigh amplitudes with depth.

The physical depth effect that is addressed by neither the Green's functions nor the Mueller-Murphy source scaling laws is the effect of moving from a partially contained to a fully contained burial depth. Based upon the modeling exercise it is concluded that the fully contained source generates more high frequency energy as a result of an

increase in coupling over the near-surface source. While an improvement in the source coupling efficiency increases the high frequency content, some increased coupling of energy over the entire bandwidth is necessary to offset the strong decay of Sv-Rayleigh amplitudes with depth in the Green's functions. In order to quantify the increased coupling efficiency with increased burial depth, the total seismic energy in the observed waveforms is calculated as a function of source depth.

ENERGY CALCULATIONS

Attenuation and Q

Energy as a function of depth is best quantified after spatial dependencies have been removed from the data. The data set lends itself to an empirical determination of range dependent propagation effects which are represented as the spatial decay of P and Sv-Rayleigh energy. The P and Sv-Rayleigh energy displays a range dependence which is greater than simple geometrical spreading. If the geometrical spreading rates of the P and Sv-Rayleigh waves are removed, the remaining spatial dependence, the apparent attenuation, can be represented as a decaying function of range;

$$A = A_0 \exp(-\alpha r) \quad (2)$$

where α is the apparent attenuation and r is the range. The apparent attenuation is a combination of attenuation mechanisms such as scattering and intrinsic attenuation. The apparent attenuation is estimated from the seismic energies which are calculated from the observational velocity records.

Calculation of the seismic energy begins with the energy flux (Wu, F., 1966 and Perret, 1973);

$$F = \rho c \int [v(t)]^2 dt \quad (3)$$

where F is the energy flux in ergs per square centimeter, ρ is the density (gm/cc), and c is the propagation velocity (cm/s), and $v(t)$ is the recorded particle velocity (cm/s).

The energy flux, F , was calculated for both the P and Sv-Rayleigh arrivals. The P arrival corresponds to the time duration over which the particle motion was linear; the Sv-Rayleigh arrival was marked by the onset of retrograde motion.

Using Parseval's Theorem the energy flux was calculated in the frequency domain;

$$\int_{\tau_1}^{\tau_2} [v(t)]^2 dt = 1/(2\pi) \int_{\omega_1}^{\omega_2} [V(\omega)]^2 d\omega \quad (4)$$

where $V(\omega)$ is the Fourier transform of $v(t)$.

The advantage of calculating the energy flux in the frequency domain is that the apparent spatial attenuation can be derived for each of the two frequency bands considered, a P band and the Sv-Rayleigh band, where the apparent attenuation is assumed to be frequency independent within each of these bands.

The P and Sv-Rayleigh time windows were tapered and transformed, padding to 256 points for the P window and 512 points for the Sv-Rayleigh window. The function $[V(\omega)]$ is plotted in Figure 16 for the P and Sv-Rayleigh windows. The P wave energy is peaked in the 10-40 hz band and the Sv-Rayleigh energy is in the 4-10 hz band. The amplitude of the P wave spectrum has fallen off by nearly a factor of ten at 40 hz which means that $[V(\omega)]$ has fallen off by a factor of 100. The P wave energy was taken to be the sum of the energies contributed by frequencies between 8 and 40 hz. The Sv-Rayleigh energy is determined by summing energy in the 4-12 hz band. Inclusion of a wider frequency band changes the energy estimates by no more than 5%.

The total energy in a spherical wavefront becomes;

$$E = 4\pi R^2 F \quad (5)$$

where E is energy in ergs and R is range in centimeters. For cylindrical waves the total energy becomes:

$$E = 2\pi R h F \quad (6)$$

where h is the depth of cylindrical wavefront and is derived for Rayleigh waves in Appendix 1.

The total spherical (P) and cylindrical (Sv-Rayleigh) energy as determined from the observational data is plotted in Figure 17. The decay of the energy with range is called the apparent attenuation. The linear slope of the log energy plot is the decay constant, α , in equation 2 and represents the combination of all remaining mechanisms of spatial attenuation.

Table 2 lists the least-squares values of α and their linear correlation coefficients. From the apparent attenuation a value of Q can be calculated by;

$$A = A_0 \exp(-\alpha r) = A_0 \exp(-wr/2cQ) \quad (7)$$

$$Q = w/2c\alpha \quad (8)$$

The Q values calculated from the P and Sv-Rayleigh attenuation rates are given in Table 3. For the radial component Q ranged from 5 to 25 for P and 10 to 30 for Sv-Rayleigh. For the vertical component Q ranged from 15-90 for P and 18-54 for Sv-Rayleigh.

Energy as a Function of Depth

The α values are used to correct for the final range dependence in the energy calculations. The range corrected P and Sv-Rayleigh energies are plotted as a function of source depth in Figure 18. The range corrections are particularly effective for the radial component where the energies calculated at each range for a given depth differ at most by a factor of three. The vertical P wave energies still contain some scatter for the different ranges with energies differing by nearly a factor of ten at a given depth.

Normalizing the P and Sv-Rayleigh energies to the sum total of P plus Sv-Rayleigh energy, it can be seen from Figure 19 that the shift in energy distribution from the shallowest to the deepest source is a shift from Sv-Rayleigh to P energy. The average recording of the shallowest event contains 40% P wave and 60% Sv-Rayleigh energy. The average recording of the 3.9 and 11.5 m events contained 72% and 83% P wave energy respectively. The percentage P wave energy increases rapidly from 1.8 to 3.9 m source depth, and more slowly to the final depth of 11.5 m.

The increase in P wave energy from 40 to 83% of the total seismic energy confirms that the fully contained source is a more efficient generator of P wave energy than the near-surface source. The absolute energy increases from an average of 8×10^{12} ergs for the shallowest event to an average of 22×10^{12} ergs for the fully contained event. Since all the events were of the same size, with a yield of 10^{15} ergs (Meyer, 1981), the increase in total seismic energy corresponds to an increase in source coupling

efficiency from 0.7 to 1.0% for the near-surface source to between 1.5 and 2.9% for the fully contained event (Table 4). For nuclear explosions in alluvium Perret (1972) obtained seismic coupling efficiencies between 0.05 to 0.15% while other materials such as wet tuff and salt gave efficiencies of 2 to 3%. Mueller (1969) determined coupling efficiencies of 0.32% for the cratering shot Schooner in tuff while the contained explosion Benham, also in tuff, gave a coupling efficiency of 6.1%. In this study a 3 to 4 fold increase in coupling from the cratering to the fully contained explosion was determined.

CONCLUSIONS

Depth effects fall under two broad categories; source depth effects and propagation depth effects. The separation of the source and propagation depth effects has been completed with the help of theoretical source and propagation models. The data set to which this analysis was applied is unique for two reasons; the small scale of the experimental configuration and the control of source depths and recording ranges.

Observations at several distances allowed the wave field to be quantified in terms of its spatial characteristics, namely the dominance of P and Sv-Rayleigh motion, the amplitude decay of these two arrivals, and their spatial attenuation rates. The source depths spanned the range from partially to fully contained, corresponding to source symmetries which vary from cylindrical to spherical. The dominance of P and surface wave motions is therefore important to this investigation because the relationship between the spherical P and the cylindrical Sv-Rayleigh arrivals is in part a measure of the changing symmetry of the source with increasing overburden. The P and Sv-Rayleigh arrivals were shown to consist of individual frequency bands, 4 to 10 hz for the Sv-Rayleigh wave and 10 to 40 hz for the P wave. Together these arrivals comprise the bandwidth of the data. Thus the P and Sv-Rayleigh arrivals were also used as a measure of the relative coupling of high to low frequencies as a function of source depth.

The observed depth effects included a 2 to 5 fold increase in P wave amplitude and a 1.5 fold decrease in the Sv-Rayleigh amplitude over the range of source depths, and a shift to higher frequencies with increasing depth. The shift to higher frequencies was consistent with the predicted effects of depth in the Mueller-Murphy source models.

The increase in P amplitude relative to Sv-Rayleigh amplitude with depth was modeled as a theoretical propagation effect. The gradient velocity model accounted for observed increases in P amplitudes but was unable to match the slow decay of surface wave amplitude with increasing source depth.

Combined theoretical source and propagation effects predict a decrease in long period spectral level with increasing source depth. The absence of a significant drop in observed long period levels is attributed to increased source coupling efficiency with source depth. The failure of observed Sv-Rayleigh amplitudes to decay as predicted is also attributed to increased source coupling since the long period part of the spectrum is measured from the amplitude of the Sv-Rayleigh wave. The source coupling efficiency increased from 0.7-1.0% for the near surface explosion to 1.5-2.9% for the fully contained explosion.

Another effect of the propagation path was to decrease the corner frequency by about 2 hz. However, the predicted source effect contributes a substantial increase of corner frequency which overrides the propagation effects and produces the observed 2 hz increase. The increase of the 10-40 hz P wave energy from 40 to 80% of the total seismic energy quantifies the observed shift to higher frequencies, and identifies the shift as one from surface wave energy to P wave energy as source depth increases.

This investigation has quantified the depth dependence of P and Sv-Rayleigh arrivals from small explosions. A natural extension of this work is to scale the results to earthquakes and large explosions observed at regional distances.

Acknowledgements

The data for this study was made available by the Air Force Weapons Laboratory Civil Engineering Division. The work was supported under Grant AFOSR-84-0016. Thanks to E. Herrin, J. Ferguson, R. Phillips, and R. Reinke for their review of the work.

References

Dobrin, M. B., R. F. Simon and P. L. Lawrence (1951). Rayleigh waves from small explosions, *Trans. Am. Geophys. U.* 32, 822-832.

Eissler, H. K. and H. Kanamori (1986). Depth estimates of large earthquakes on the island of Hawaii since 1948, *J. Geophys. Res.* 91, 2063-2076.

Langston, C. A. (1978). Moments, corner frequencies, and the free surface, *J. Geophys. Res.* 83, 3422-3426.

Meyer, Rudolf (1981). *Explosives*, Verlag Chemie, 2nd Ed., Weinheim, W. Germany.

Mueller, R. A. and J. R. Murphy (1971). Seismic characteristics of underground nuclear detonations, *Bull. Seis. Soc. Am.* 61, 1675-1692.

Perret, W. R. (1972). Seismic-source energies of underground nuclear explosions, *Bull. Seis. Soc. Am.* 62, 763-774.

Perret, W. R. (1973). Seismic source energies of four explosions in a salt dome, *J. Geophys. Res.* 78, 7717-7726.

Stump, B. W. and R. E. Reinke (1982). "Spall-like waveforms observed in high-explosive testing in alluvium," AFWL-TR-82-15, Air Force Weapons Laboratory, Kirtland AFB, New Mexico.

Wu, F. T. (1966), Part I - Lower Limit of the Total Energy of Earthquakes and Partitioning of Energy Among Seismic Waves, Part II - Reflected Waves and Crustal Structures, Ph. D. Thesis, Caltech, Pasadena, California.

APPENDIX 1

Rayleigh amplitude A_r is assumed to be a decaying function of depth, z ;

$$A_r = A \exp(iks z)$$

where $s = (c^2/p^2 - 1)^{0.5}$, k is the wavenumber, $2\pi/\lambda$, and A is a constant. Wavelength $\lambda = cT$ where c is phase velocity and T is period.

The Rayleigh wavefront is approximated by a cylinder of height h . For a particular observation of Sv-Rayleigh amplitude, A_p ,

$$\int_0^{\infty} A_r dz = A_p h$$

where h is some depth given by;

$$\begin{aligned} \int_0^{\infty} A_r dz &= \int_0^{\infty} A \exp(iks z) dz \\ &= A/iks \exp(iks z) \Big|_0^{\infty} \\ &= -A/iks \end{aligned}$$

Figure Captions

Figure 1: Schematic of the experimental configuration. Sources were buried at 1.84, 3.16, 3.96, 5.64, and 11.5 m. Data was recorded at ranges of 17.4, 37.5, 73.2, and 228.6 m.

Figure 2: Observed velocity waveforms. Radial and vertical components are shown for each source depth at the 73 m range. H indicates source burial depth.

Figure 3: Velocity waveforms and corresponding P and Sv-Rayleigh particle motions observed at 228 m. (a) Radial (solid line) and vertical (dashed line) velocity waveforms. H indicates source burial depth. Bars indicate P and Sv-Rayleigh time windows for which particle motions are plotted. (b) Particle motions for the P and Sv-Rayleigh time windows.

Figure 4: Velocity waveforms and corresponding P and Sv-Rayleigh particle motions for the 5.6 m event at four recording ranges. (a) Radial (solid line) and vertical (dashed line) velocity waveforms. Bars indicate P and Sv-Rayleigh time windows. (b) Particle motions for the P and Sv-Rayleigh windows.

Figure 5: Spatial decay of P and Sv-Rayleigh velocity amplitudes. Amplitude decay is approximated by a least squares line on each plot. (a) Radial P and Sv-Rayleigh amplitudes. (b) Vertical P and Sv-Rayleigh amplitudes.

Figure 6: P and Sv-Rayleigh amplitudes as a function of source depth. (a) Radial P and Sv-Rayleigh amplitude versus source depth. (b) Vertical P and Sv-Rayleigh amplitude versus source depth.

Figure 7: Ratio of P to Sv-Rayleigh amplitude as a function of source depth, for both the radial and vertical components.

Figure 8: Displacement spectra for all events recorded at 73 m. 2048 time points were windowed by a 10% cosine taper applied to the displacement waveforms.

Figure 9: Comparison of displacement spectra of the deepest and shallowest events. The shallowest event (solid line) is the 1.8 m event. The deepest event (dashed line) recorded at 17 and 37 m is the 5.6 m event; the deepest event recorded at 73 and 228 m is the 11.5 m event. (a) Displacement spectra for the 17 and 37 m ranges. (b) Displacement spectra for the 73 and 228 m ranges.

Figure 10: Spectral ratio of the deepest to the shallowest events. Dashed lines represent a spectral ratio of one. (a) Spectral ratios for the 17 and 37 m ranges. (b) Spectral ratios for the 73 and 228 m ranges.

Figure 11: Predicted effects of depth on the far-field source potential of Mueller and Murphy (1971). Theoretical source spectra are shown for the 1.8, 5.6, and 11.5 m source depths.

Figure 12: Spectral ratio of the deepest to shallowest Mueller-Murphy sources.

Figure 13: Gradient velocity structure. Compressional and shear velocity and density increase steadily through 25 m (replicated by 13 layers).

Figure 14: Gradient synthetics. Radial and vertical velocity waveforms are shown for the 1.8 and 11.5 m source depths at the 73 and 228 m ranges.

Figure 15: Spectral ratios of gradient spectra with source effects included.

Figure 16: P and Sv-Rayleigh amplitude spectra. P wave amplitude falls off by a factor of 10 from 8 to 40 Hz; Sv-Rayleigh amplitudes fall off by a factor of 10 from 4 to 12 Hz.

Figure 17: Decay of P and Sv-Rayleigh energy with range. Energy decay is plotted for the event at 1.8 m (solid line), 3.2 m (dashed line), 3.9 m (dotted line), 5.6 m (dash-dot line), and 11.5 m (short solid line) (a) Radial component, and (b) vertical component.

Figure 18: P and Sv-Rayleigh energy as a function of source depth. (a) Radial component, and (b) vertical component.

Figure 19: Percentage P and Sv-Rayleigh energy of the total seismic energy.

OBSERVATIONAL DATA

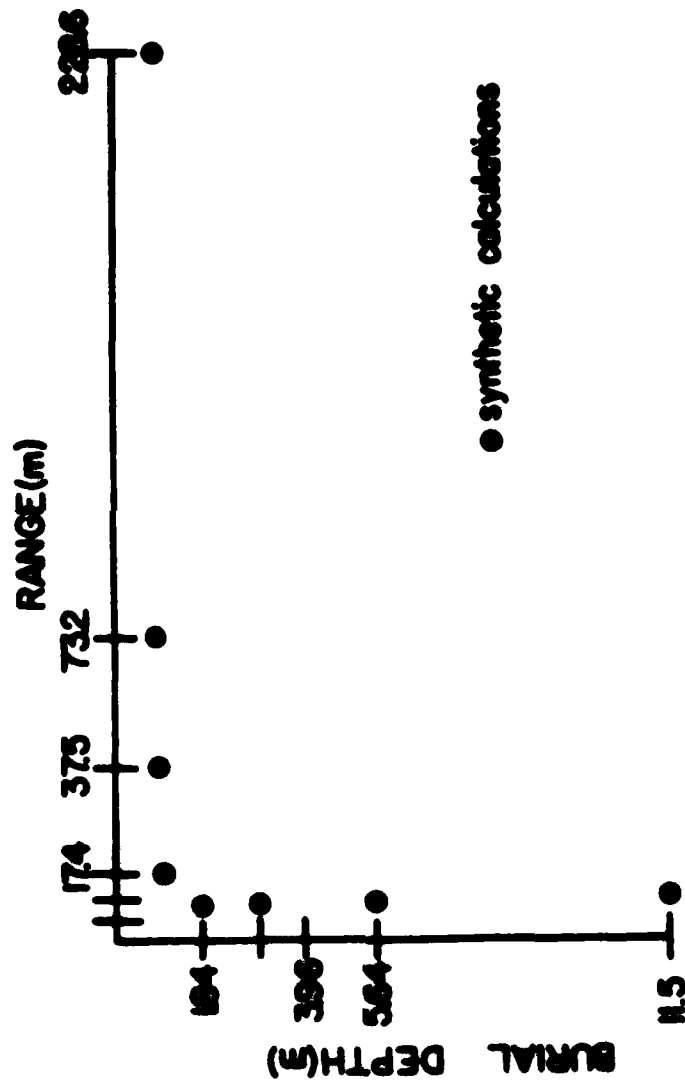


Figure 1

VELOCITY WAVEFORMS Range = 73 meters

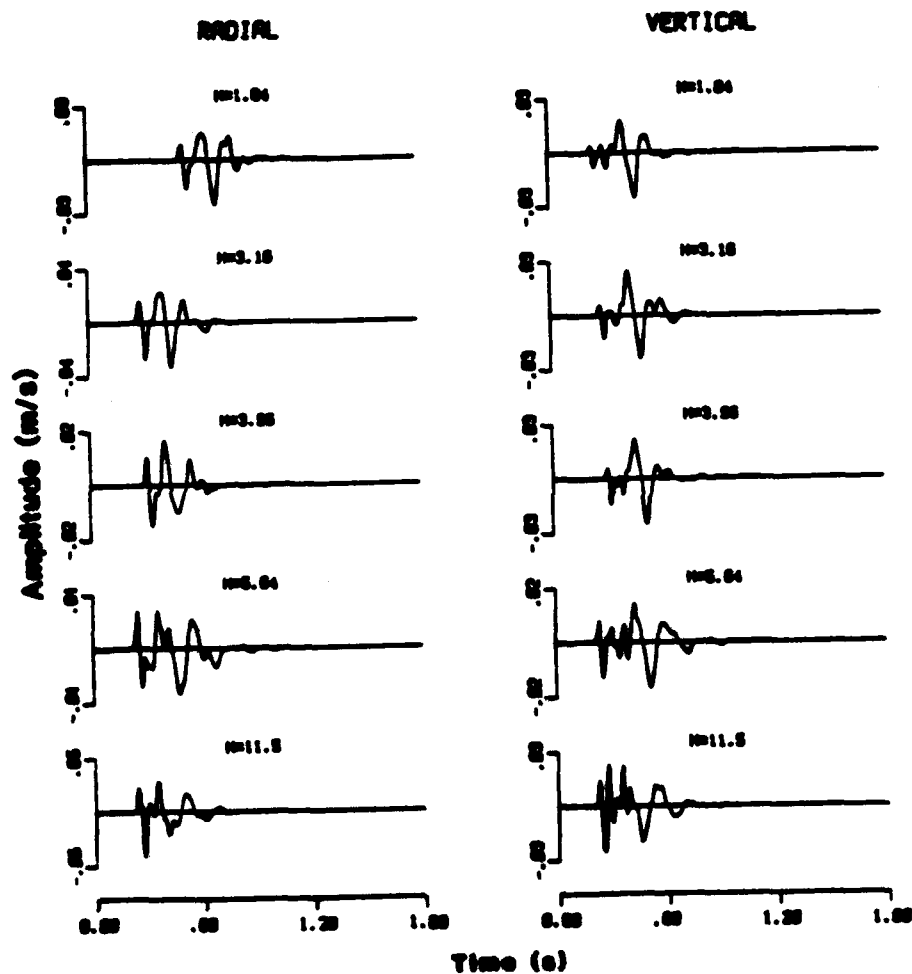


Figure 2
24

RADIAL AND VERTICAL VELOCITY
Range = 228 meters

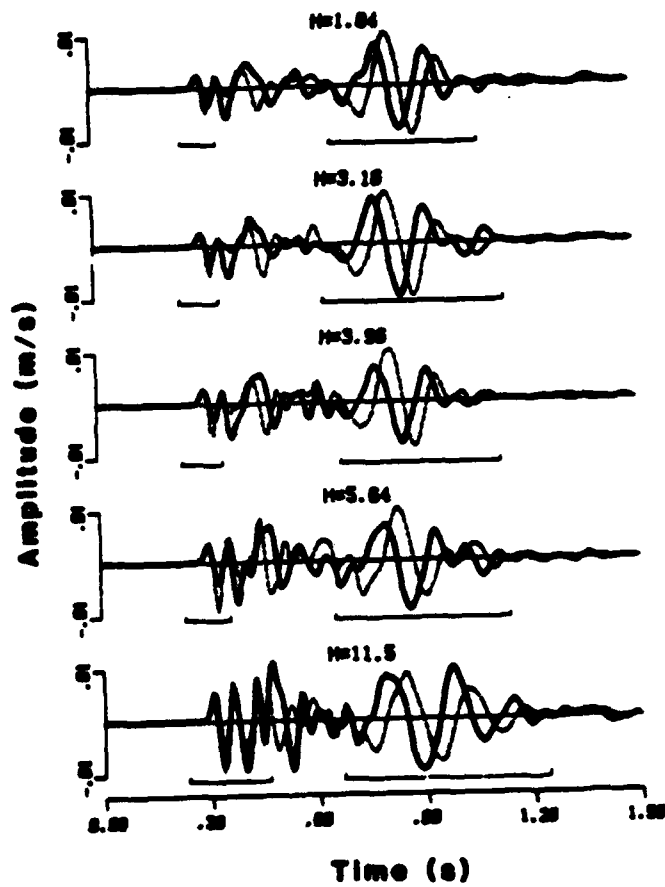


Figure 3a
25

PARTICLE VELOCITY Range 228

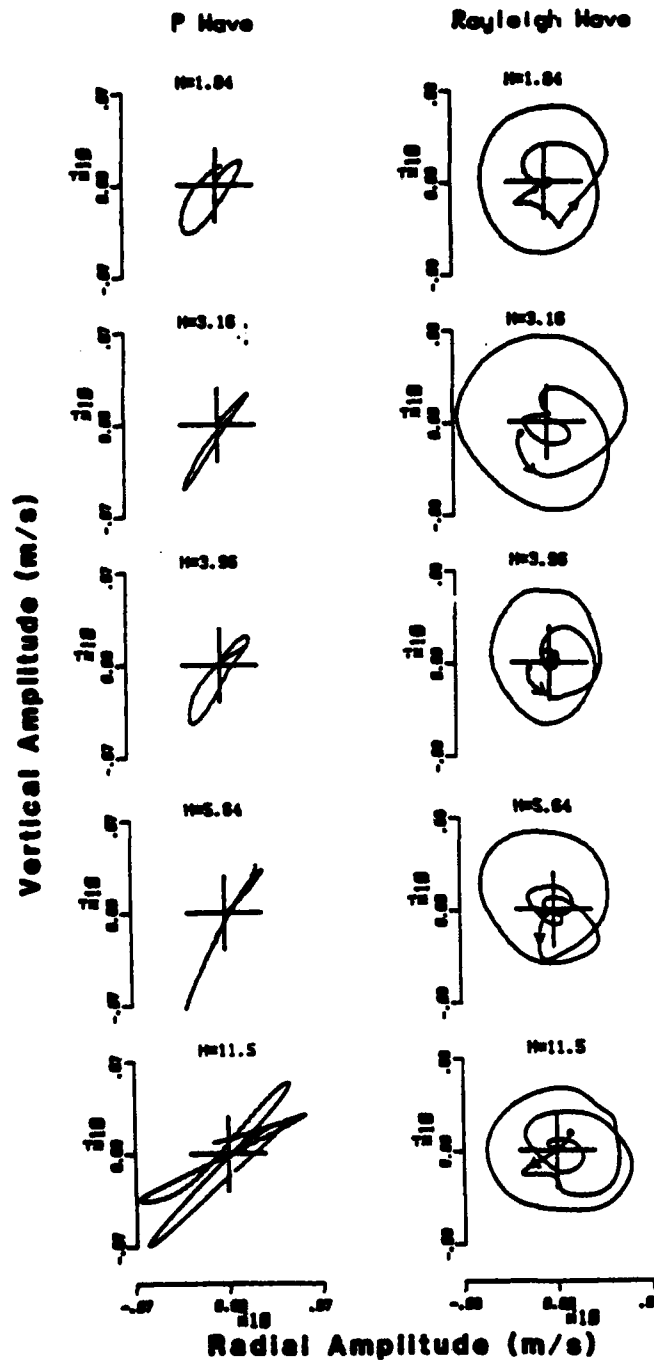


Figure 3b
26

RADIAL AND VERTICAL VELOCITY
Depth = 5.64 meters

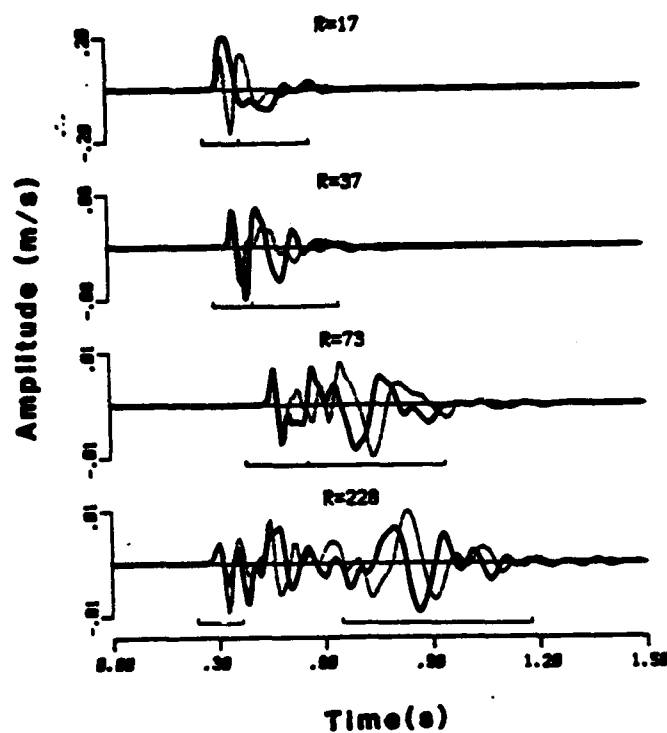


Figure 4a
27

PARTICLE VELOCITY Depth 5.84

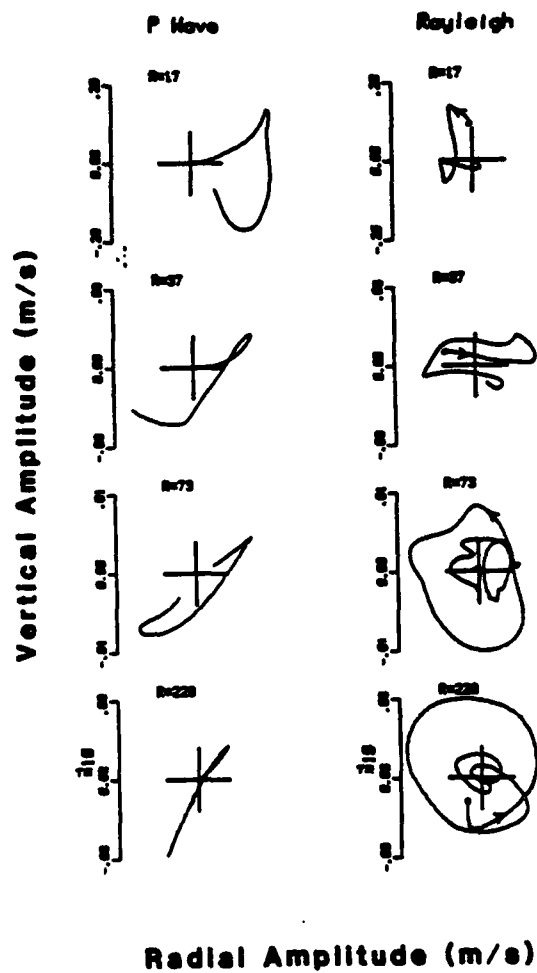


Figure 4b

OBSERVED VELOCITY AMPLITUDES LEAST SQUARES FIT, AMP VS RANGE

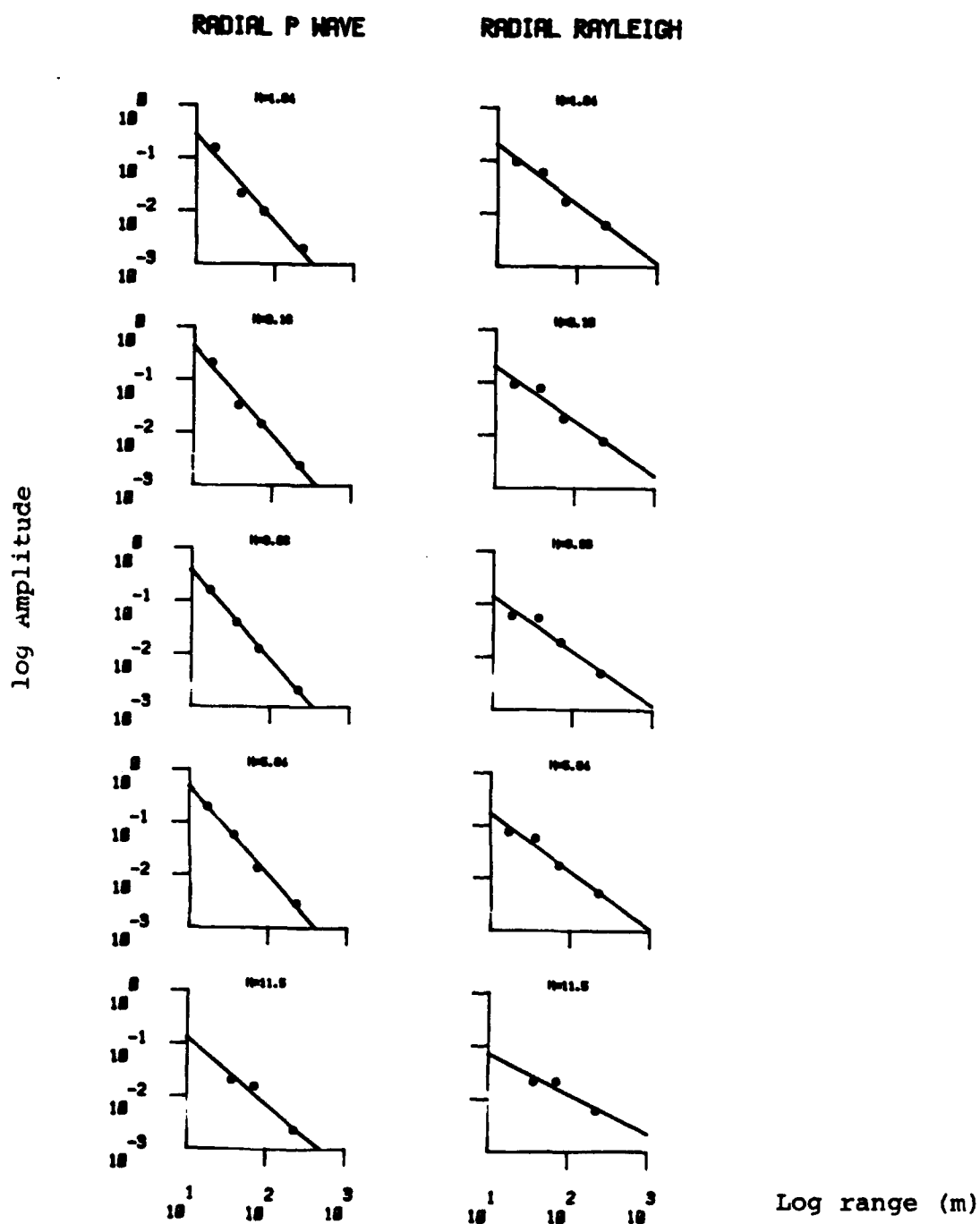


Figure 5a
34

OBSERVED VELOCITY AMPLITUDES LEAST SQUARES FIT, AMP VS RANGE

VERTICAL P WAVE

VERTICAL RAYLEIGH

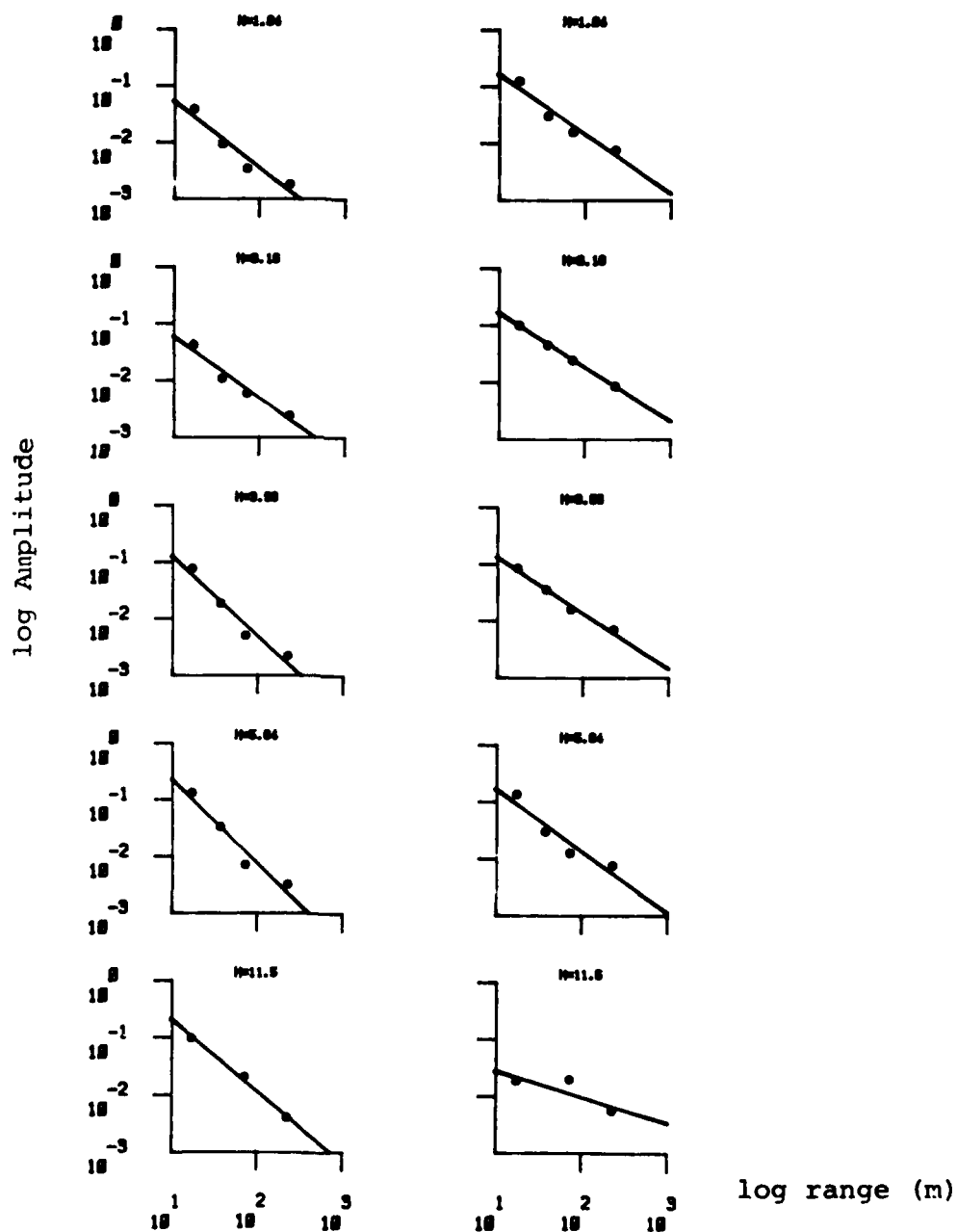


Figure 5b
33

OBSERVED VELOCITY AMPLITUDES P AND RAYLEIGH VS DEPTH

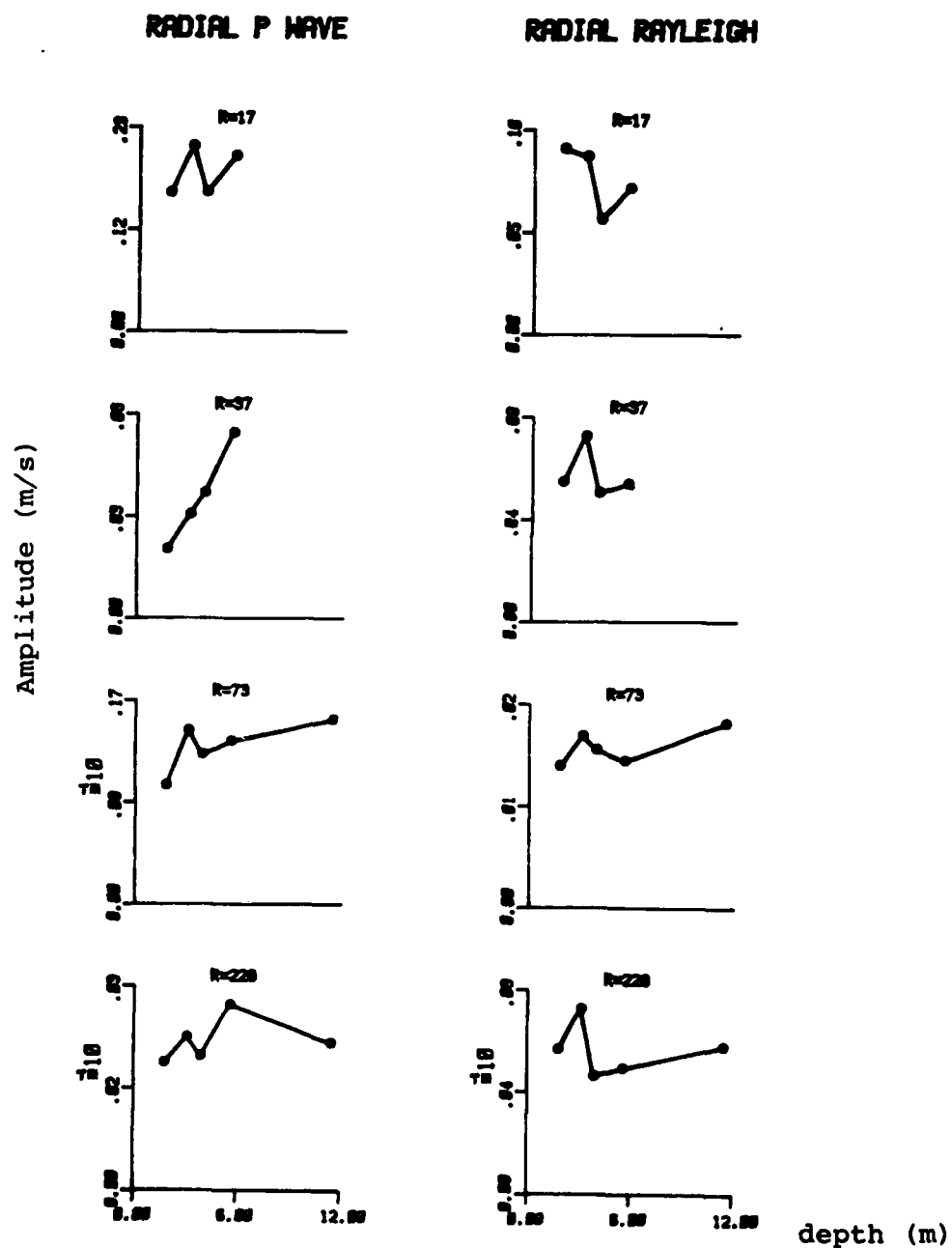


Figure 6a

OBSERVED VELOCITY AMPLITUDES P AND RAYLEIGH VS DEPTH

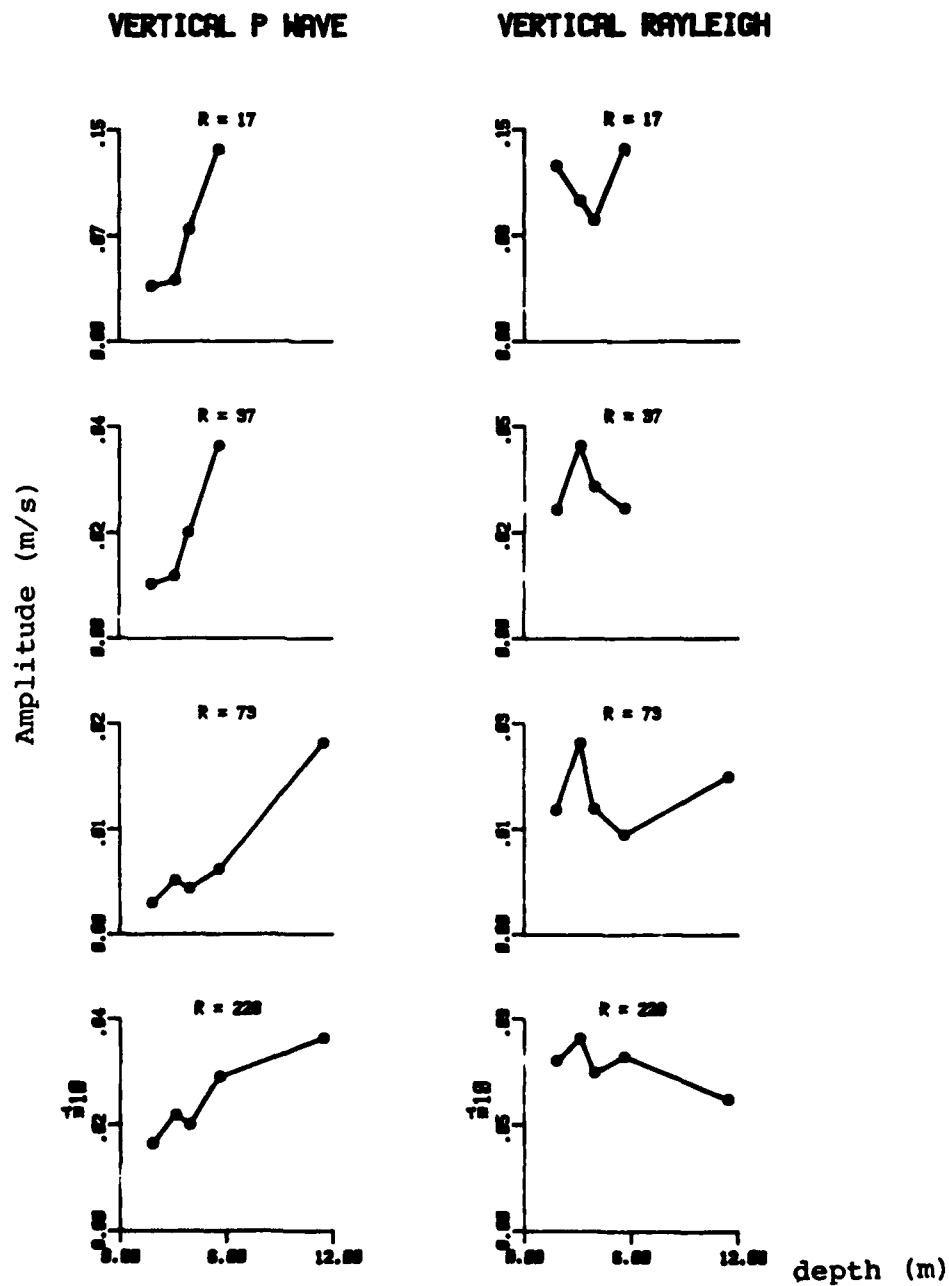


Figure 6b
31

OBSERVED VELOCITY AMPLITUDES P:R RATIO VS DEPTH

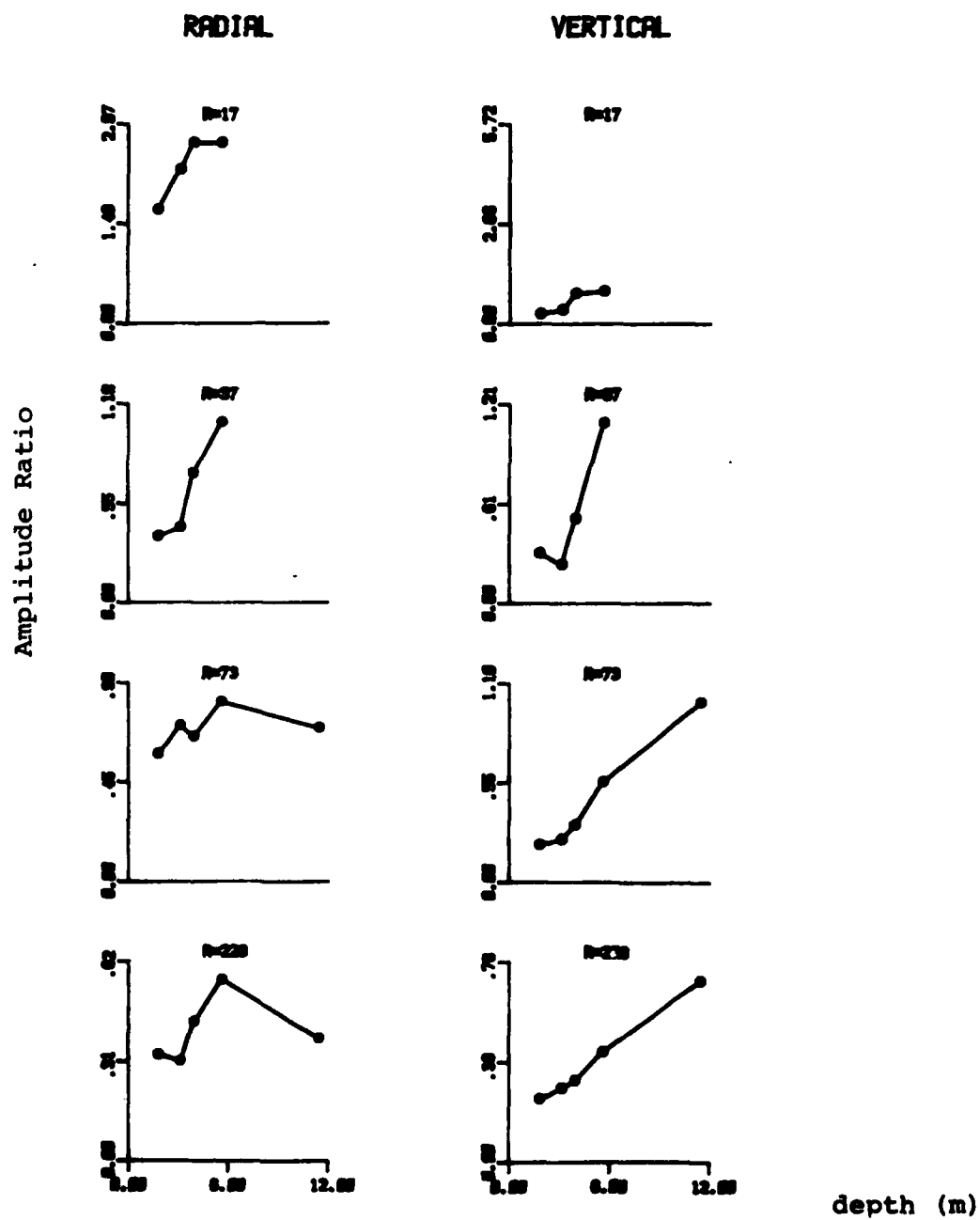


Figure 7
30

FULL WAVEFORM SPECTRA (OBSERVED)

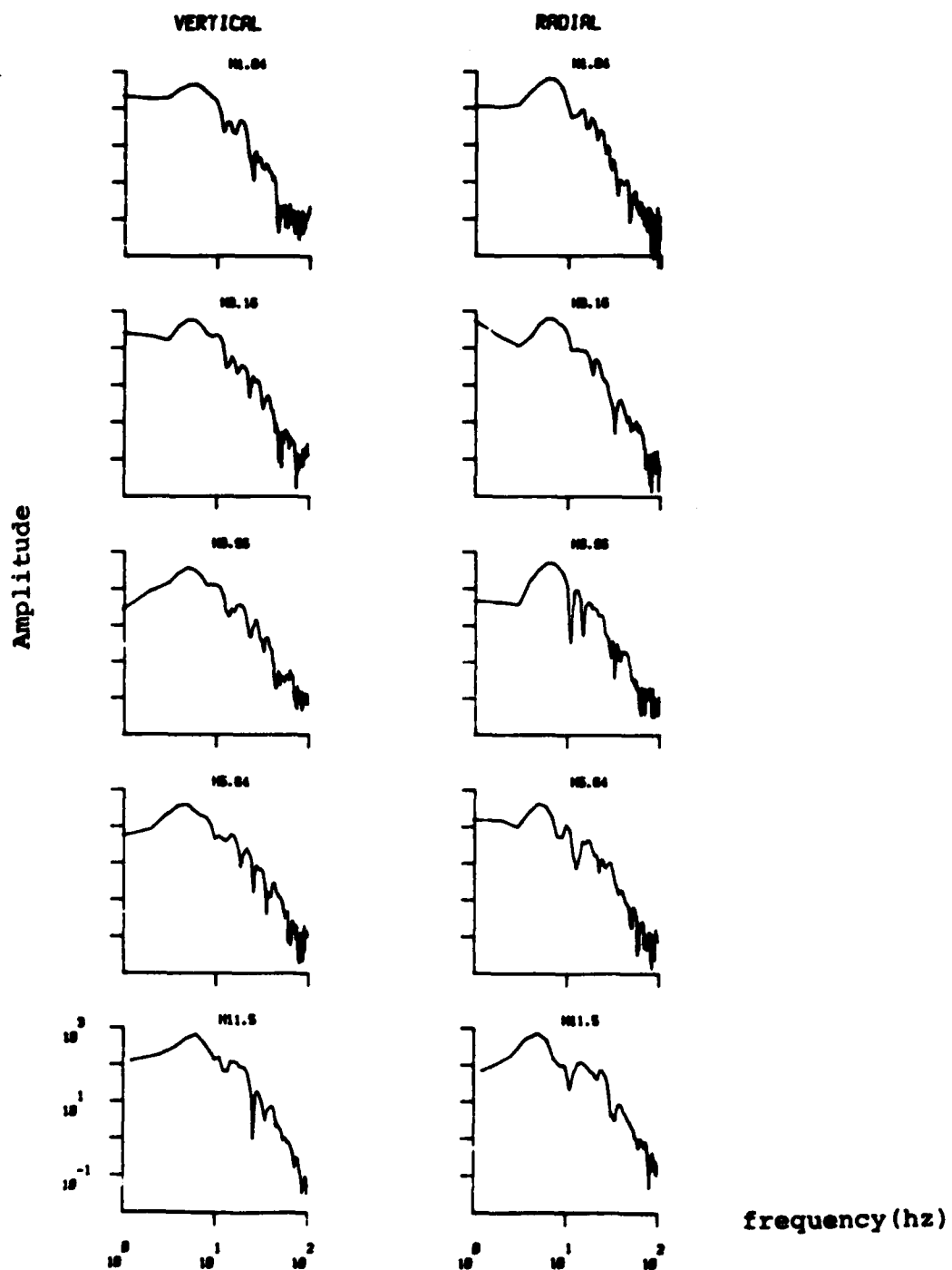
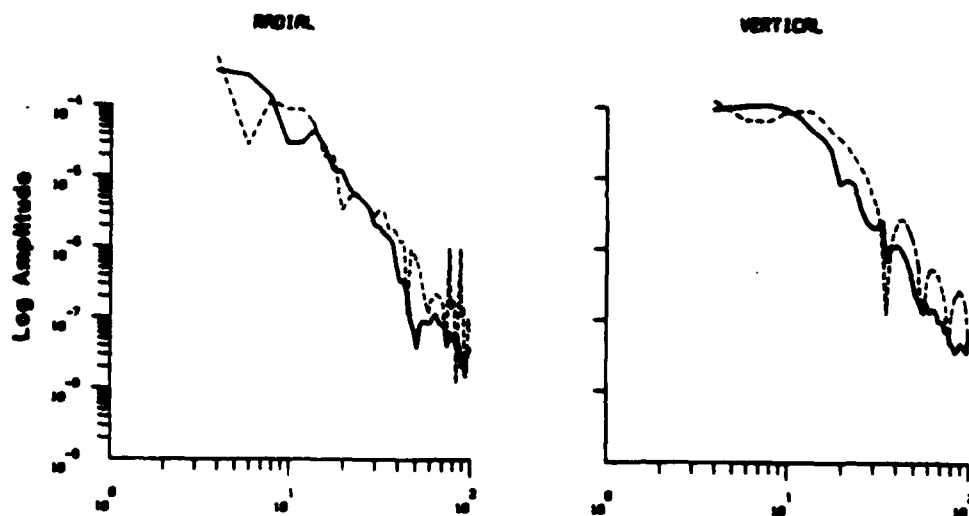


Figure 8
29

DISPLACEMENT SPECTRA

Range = 17 meters



Range = 37 meters

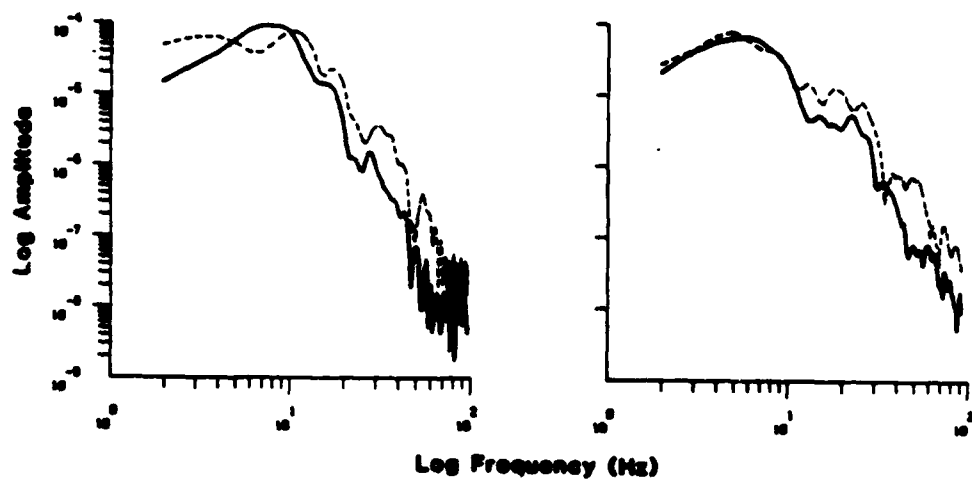
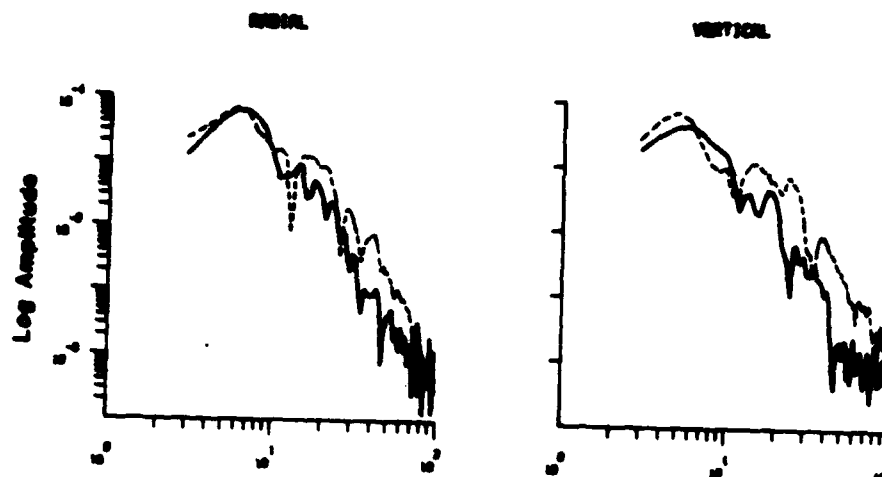


Figure 9a
35

OBSERVED DISPLACEMENT SPECTRA
Range = 73 meters



Range = 228 meters

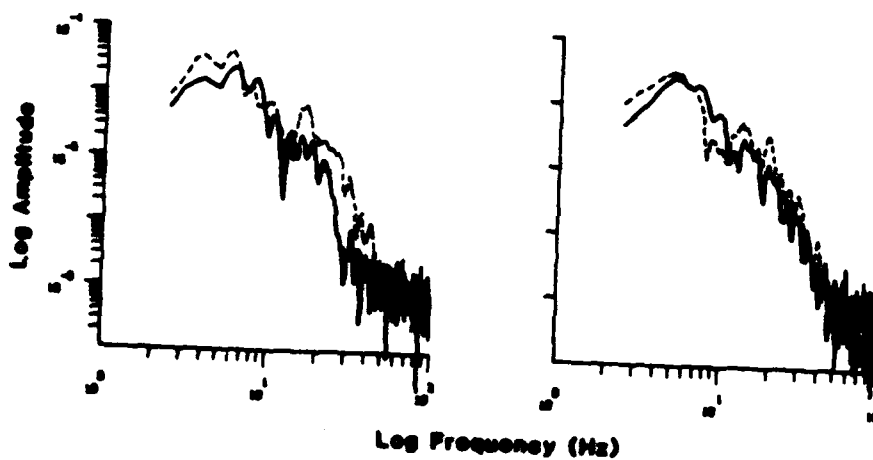
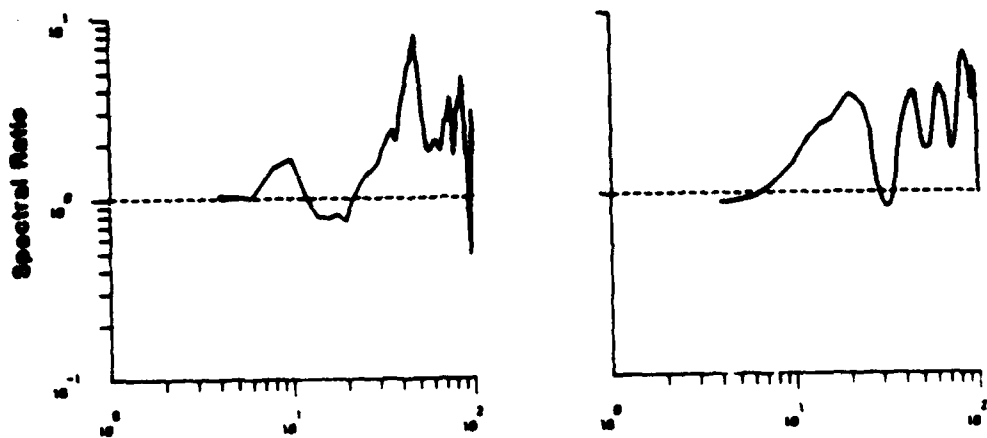


Figure 9b
36

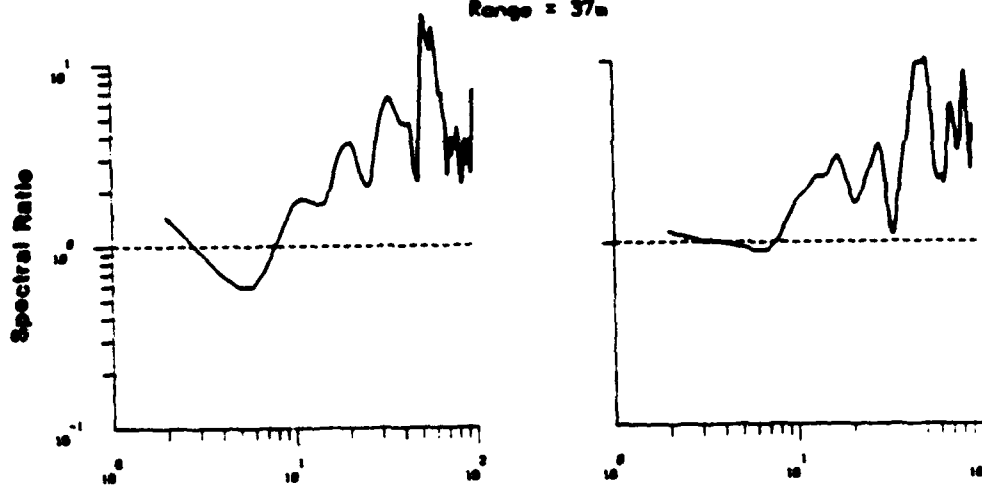
SPECTRAL RATIOS Range = 17m

HORIZONTAL

VERTICAL



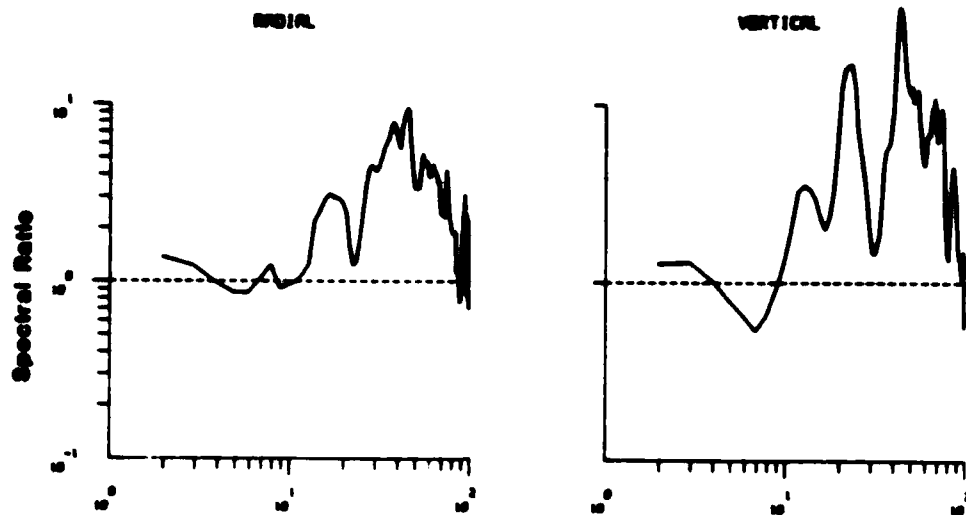
Range = 37m



Log Frequency (Hz)

Figure 10a
37

SPECTRAL RATIOS Range = 73m



Range = 228m

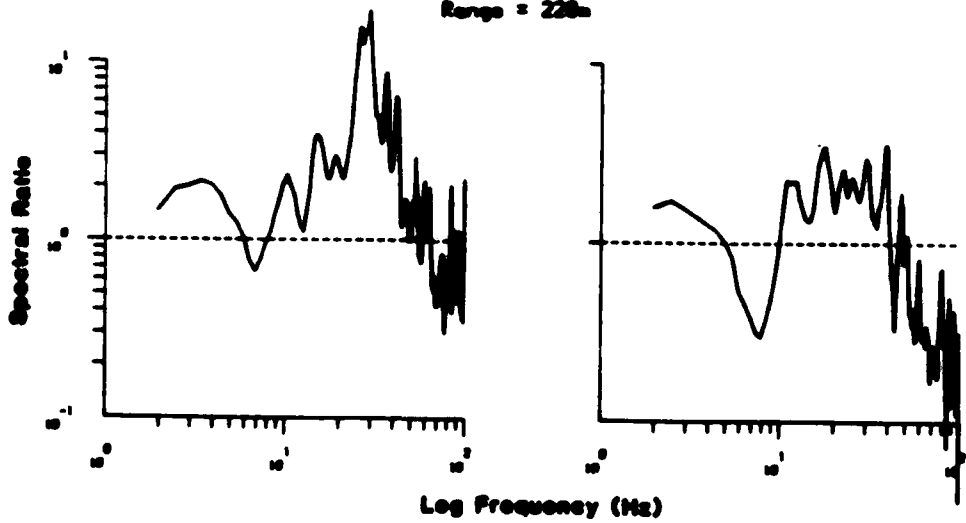


Figure 10b
38

MUELLER-MURPHY SOURCE SPECTRA (DEPTH-SCALED)

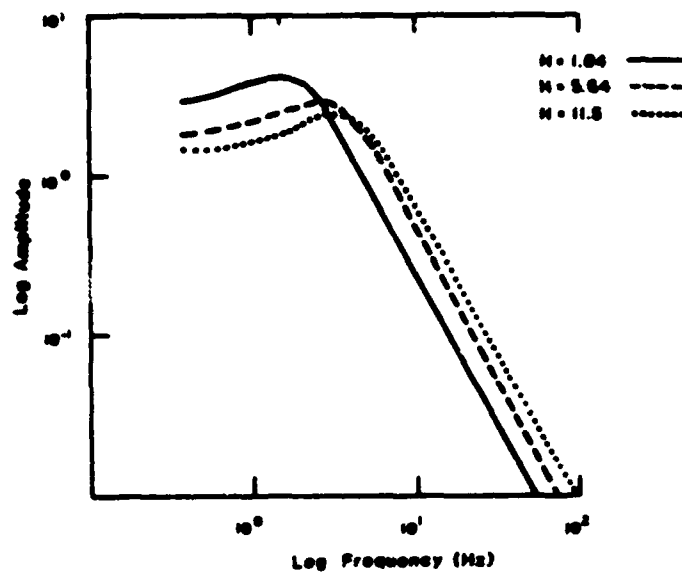


Figure 11
39

MUELLER - MURPHY
SOURCE RATIO

H 11.5 / H 1.84

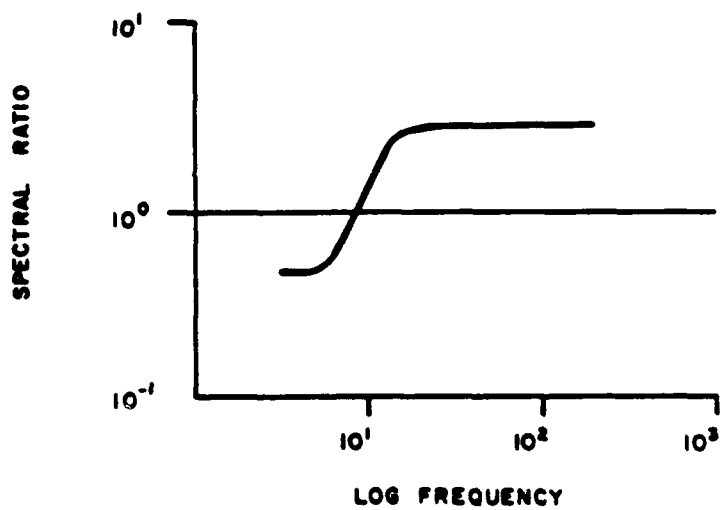


Figure 12

GRADIENT

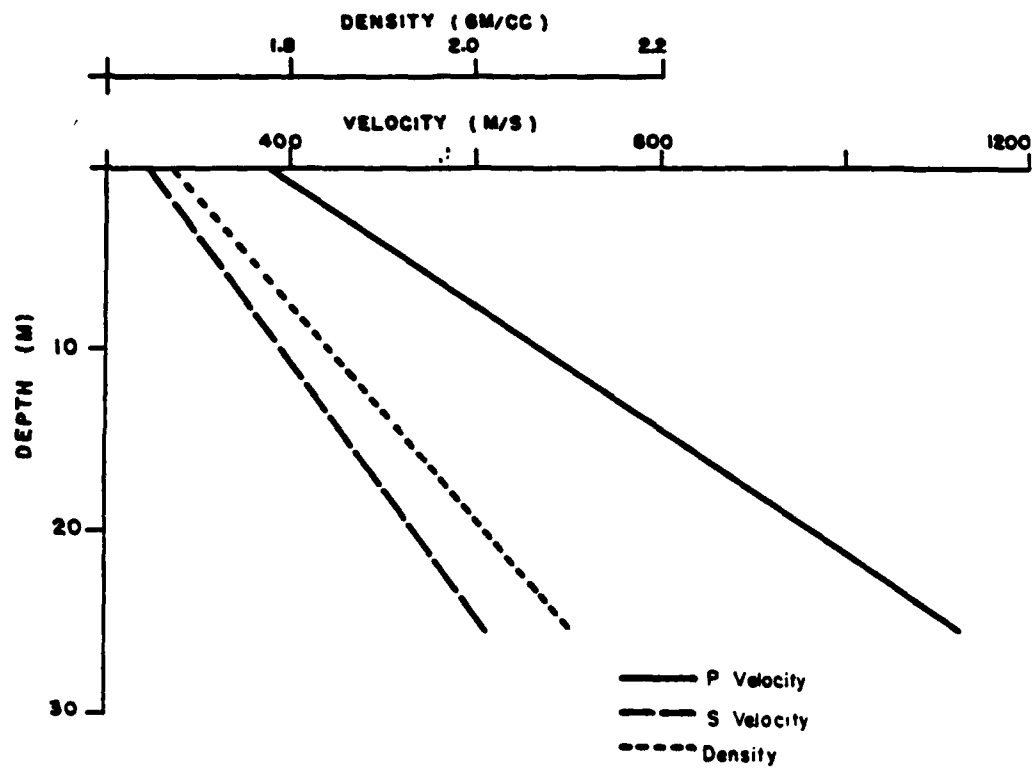
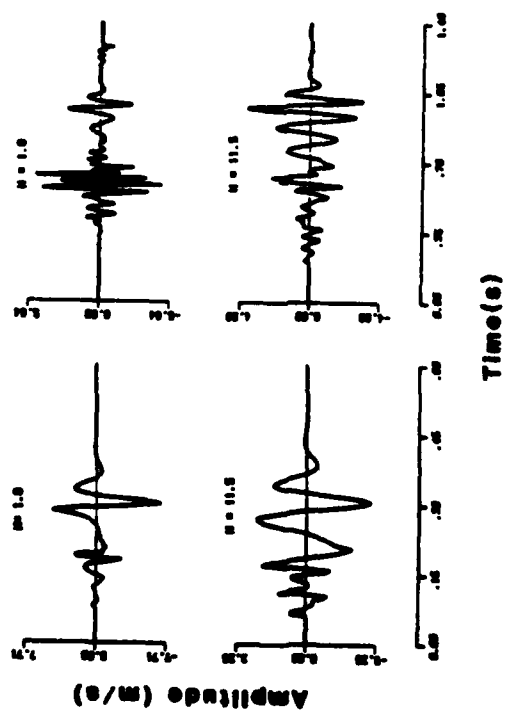


Figure 13

GRADIENT SYNTHETICS Radial Velocity

RANGE = 73m

RANGE = 228m



GRADIENT SYNTHETICS Vertical Velocity

RANGE = 73m

RANGE = 228m

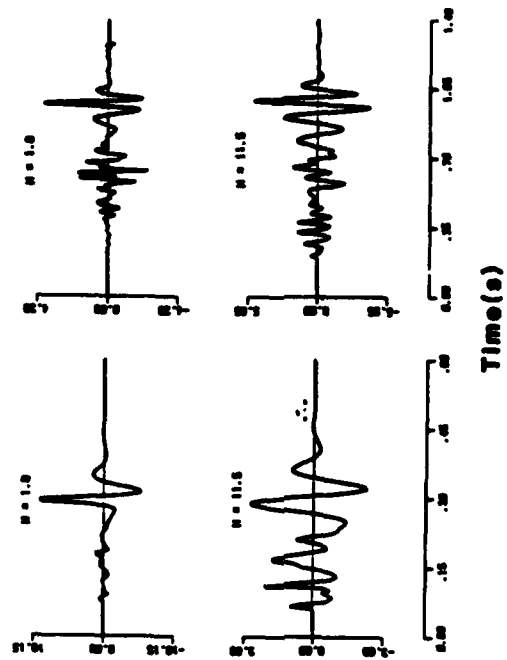
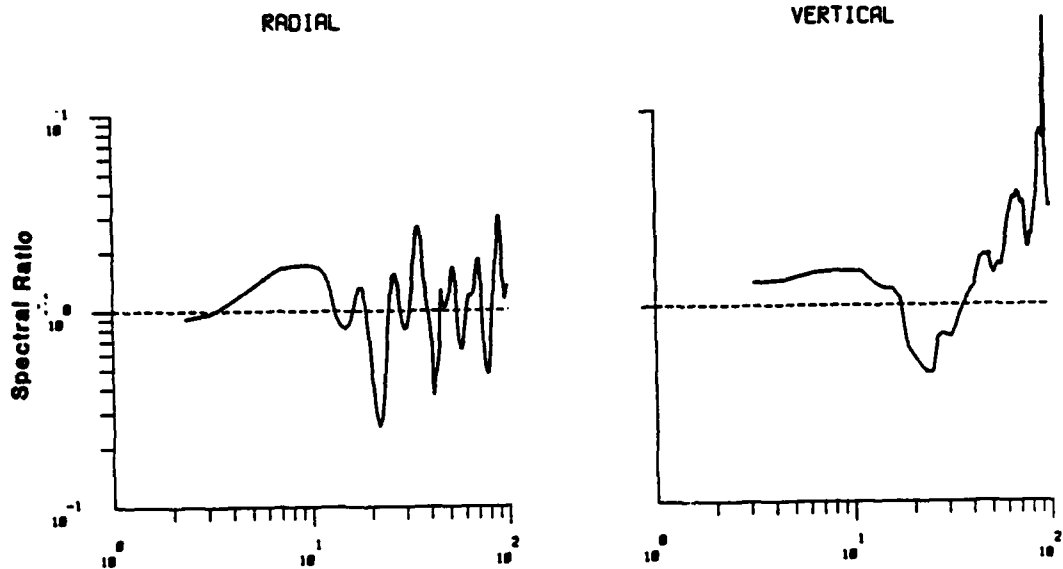


Figure 14

GRADIENT SPECTRAL RATIOS

Range = 73m. H11.5:H11.8



Range = 228m. H11.5:H11.8

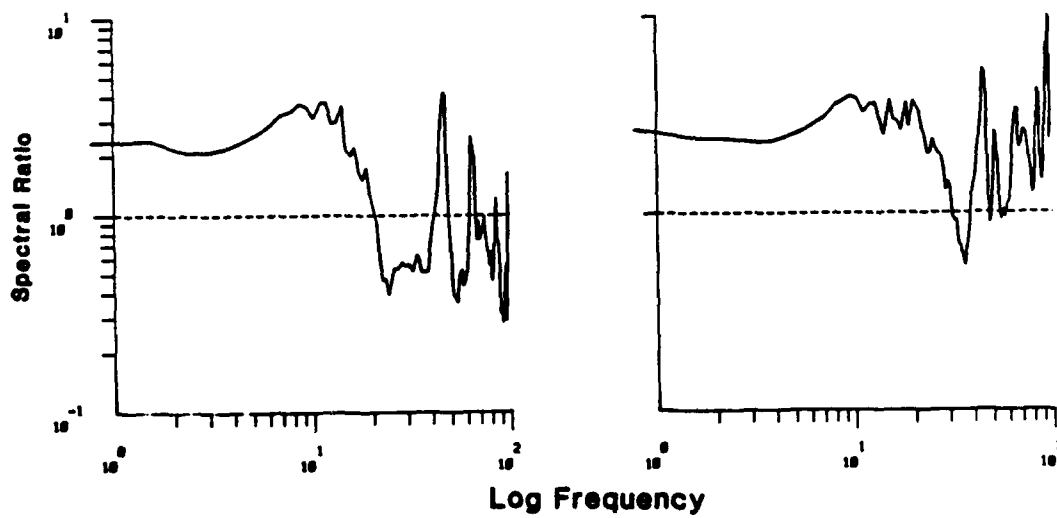


Figure 15

WINDOWED VELOCITY SPECTRA

H=1.84, R=228

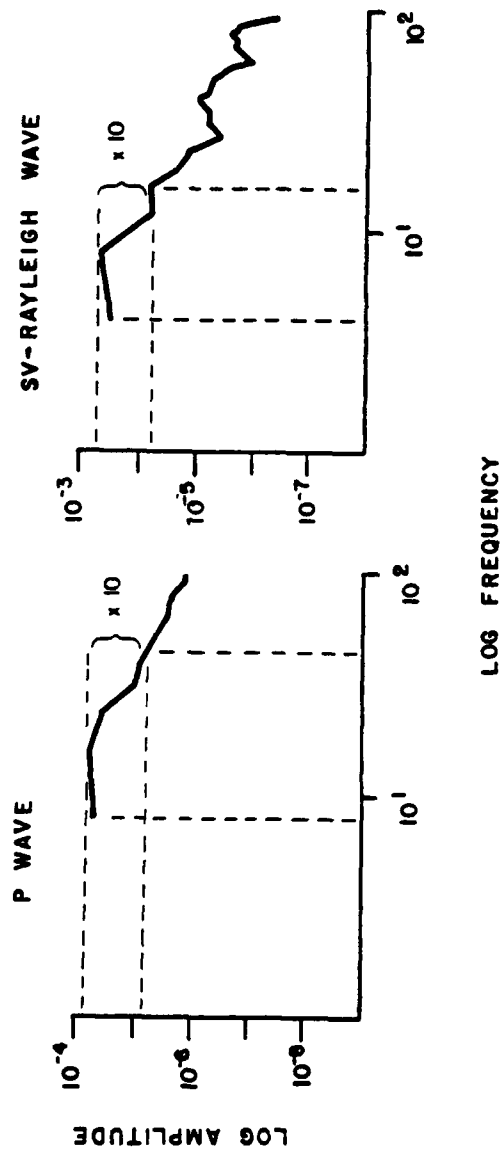


Figure 16

ENERGY vs RANGE

RADIAL

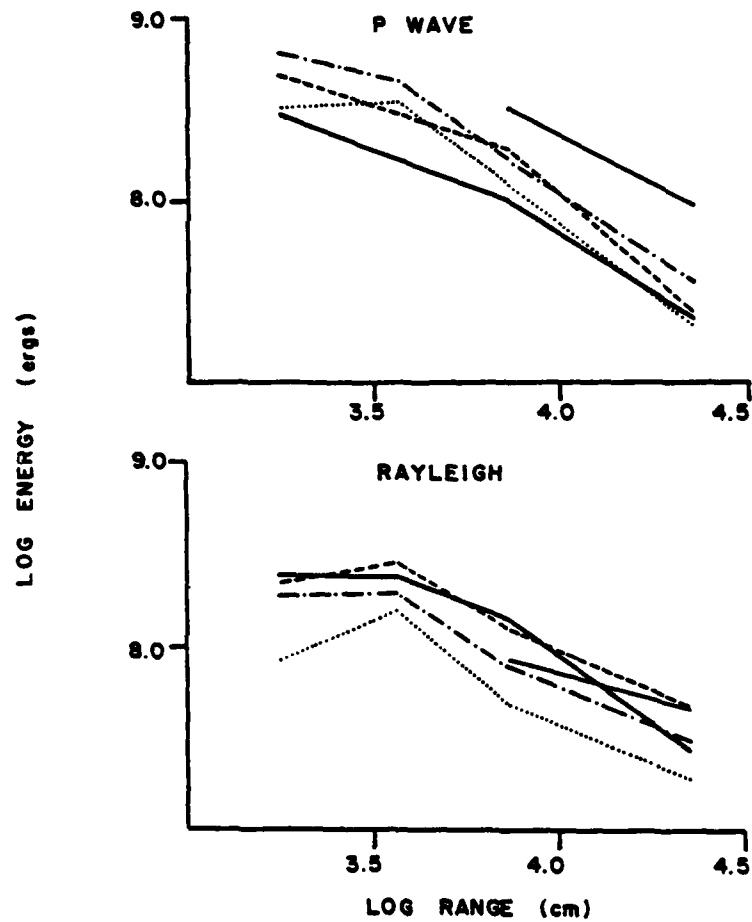


Figure 17a

ENERGY vs RANGE

VERTICAL

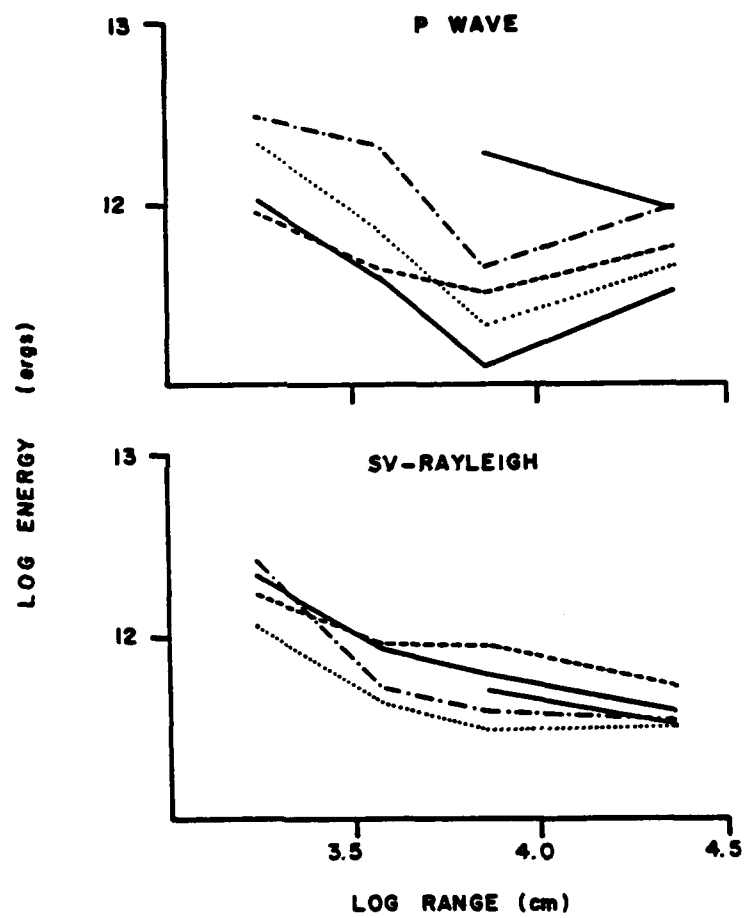
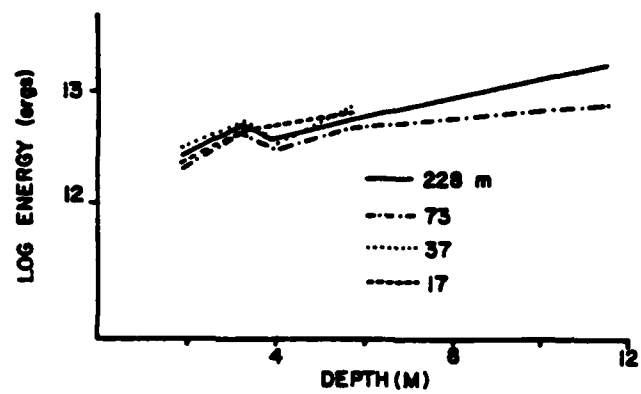


Figure 17b

ENERGY VS DEPTH

RADIAL P WAVE



RADIAL RAYLEIGH

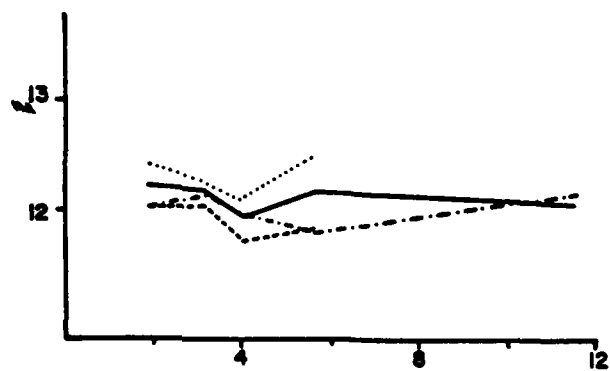


Figure 18a

ENERGY vs DEPTH

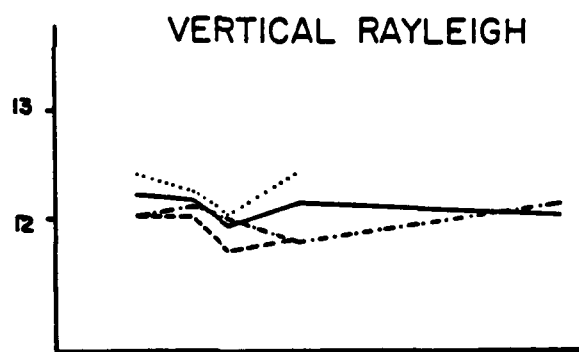
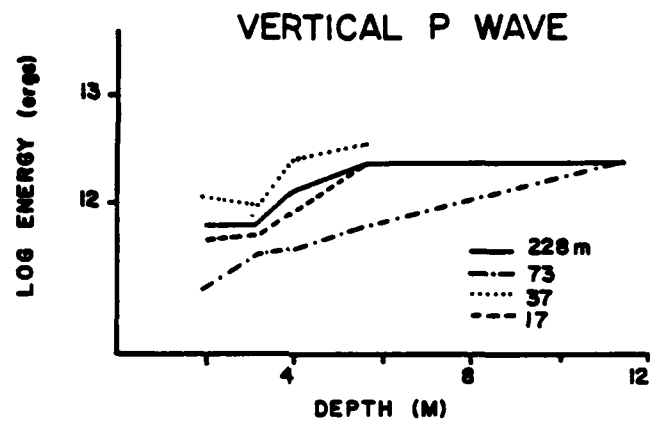
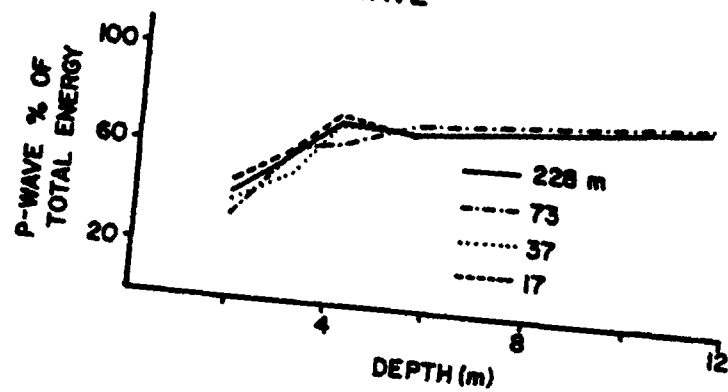


Figure 18b

ENERGY % VS DEPTH

P-WAVE



RAYLEIGH WAVE

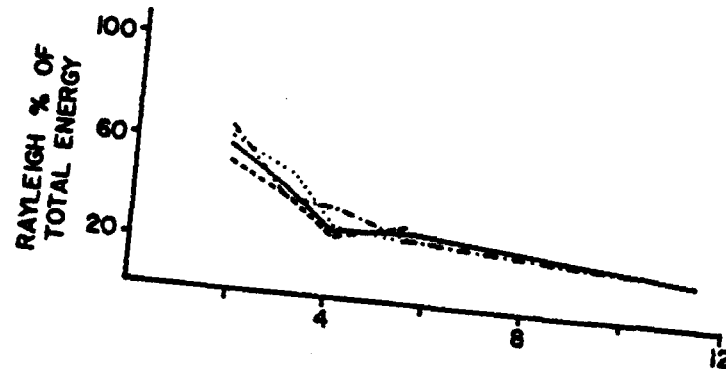


Figure 19

**CORNER FREQUENCIES OF
OBSERVED DISPLACEMENT SPECTRA**

RADIAL					
source depth:	1.84	3.16	3.96	5.64	11.5
range:					
17	10.0	10.5	11.0	10.5	--
37	10.0	11.0	12.0	15.0	--
73	10.0	10.5	10.5	11.5	12.5
228	10.0	10.0	10.5	10.5	11.5

VERTICAL					
source depth:	1.84	3.16	3.96	5.64	11.5
range:					
17	12.0	12.0	15.0	15.0	--
37	11.0	11.0	14.0	15.0	--
73	10.0	10.5	11.0	12.0	12.5
228	9.0	9.5	10.5	10.5	11.5

Table 1a

DC LEVELS OF
OBSERVED DISPLACEMENT SPECTRA
(x10**4)

RADIAL					
source depth:	1.84	3.16	3.96	5.64	11.5
range:					
17	3.20	3.20	3.00	6.00	--
37	1.00	1.00	0.70	0.80	--
73	0.70	0.70	0.50	0.40	1.20
228	0.22	0.40	0.28	0.31	0.40

VERTICAL					
source depth:	1.84	3.16	3.96	5.64	11.5
range:					
17	1.10	0.90	0.80	1.20	--
37	0.70	0.75	0.55	0.90	--
73	0.48	0.60	0.40	0.42	0.72
228	0.28	0.37	0.30	0.38	0.40

Table 1b

APPARENT SPATIAL ATTENUATION
 (*10**5)
 Least square energy decay rates
 and Linear Correlation Coefficients

Depth (m)	Radial	LCC	Vertical	LCC
----- P ENERGY -----				
1.84	-5.0	0.98	--	--
3.16	-6.1	0.99	-1.2	0.31
3.96	-5.9	0.98	-2.0	0.48
5.64	-5.8	0.99	-1.2	0.34
Average:	-5.7	--	-1.5*	--
----- RAYLEIGH ENERGY -----				
1.84	-4.7	0.99	-2.7	0.82
3.16	-3.5	0.95	-1.9	0.87
3.96	-3.7	0.92	-1.8	0.74
5.64	-3.8	0.96	-2.6	0.61
Average:	-3.9	--	-2.3	--

* Decay rates are slow for the vertical P wave and correlation coefficients are poor, largely because P wave energy at the 73 meter range is anomalously low.

Table 2

Q VALUES FOR P AND SV-RAYLEIGH WAVES

$$Q = f/ca$$

Frequency	Q	
8	5	Radial P Wave
40	25	a = 5.7×10^{-5} ergs/cm c = 920 m/sec
4	10	Radial SV-Rayleigh Wave
12	30	a = 3.9×10^{-5} c = 320 m/sec
8	16	Vertical P Wave
40	90	a = 1.5×10^{-5} c = 920 m/sec
4	18	Vertical SV-Rayleigh Wave
12	54	a = 2.3×10^{-5} c = 320 m/sec

Table 3

TOTAL SEISMIC ENERGY
x 10**13

Total Radiated Energy = 10**15 ergs

Range(m)	17	37	73	228
Depth(m):				
1.8	1.03	0.79	0.67	0.86
3.2	1.20	1.10	0.91	1.08
3.9	0.93	0.94	0.58	0.80
5.6	1.70	1.30	0.80	1.30
11.5	--	--	1.40	2.90

Table 4

**STOCHASTIC GEOLOGIC EFFECTS
ON NEAR-FIELD GROUND MOTIONS IN ALLUVIUM**

**R.E. Reinke
AFWL/NTESG
Kirtland AFB, NM 87117-6008**

**B.W. Stump
Department of Geological Sciences
Southern Methodist University
Dallas, Texas 75275**

ABSTRACT

Analysis of accelerograms recorded at the 20 m range from a buried 5 pound detonation in alluvium revealed wide (as large as 20 dB in the amplitude modulus of the Fourier transform) variations in response for frequencies above 35 Hz. Additional experiments were performed which ruled out source asymmetry or instrumental irregularity as the cause of these variations. The observations suggest that scattering by geologic inhomogeneity is responsible for the frequency dependent spatial variability in ground motion. A thorough understanding of the physical processes responsible for this variability requires that a quantitative relationship be established between the subsurface material property information and the observed ground motion characteristics. An attempt was made to do this using available standard penetration test (SPT) data from the test bed where the initial experiment was detonated. Autocorrelations of the blow count data from the SPT test were computed and compared with theoretical exponential and Gaussian distributions. The exponential distribution with a scale length between 2.0 and 3.0 m best matches the data. Assuming the Born approximation, a scale length of 2.0 - 3.0 m implies that significant scattering should occur above 10 Hz. The recorded ground motions are, however, coherent out to about 35 Hz, suggesting a scale length 0.5-1.0 m which is beyond the resolution of the SPT technique. This scale length is, however, not unreasonable in light of the general geologic characteristics of the test area.

INTRODUCTION

Several recent studies have found a surprising lack of coherence between ground motion waveforms recorded at stations separated by only a few tens of meters. McLaughlin, et. al. (1983), discuss the station-to-station waveform coherence for near-field explosion accelerograms recorded on a nine-station array at Pahute Mesa, Nevada Test Site. For this array, at a range of 6 kilometers from a 5.6 ML underground explosion with an interstation spacing of 100 meters, strong incoherent signals were found above 5 Hz. on all components. This incoherence was attributed to scattering. Vernon, et. al. (1985), discuss earthquake seismogram coherence for a nine-station array with an interstation spacing of 50 m. This temporary array was located near the Pinon Flat observatory in California. Several events with magnitudes between 3.0 and 4.2 and hypocentral distances ranging from 10 to 50 kilometers were analyzed. For this data set, P waves were found to be coherent up to the 25-30 Hz. region, S waves up to about 15 Hz. This variability in ground motion over such short distances raises questions about the appropriateness of using single station point measurements of the ground motion field for the inversion of source functions as well as the use of the peak ground acceleration (PGA) statistic based on single point measurements.

Smith, et. al. (1982), analyzed the near-field motions from the 1979 Imperial Valley Earthquake. This data set was obtained from a closely spaced array of 5 stations. This study confirmed that incoherence of higher frequency ground motions could, because of averaging effects, reduce the high frequency input to buildings with foundations of large areal extent. Analysis of this particular data set suggested that base averaging reduction

factors of 10 to 30 percent would have occurred for foundations 50 m in diameter for frequencies above 20 Hz. No significant reduction would have occurred for frequencies below 5 Hz.

This frequency dependent spatial variability in ground motion has also been observed on some small-scale, high-explosive tests conducted in dry alluvium. An array of six triaxial accelerometers spaced at six azimuths at the 20 m range from a buried 5-pound detonation yielded waveforms which were incoherent above 30-35 Hz. In an effort to determine whether these variations were induced by instrumentation, source asymmetry or scattering due to geologic variability, a series of small-scale, high-explosive experiments were performed. This paper describes the results of these experiments and the physical interpretation of the data.

THE INITIAL EXPERIMENT--THE ART 2 TEST

The Array Test Series (ARTS) was a series of single and multiple 5-pound explosive tests conducted in dry alluvium. The ARTS was formulated, designed and implemented to investigate the quantitative effects of finite explosive sources upon observed motion fields. The single burst tests in the series were intended to thoroughly characterize the single burst ground motion environment (Stump and Reinke, 1987). One of these tests, ART 2 (Table 1), was intended to determine the degree of azimuthal variation in ground motion levels resulting from a single charge event. The experimental layout for this test is shown in Figure 1. Six triaxial servo accelerometers were placed at the 20 m range at six different azimuths. These accelerometers were recorded by 3-channel digital event recorders at a rate of 200 samples/second with a 5-pole low pass Butterworth filter at 70 Hz. The original accelerograms, along with low pass (30 Hz corner) and high pass (40 Hz corner) filtered versions, are shown in Figures 2 and 3. Fourier acceleration spectra for the waveforms are shown in Figure 4. Examination of the acceleration traces and the spectra in these figures reveals considerable similarity in the various waveforms below 30 Hz, while large azimuthal amplitude variations are observed for frequencies above 30-35 Hz. The accelerograms show that the high frequency energy arrives after the initial coherent low frequency response with a great variability in wave shape as well as amplitude. The vertical and radial spectral shapes (Figure 4) are similar between 5 and 35 Hz, while variations up to 15-20 dB occur above 35 Hz.

EXPERIMENTAL DESIGN

Three possible sources for the observed azimuthal variations in waveforms have been identified: (1) non-uniformity in instrumentation response, (2) asymmetry in the explosive source, and (3) geologic inhomogeneity. In order to experimentally investigate the first possibility--instrumental irregularity--the ART 19 test (Table 1), also called the "huddle" test was performed. In this test, all seven 3-component accelerometers were placed in a closely spaced group at the 20 m range (Figure 5) from a 5-pound charge detonated at a depth of 1 meter. Individual vertical and radial spectra from this test are compared in Figure 6. The resulting spectral scatter, as observed in these figures, is at most 3-4 dB, over the band from 5-70 Hz, much less than that observed for the azimuthal data. In fact, the higher frequency scatter (40-70 Hz region) shown in these figures may not reflect true instrumental irregularity, since, as seen by examination of Figures 5 and 6, the accelerometers which are physically closest in the field do possess the greatest degree of similarity in spectral shape.

An additional set of experiments, the ART 11 series (Table 1), was designed to determine whether azimuthal irregularities in ground motion result primarily from propagation path variations and scattering by geologic inhomogeneity or explosive source asymmetry. The test bed layout for the ART 11 tests is shown in Figure 7. Ground motions were recorded by triaxial servo-accelerometers and 3-channel digital event recorders at six equally spaced azimuths at a range of 20 meters. The ART 11 series of tests consisted of five separate 5-pound detonations--all fired at the same test-bed with the accelerometers remaining

in the same position from shot to shot. The initial detonation was fired at a depth of 1 m in situ. The resulting crater was then excavated and a new 5-pound charge emplaced in the resulting pit with uniform sand rained around the charge. This process was repeated a total of four times. Thus the ART II series of tests consisted of five shots, one in situ and four pit shots--all using the same test-bed and an identical recording array.

The goal of the ART II tests was to determine whether source asymmetry or geologic factors were the dominant cause of the observed scatter. By repeating the experiment five times at the same location, five sets of triaxial accelerograms and spectra were obtained for each azimuth. If the observed data scatter were produced by geologic inhomogeneity, then one would expect very similar acceleration waveforms, as well as amplitude spectra, to be observed from shot to shot at the same recording station. The detonation of a 5-pound charge is, of course, not strictly a repeatable phenomenon, since the initial in situ detonation destroys a portion of the test-bed by formation of the crater. Excavation of the severely disturbed material comprising the crater and subsequent emplacement of the charge within the pit was intended to make the experiment as repeatable as possible. The transition from the in situ test to the pit sequence was the most severe. The in situ shot produced a crater roughly 2.2 meters in diameter. The crater was excavated producing a pit about 3 m in diameter and 1.3 m deep. The dimensions of both crater and pit increased slightly with each shot. The final pit was about 3.5 m in diameter and the final crater about the same diameter.

While the ART 2 and the ART Phase II (the pit shots)

experiments investigated azimuthal ground motion variations at the 20 meter range, the ART III-1 experiment (Table 1) was designed to investigate the influence of range upon the observed azimuthal variations. If scattering by geologic inhomogeneity is the dominant factor producing the azimuthal variation, then one might expect the degree of variation to increase with range of the receiver array. The ART III-1 test consisted of a 5-pound cylindrical charge detonated in situ at a depth of 1 meter. The ground motions were recorded at a total of 12 locations using triaxial servo accelerometers and 3-channel digital event recorders. Six recording stations were placed at equal azimuths at the 10-m range, and the remaining six were placed at equal azimuths at the 30-m range.

STOCHASTIC/DETERMINISTIC CLASSIFICATION TOOLS
AND DATA ANALYSIS

One approach to quantify the observed variation in the data sets is to compute the coherency between station pairs in a manner analogous to that employed by McLaughlin, et al. (1983). The coherency is defined by:

$$\gamma_{xy} = \frac{|\phi_{xy}(\omega)|}{(\hat{\phi}_{xx}(\omega) \cdot \phi_{yy}(\omega))^{1/2}}$$

where $\phi_{xy}(\omega)$ = cross power spectrum and $\phi_{xx}(\omega)$, $\phi_{yy}(\omega)$ the power spectra of the two time series.

As is well known, smoothing must be applied to the spectra prior to estimation of the coherency in order to minimize variances at each frequency. For the coherency estimates computed here, a 4-point lag window was applied to the spectra prior to estimation of the coherency factors.

Coherencies were computed between the 0° data and each of the other recording stations. The time windows used were 128 samples, or 0.64 seconds in length. This length window encompasses all of the wavetrain. At this relatively short range, it is effectively impossible to separate the various components of the waveform.

The computed coherencies for the station pairs are shown in Figure 8. The coherence factors for the vertical and radial components are higher than might be intuitively expected after examination of the spectral plots in Figure 4. However as Smith, et al. (1982), point out, the coherency will be unity when the signals at two stations are related by any linear transfer function so the coherence function is not a direct estimator of

the variation of amplitude across an array.

Based upon the results of the coherency analysis an alternate approach for analysis of the data was taken. The set of amplitude spectra of the azimuthal observations was treated as a statistical ensemble. An example of this technique applied to the ART 2 data is shown in Figure 9. The mean and variance of the spectral ensemble were calculated as shown assuming a log-normal distribution. These figures illustrate $\bar{\mu}$, the mean and $\bar{\mu} \pm \sigma$, the mean ± 1 standard deviation for the vertical, radial, and transverse data from ART 2. The vertical and radial data show small standard deviations between 5 and 30 Hz. Beyond 35 Hz, the width of the $\bar{\mu} \pm \sigma$ deviation band increases until at 40 Hz, the expected scatter in the Fourier modulus is 8 dB or greater. The transverse motions, on the other hand, show at least 8 dB scatter throughout the entire frequency band; although the overall mean amplitude is reduced about 10 dB from the radial and vertical amplitude levels.

The lack of coherence below 5 Hz on all components has several possible sources. This effect was first thought to be due to signal induced tilts in the accelerometers. Integration of the acceleration traces and subsequent attempts to correct the resulting velocity and displacement records did not significantly change the estimates. It is likely that aliasing and/or noise is the cause of this low frequency incoherence. The amplitude level in this region is very low relative to the higher frequencies. Even a small amount of aliased energy would significantly effect the apparent coherence in this region which is well below the corner frequency of the 5-pound source. At higher frequencies the aliased energy level is insignificant relative to the amplitude of the direct source energy.

Another measure of the data scatter in the frequency domain is the coefficient of variation (CV) (Bathea, et al., 1985). The CV is the ratio of the standard deviation to the mean, $CV = \frac{s}{\bar{x}}$. CVs for the ART 2 spectra are given in Figure 10. For ART 2, the CV on the radial and vertical components increases with frequency ($CV < 0.5$ from 5 to 30 Hz); the transverse component CV remains approximately constant at a relatively high level (> 0.5) across all frequencies, suggesting that the transverse component is uncorrelated at all frequencies. By way of contrast, Figure 11 shows the very low values of the CV between 5 and 60 Hz. for the radial and vertical components of the Huddle (ART 19) test. The advantage of the CV as an estimator of the data scatter across the array is that all stations in the array may be used in the single estimate as opposed to only a pair of stations in the coherence estimate.

Amplitude spectra of the vertical acceleration waveforms recorded at the 0° azimuth for all five of the ART 11 pit shots are compared in Figure 12. The sets of spectra recorded at the other azimuths and the other components are similar in character to the 0° vertical set. The four pit shot spectra are quite similar in shape and amplitude, while the in situ shot spectrum exhibits a shape which is similar to that of the pit shot spectra, but higher in amplitude for almost all frequencies. Two of the pit shots are almost identical in the frequency domain; pit shots 3 and 4 also group closely together over most of the frequency band. The greatest change in amplitude from shot to shot occurs in the 30-35 Hz. region. This area of the spectrum is fairly flat for the in situ shot; however, a spectral hole develops for the pit shots which deepens with each successive pit shot. Even though the shape of the source spectrum may

change from shot to shot, which is to be expected since introduction of the backfilled cavity results in more energy lost in cratering, greater attenuation and a larger cavity, the CV should change very little if the source remains cylindrically symmetric for all shots. Figure 10 shows the azimuthal coefficient of variation plotted as a function of frequency for the vertical, radial and transverse components, respectively, for all five shots. The normalized standard deviation curves are very similar for all five shots out to the system anti-alias filter at 70 Hz. The coefficient of variation curves from ART 2, which was conducted near the pit shot site but on a different test bed, are also plotted in this figure. The change in the coefficient of variation curves between the two sites is much larger than the variation from shot to shot for the pit shot sequence. The relatively small scatter in the coefficient of variation curves for the five events of the pit shot sequence (the in situ shot plus the four pit shots) suggests that source asymmetry plays an unimportant role in the development of the azimuthal variation in ground motion response.

The ART 111-2 (Table 1) shot was designed to determine the degree to which azimuthal variation increases with range from the source. In this test ground motions were recorded by circular arrays at both the 10 m and 30 m ranges. Coefficient of variation plots for the vertical, radial and transverse spectra for both the 10-m and 30-m ranges are given in Figure 13. These results support the contention that the coefficient of variation increases with range.

RELATION OF OBSERVED AZIMUTHAL VARIABILITY TO TEST SITE

GEOLOGY

The tests discussed in this paper were conducted at the same test site in the Rio Grande Valley south of Albuquerque, New Mexico. The subsurface geology consists of dry alluvium down to the water table at a depth of approximately 75 meters. The site lies in a small shallow basin which in earlier times contained a playa. In general, the site is underlain by unconsolidated eolian sands, alluvium and lacustrine deposits 15-30 meters thick. Beneath this material are the tertiary Santa Fe and Galisteo formations, 180-300 meters thick (Bedsun, 1983). A typical near-surface P wave velocity section is shown in Figure 14 (Stump and Reinke, 1982).

Near-surface deposits are fairly variable with intermittent caliche beds present. Trenching at other test sites in the area has revealed discontinuous subsurface caliche beds typically on the order of 0.5 to 1.0 m in thickness (Stump and Reinke, 1982). In an effort to quantify the nature of the subsurface variability at the ART 2 test site, 18 boreholes were drilled within the confines of the testbed, as shown in Figure 15. Each borehole was drilled to depth of 6.1 meters. Standard penetration tests were performed in each hole. The standard penetration test (SPT) involves determining the number of hammer blows required to drive a sampling tube a unit distance. This blow count is related to the in-situ density and compressive strength of the subsurface material (Terzaghi and Peck, 1967). Figure 16 displays the blow counts per meter for each borehole down to the 6-meter depth. Figure 15 contains isopach maps showing the lateral distribution of the areas of similar blow

counts as a function of depth.

A thorough understanding of the physical processes responsible for the observed azimuthal variability in the ART 2 test requires that a quantitative relationship be established between the subsurface material property information and the observed ground motion characteristics. Aki and Richards (1980) present such a relationship. Following Chernov (1960) they characterize the statistical nature of geologic media by the autocorrelation of the velocity fluctuation.

For $\mu = -\delta C/C_0$, where C_0 = velocity, the normalized autocorrelation function is defined by:

$$N(r) = \langle \mu(r') \cdot \mu(r'+r) \rangle / \langle \mu^2 \rangle$$

where r denotes position.

Two statistical distributions are considered:

- (1) the exponential distribution: $N(r) = e^{-|r|/a}$
- (2) the gaussian distribution: $N(r) = e^{-r^2/a^2}$

The quantity a is the measure of scale length of the medium inhomogeneity called the correlation distance.

Once a medium is described statistically in terms of $N(r)$ then the Born scattering approximation may be used to determine the strength of the scattering as a function of frequency for the medium. The Born approximation assumes that the primary waves are unchanged by propagation through a scattering medium so that energy conservation is violated. Only single scattering is considered. Following Aki and Richards (1980) the ratio of scattered energy to total energy is given as follows:

$$\delta I/I = 8\langle\mu^2\rangle\cdot k^4\cdot a^2\cdot L \text{ for } ka < 1, \text{ and}$$

$$\delta I/I = 2\langle\mu^2\rangle\cdot k^2\cdot a\cdot L \text{ for } ka > 1.$$

where $\delta I/I$ is the ratio of scattered energy to the total energy carried by the wave, $\langle\mu^2\rangle$ is the average of the square of the velocity perturbation, k is the wave number, a is the scale length or correlation distance of the medium, and L is the length of the travel path.

Making the assumption that there is a linear correlation between the blow count value at a particular point and the P wave velocity at the same point we shall attempt to relate the observed azimuthal variability in the ART 2 data with the blow count data using the scattering theory discussed above. The mean was computed for the set of blow count data for all of the holes. This yields a mean value of 50 blows/0.30 meter. This value was treated as C_0 in the scattering equations. The autocorrelation function was then computed of the following ratio: $(BC_i - BC)/BC$, where BC_i is the individual blow count value, BC is the mean value of all blow counts. The autocorrelation functions were computed separately for each hole.

Values of the autocorrelation functions of the blow count data for all of the holes are plotted in Figure 17. Also plotted in Figure 17 are several theoretical autocorrelation functions for different values of the correlation length a , for both the Gaussian and exponential distributions. Based on examination of these plots the theoretical distribution function which best fits the data is apparently an exponential function with a scale length between 2.0 and 3.0 meters. This scale length applies, of course, only to the vertical distribution of inhomogeneities.

The horizontal inhomogeneity scale length could well be different in character. The horizontal spacing of the boreholes (≈ 6.7 m) is much too wide to allow any sort of reasonable estimate of the horizontal scale length (this spacing yields a nyquist wavelength of 13.4 m).

Using the Born equations, the ratio of scattered energy to total energy, $(\delta I/I)$, was computed for the ART 2 test-bed using several values of the inhomogeneity scale length as shown in the plots in Figure 18. The $ka \ll 1$ case is appropriate for most of the frequency-scale length combinations under consideration here. The $ka \gg 1$ case is appropriate for scale lengths greater than 2 m in the higher frequency region (>20 Hz). Both curves indicate that for scale lengths of 2.0 to 3.0 meters significant ($\delta I/I > 0.10$) scattering begins near 10 Hz. Significant scattering in the ART 2 test data occurs above 30-35 Hz (Figure 4). There are several possibilities for this apparent poor correlation: (1) the Born approximation is valid only for small values of scattered energy; (2) the autocorrelation function which was derived pertains only to the vertical distribution of inhomogeneity and thus the scale length which is appropriate for the overall propagation medium could be considerably different from 2.0-3.0 meters; (3) a finer spatial sampling of the near surface blow count values might well yield a smaller scale length; and (4) the assumed correlation between blow count data and P wave velocity may be incorrect.

To determine the effect of varying the scale length upon the theoretical scattered energy, $\delta I/I$ as a function of frequency was computed for correlation lengths of 1.0 m, 0.5m and 0.25m (Figure 18). For these scale lengths, the frequency at which scattering becomes significant is in the 25-30 Hz. region.

This result, particularly the 0.5 curve, correlates much better with the observed threshold of incoherence in the ART 2 test. A correlation scale length in the neighborhood of 0.5 - 1.0 m is also not unreasonable in light of the results of the "Huddle" test (ART 19) in which all of the instrumentation was placed in a group approximately 1 meter in width (Figure 5). Examination of the spectra from this test in Figure 6 reveals that the spectra of the endmost instruments separated by a distance of approximately 1 meter begin to diverge; whereas, the spectra from instruments spaced more closely correlate very well. Shallow trenching in the general test site area suggests that a typical caliche bed thickness is on the order of 0.5 to 1.0 m. although a typical lateral extent may be slightly greater (Stump and Reinke, 1982).

This simple forward model indicates that the azimuthal variability in the ART 2 data can be explained with a scattering model based upon the Born approximation. The implication is that the particular standard penetration test array did not properly characterize the appropriate scale length due to inadequate horizontal or vertical spatial sampling since blow count values were obtained by counting the number of blows required to drive the sampling tube a distance of 0.6 meter. This sample interval yields a Nyquist wavelength of 1.2 m.

DISCUSSION AND CONCLUSIONS

The results of the ART experiments have shown, at least for this particular alluvial test site, that the predominant cause of azimuthal variation in ground motion response is inhomogeneity in near-surface geologic material rather than very near-source asymmetry. Considering that this particular site in general is thought to have a fairly uniform near-surface geologic composition, the degree of azimuthal variation observed from these small tests is fairly remarkable. Experiments of this type should be performed at several sites to further constrain the relationship between the spectral coefficient of variation and the variation in the geologic structure. Such surveys will aid greatly in the interpretation and understanding of ground motion data from small-scale field tests. It is clear that for a small-scale test performed at the ART 2 site, deterministic interpretations of the data cannot be made above the 30-35 Hz region. Coefficient of variation surveys could also place limitations upon the interpretation of near source, regional, and teleseismic measurements of earthquakes and explosions made at a single point. These surveys may be useful in explaining the lack of coherence between individual station pairs in small seismic arrays, such as the Pinon Flat array (Vernon et al., 1985).

In this study an initial attempt was made at relating the available subsurface information at the ART 2 site with the observed waveform variation in the test. This attempt was not very successful, probably due to insufficient spatial resolution of the subsurface sampling performed. Forward modeling argues that the scale lengths which are present in the ART 2 test-bed

are perhaps on the order of 0.5-1.0 m rather than 2.0-3.0 meters as determined from the autocorrelation of the standard penetration test blow count data. Use of other sampling techniques, such as the seismic cone penetrometer test (in which the force necessary to drive a rod into the ground is measured and a geophone in the rod tip is used to perform a velocity survey) could enable much finer spatial resolution to be obtained both horizontally and vertically allowing a greatly improved characterization of the random properties of the medium.

ACKNOWLEDGEMENTS

Funding for the experiments was provided by the Air Force Weapons Laboratory Independent Research Program under projects ILIR8207 and ILIR8414. Additional support was provided by The Air Force Office of Scientific Research through grant AFOSR-84-0016 to Southern Methodist University.

REFERENCES

- Aki, K. and P. Richards, 1980, Quantitative Seismology: Theory and Methods, W.H. Freeman and Company, San Francisco, 2 volumes, 932 pages.
- Bethes, R., B. Duran and T. Boullian, 1985, Statistical Methods for Engineers and Scientists, Marcel Dekker, Inc., New York, 1985, 698 pages.
- Bedsun, D., 1983, Summary of geotechnical testing and material models for subsurface soil conditions at McCormick Ranch, Kirtland AFB, New Mexico, Letter Report, NMERL 7.11-TA7-20.
- Chernov L., 1960, Wave Propagation in a Random Medium, McGraw-Hill, New York, 168 pages.
- McLaughlin, K., L. Johnson and T. McEvilly, 1983, Two-dimensional array measurements of near-source ground accelerations, Bulletin of the Seismological Society of America, Vol 73, No. 2, pp 349-376.
- Smith, S.W., J. Ehrenberg and E. Hernandez, 1982, Analysis of the El Centro differential array for the 1979 Imperial Valley Earthquake, Bulletin of the Seismological Society of America, Vol 72, No. 1, pp 237-258.
- Stump, B. and R. Reinke, 1982, Spall-Like Waveforms Observed in High Explosive Testing in Alluvium, AFWL TR-82-15, 122 pp., Air Force Weapons Laboratory, Kirtland AFB, N.M.
- Stump, B. and R. Reinke, 1987, Experimental confirmation of superposition from small scale explosions, submitted to the Bulletin of the Seismological Society of America
- Vernon, F., J. Fletcher, L. Haar, T. Bolswick, E. Sembera, and J. Brune, 1985, Spatial coherence of body waves from local earthquakes recorded on a small aperture array, EOS: Transactions of the American Geophysical Union, Vol 66, No. 46, p 954 (abstract).
- Terzaghi, K. and R. Peck, 1967, Soil Mechanics In Engineering Practice, John Wiley and Sons, New York, 729 pages.

LIST OF ILLUSTRATIONS

- Figure 1. Experimental Layout for the ART 2 Test Event.
- Figure 2. Filtered Vertical Acceleration Records from ART 2. Record Length is 0.5 Seconds.
- Figure 3. Filtered Radial Acceleration Records from ART 2. Record Length is 0.5 Seconds.
- Figure 4. Vertical and Radial Fourier Acceleration Spectra for ART 2.
- Figure 5. Experimental Layout for Huddle Test.
- Figure 6. Vertical and Radial Fourier Acceleration Spectra from Huddle Test.
- Figure 7. Test-Bed Layout for the ART 11 Tests.
- Figure 8. Computed Coherencies for ART 2.
- Figure 9. Mean and Variance of ART 2 Spectral Ensembles.
- Figure 10. Spectral Coefficient of Variation Curves for the ART 11 Pit Shots Compared with ART 2.
- Figure 11. Spectral Coefficient of Variation Curves for the Vertical and Radial Components of the Huddle Test.
- Figure 12. Comparison of Vertical Acceleration Spectra for the Five Shots of the ART 11 Series.
- Figure 13. Comparison of 10-m and 30-m Coefficient of Variation Curves for ART 111-2.
- Figure 14. Generalized Geologic Cross Section of McCormick Ranch.
- Figure 15. Layout of Boreholes Within the ART 2 Test-Bed and Isoach Map of Blow Counts.
- Figure 16. Plots of Blow Counts vs Depth (Data points from all 18 boreholes are included).
- Figure 17. Experimental Autocorrelation Function Compared with Gaussian and Exponential Autocorrelation Functions (The lines on the plot are the theoretical autocorrelation functions, the experimental autocorrelation functions from all holes are represented by data points).
- Figure 18. Plot of Scattered Energy as a Function of Frequency for Different Scale Lengths.

TABLE 1

Experiment	Description
ART 2	Single 5-lb. charge buried at 1 meter. Recording array - 6 triaxial accelerometers at different azimuths at the 20 m. range.
ART 19	"Huddle Test". Single 5-lb. charge buried at 1 meter recorded by 6 triaxial accelerometers in a closely spaced group at the 20 m. range
ART 11	The "Pit Shots". Series of five 5-lb buried charges all fired at the same ground zero and recorded by 6 triaxial accelerometers spaced at equal azimuths at the 20 m. range. The initial charge was detonated in situ, subsequent charges were fired in a sand filled pit.
ART 111-2	Single 5-lb buried charge recorded by 6 accelerometers at the 10 m. range and 6 accelerometers at the 30 m. range. Accelerometers spaced at equal azimuths.

ART 2 CONFIGURATION

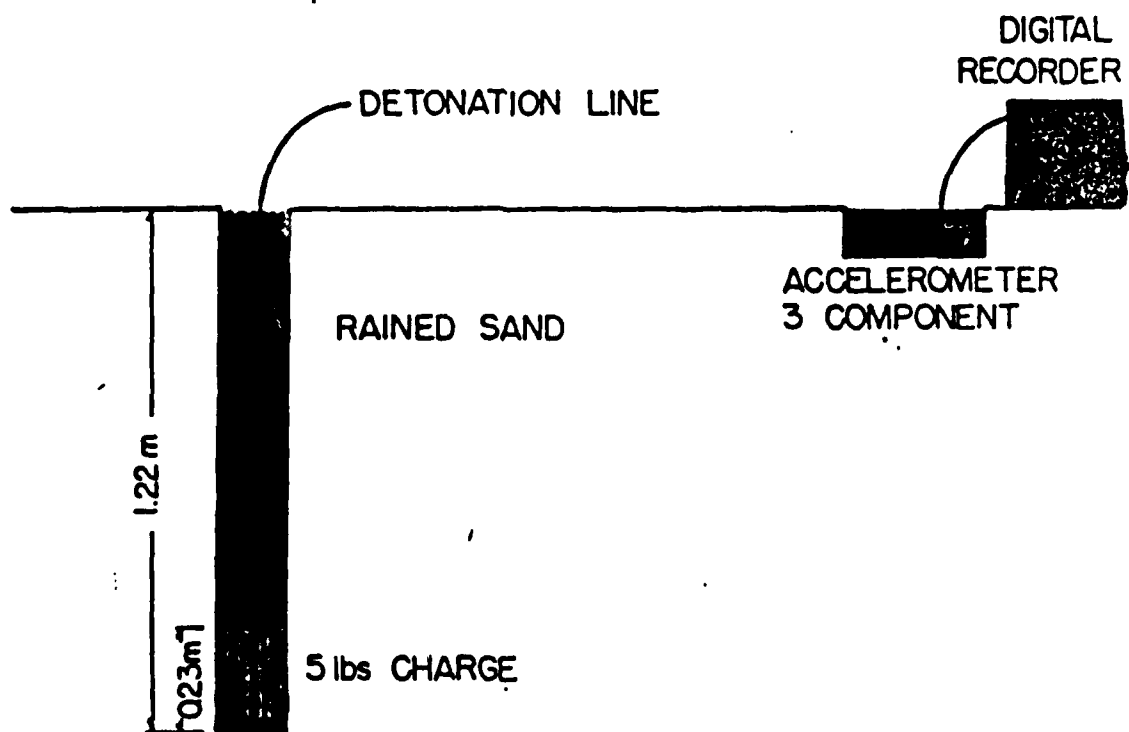
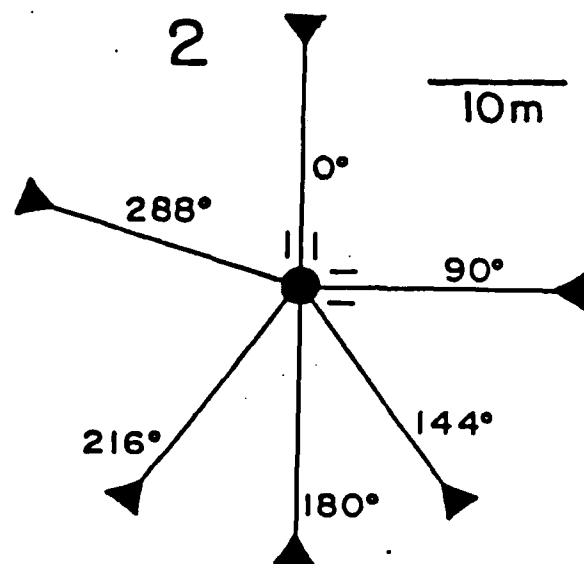


Figure 1.

ARTS 2 VERTICAL

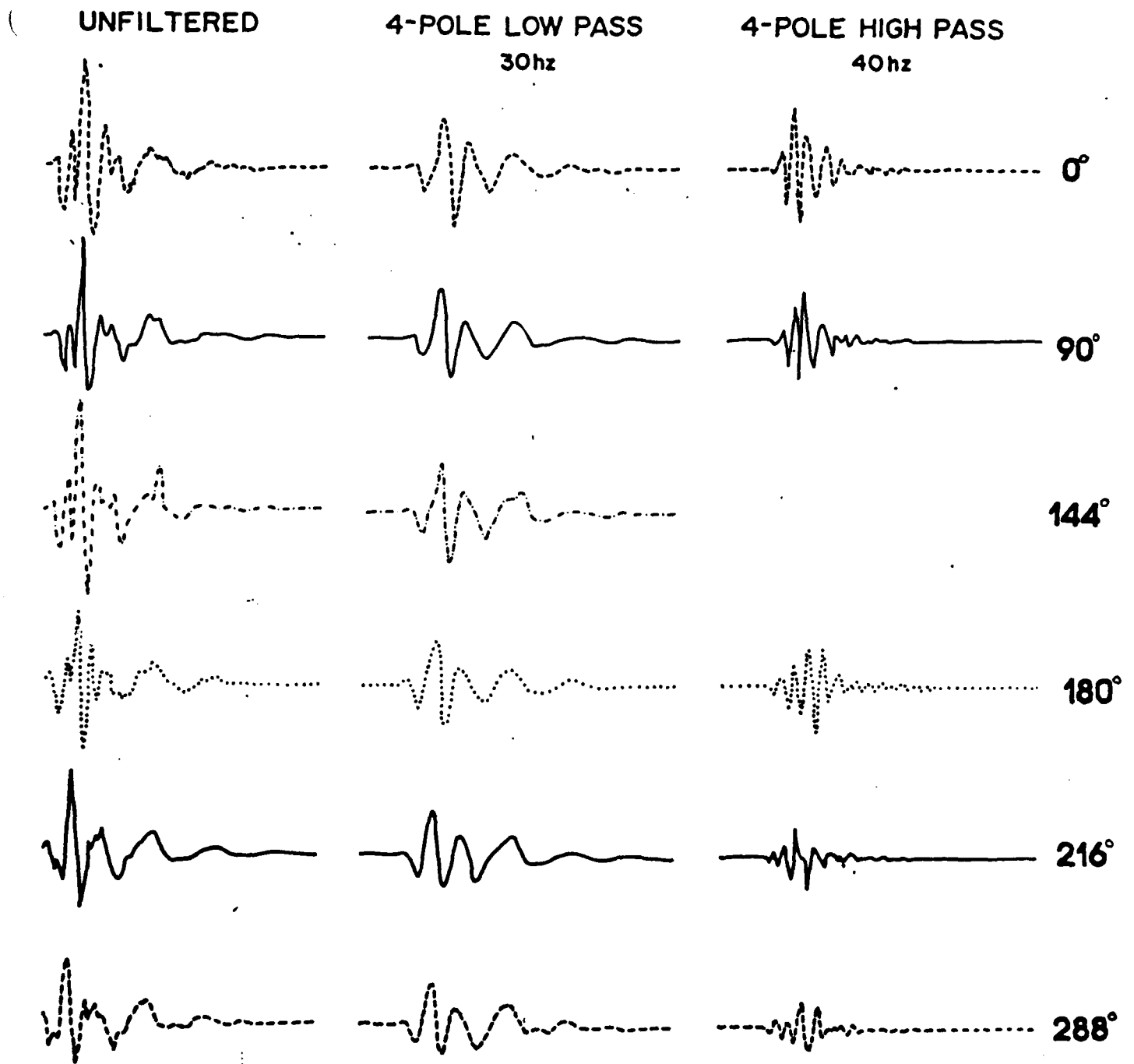


Figure 2.

ARTS 2 RADIAL

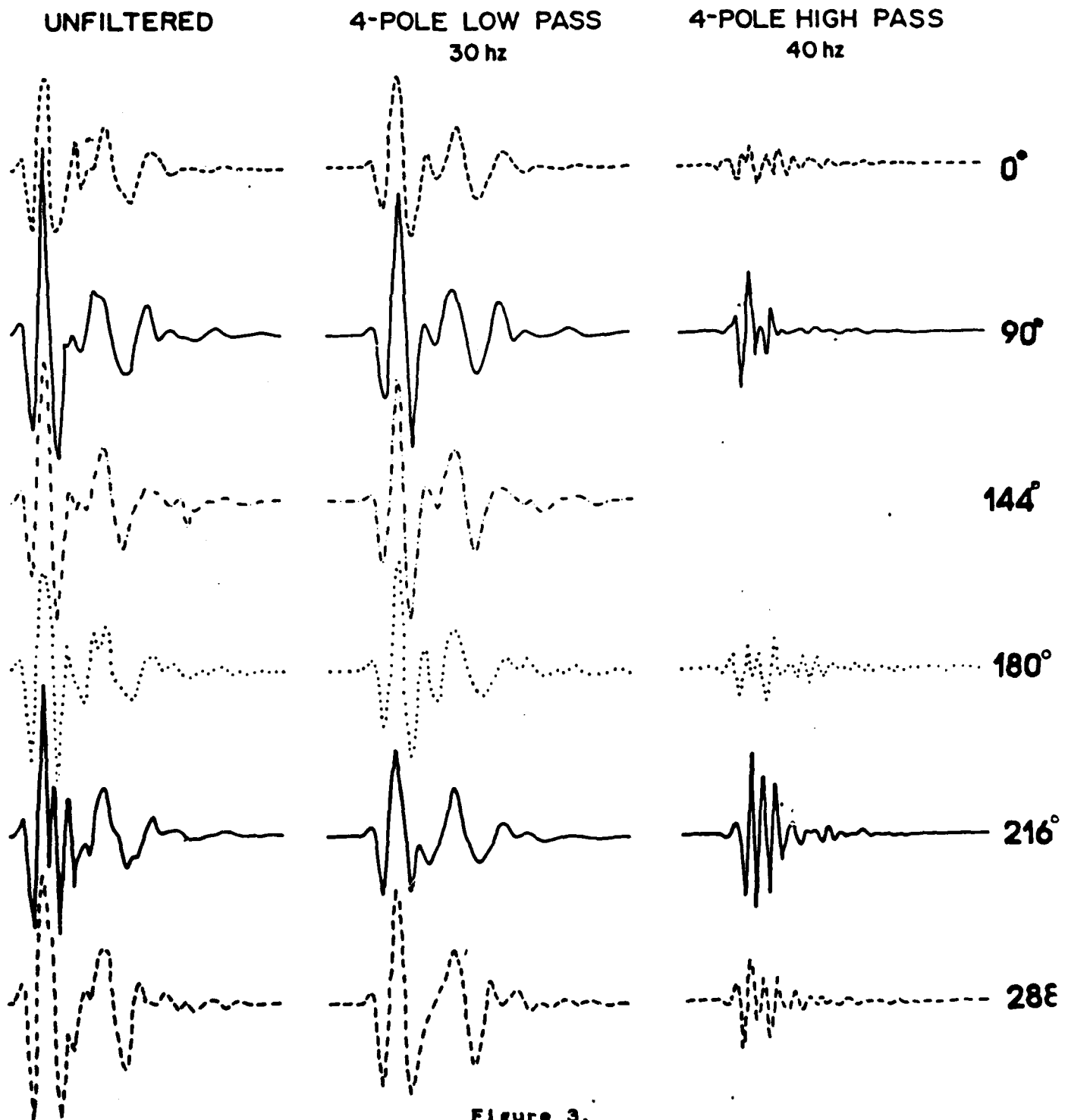


Figure 3.

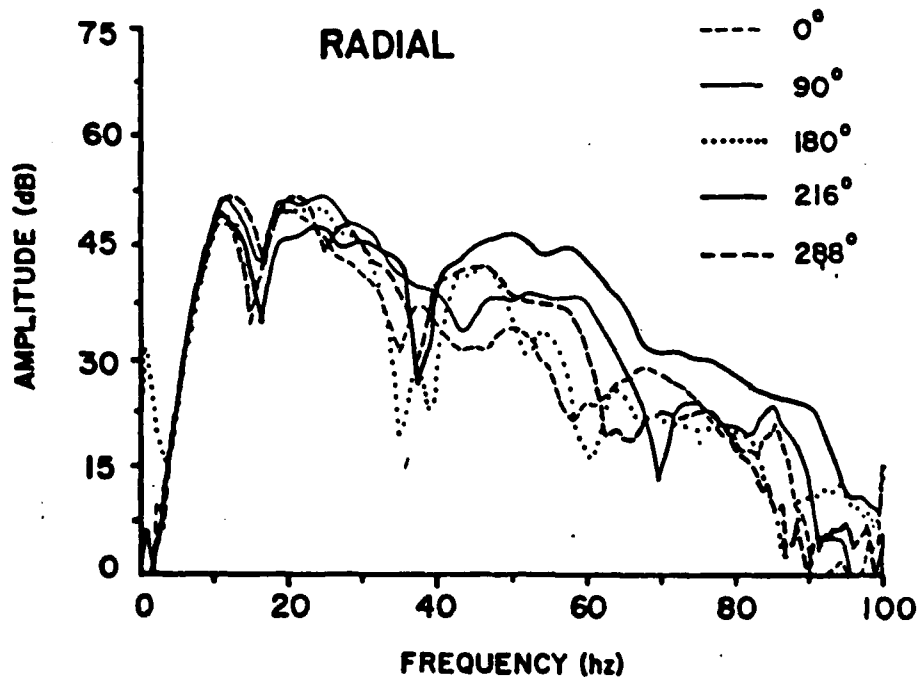
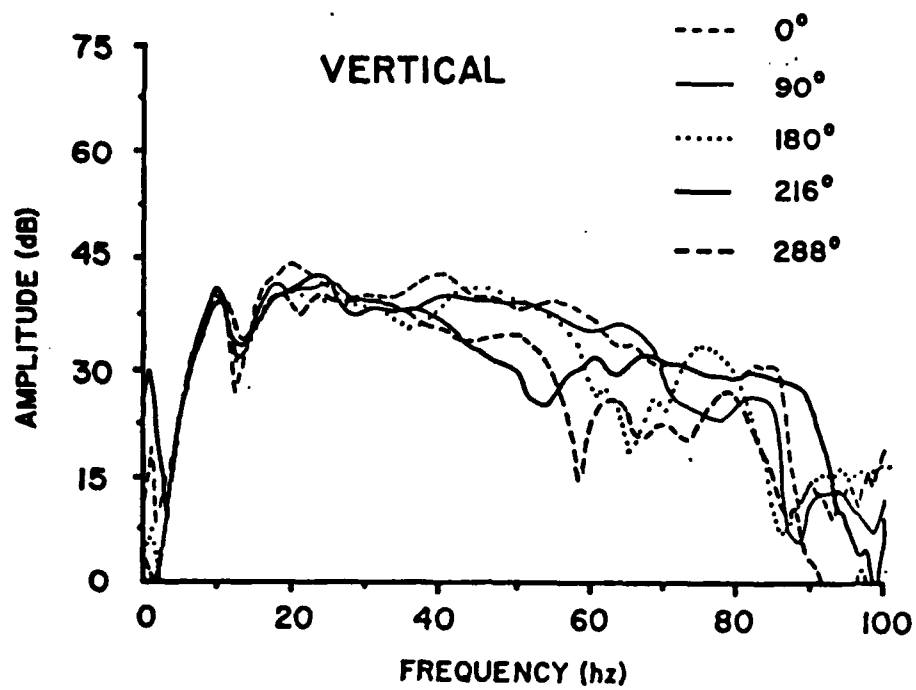


Figure 4.

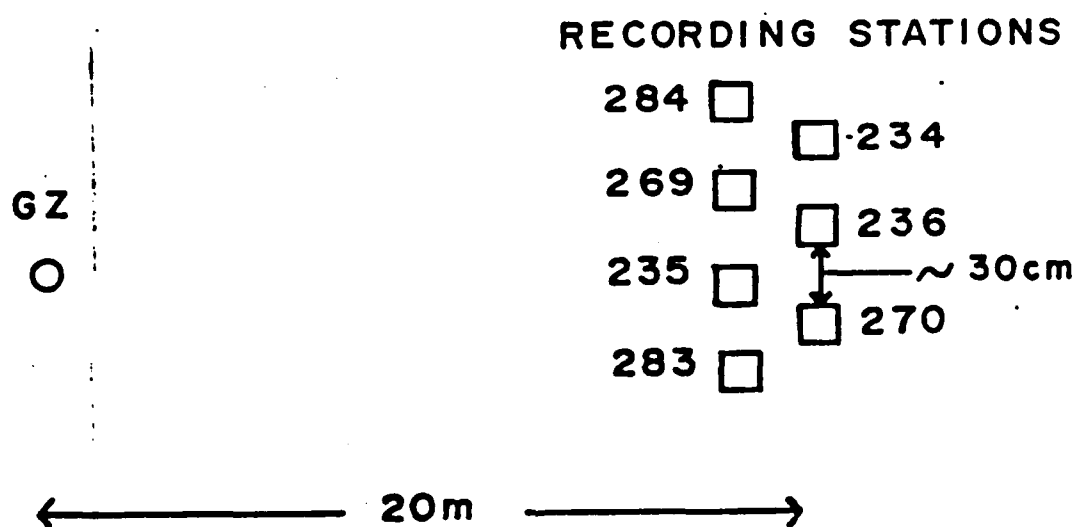


Figure 5.

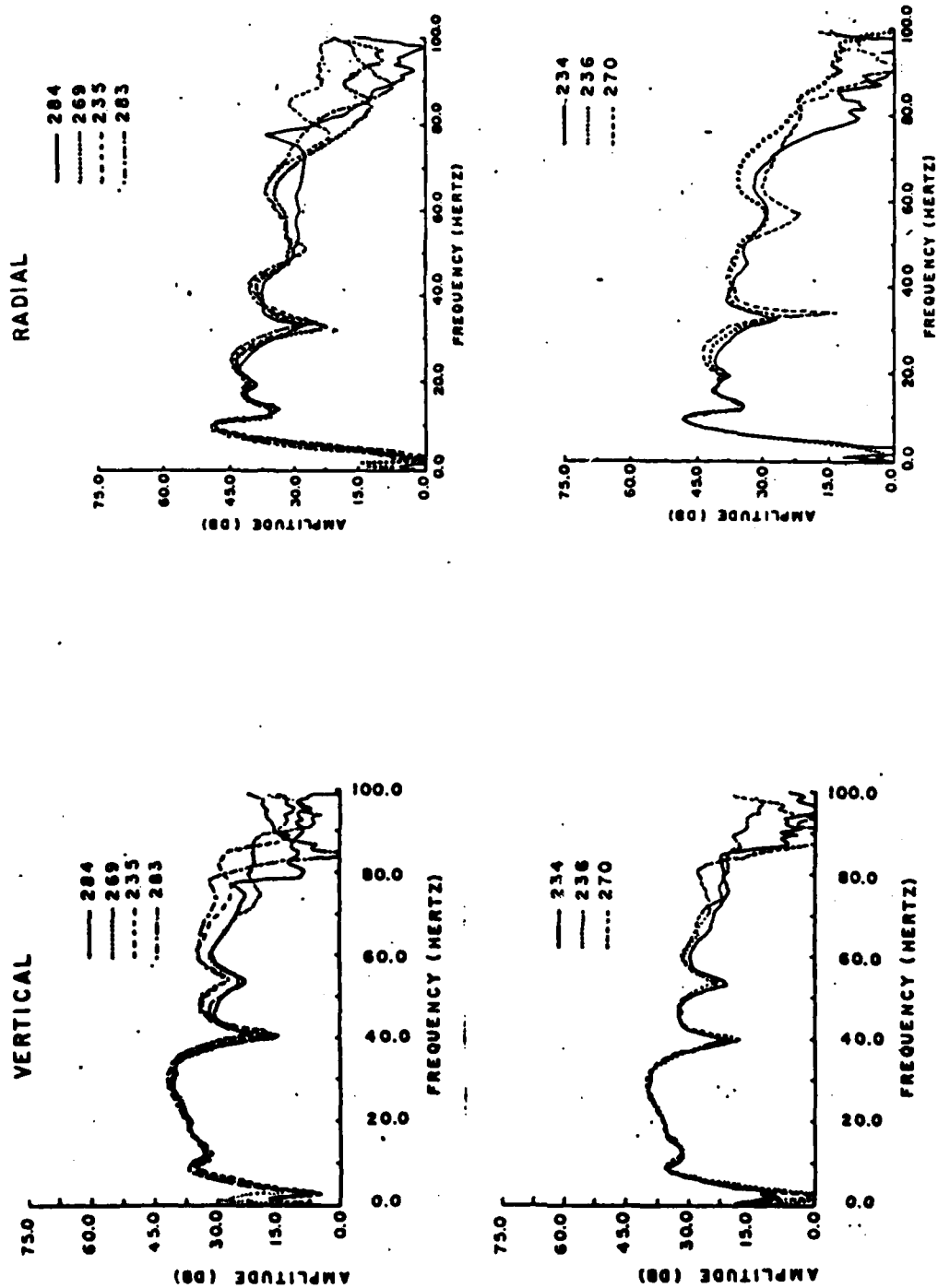


Figure 6.

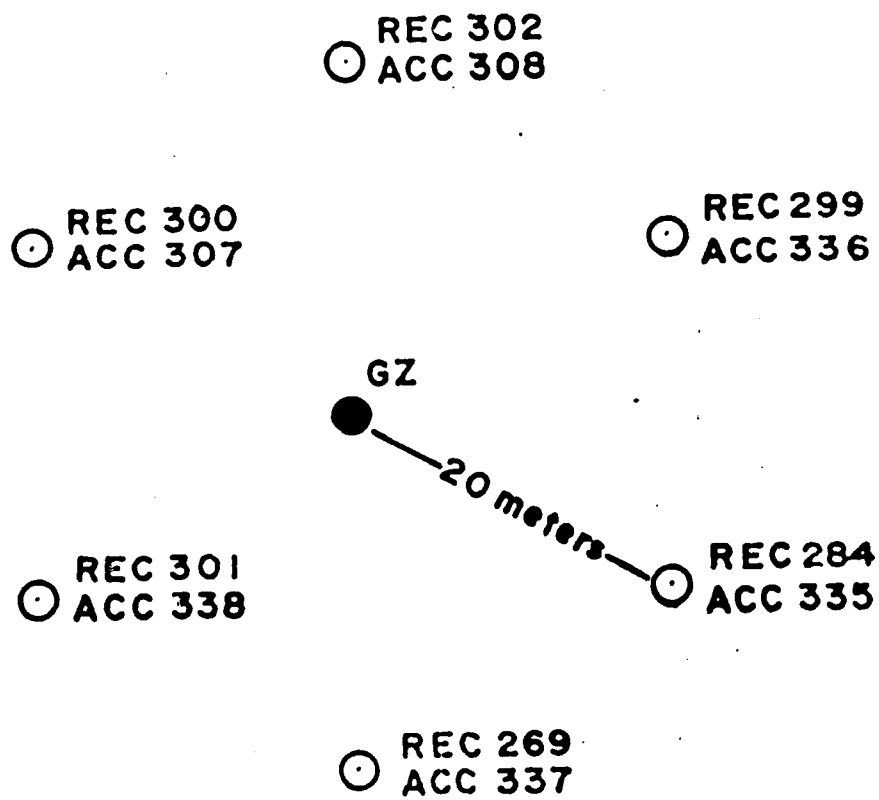


Figure 7.

COHERENCE WITH 0° DATA

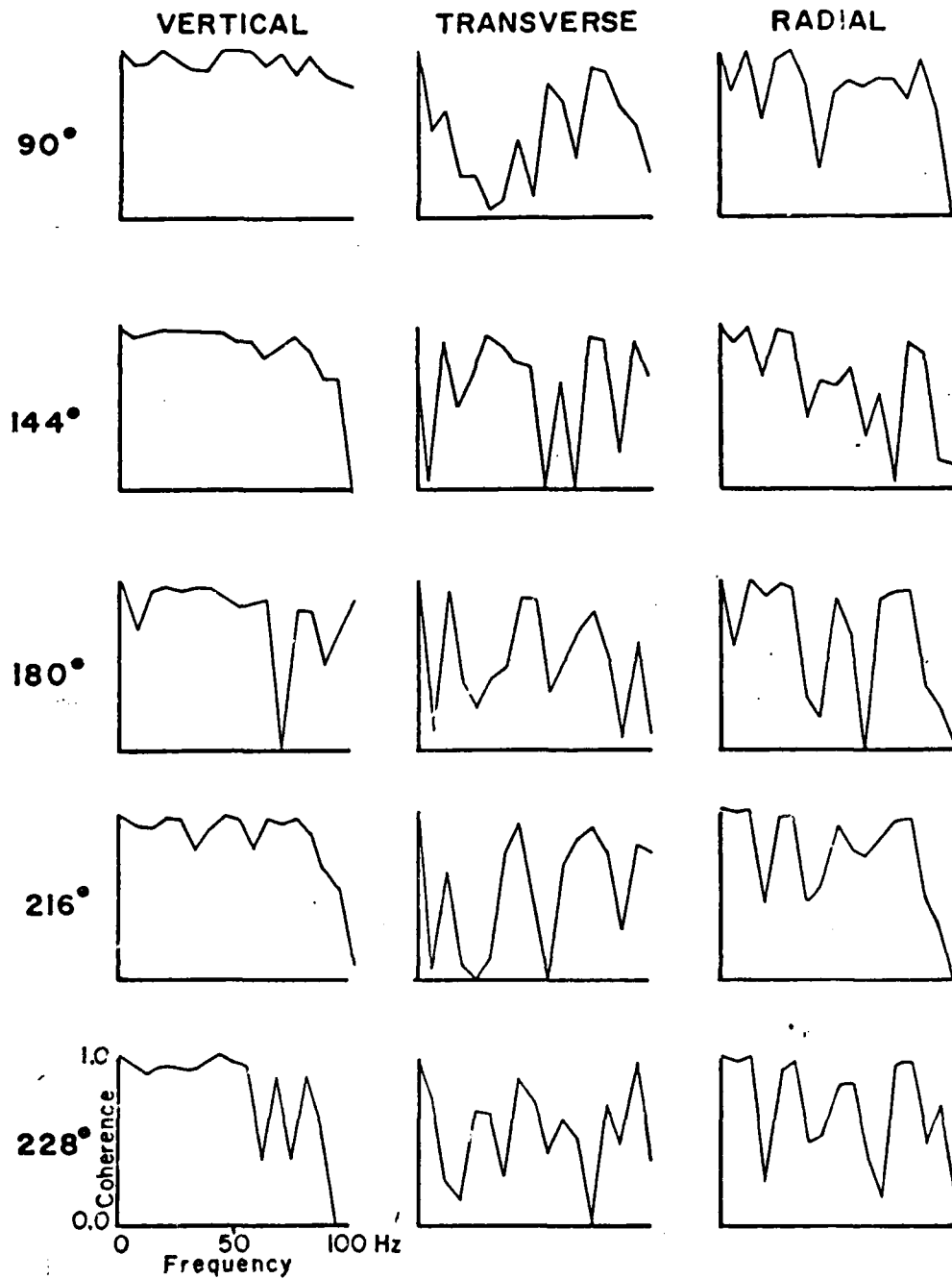


Figure 8.

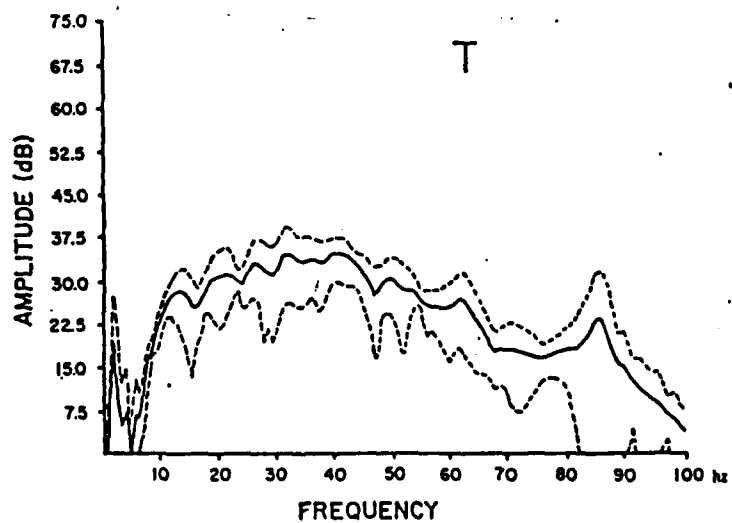
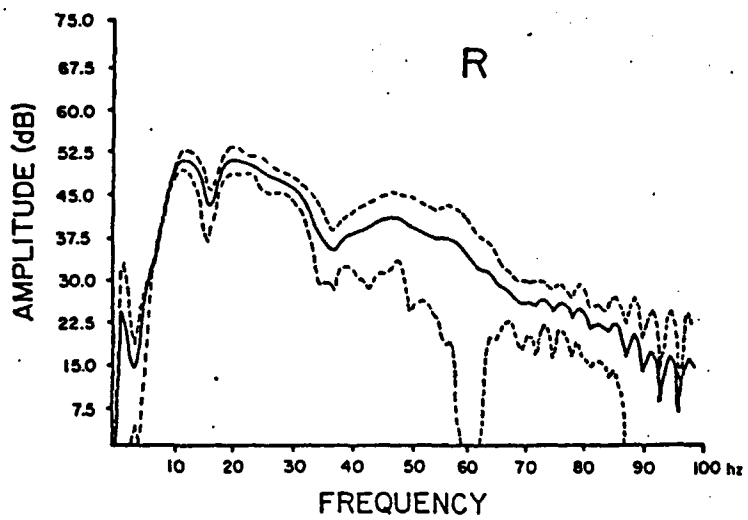
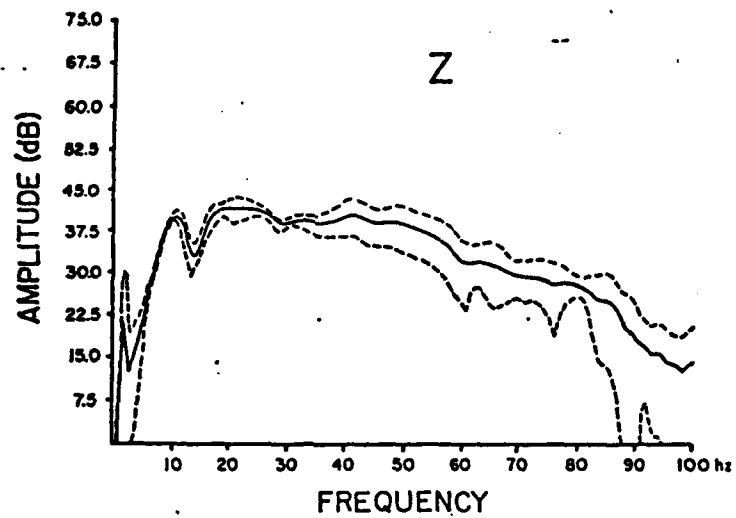


Figure 9.

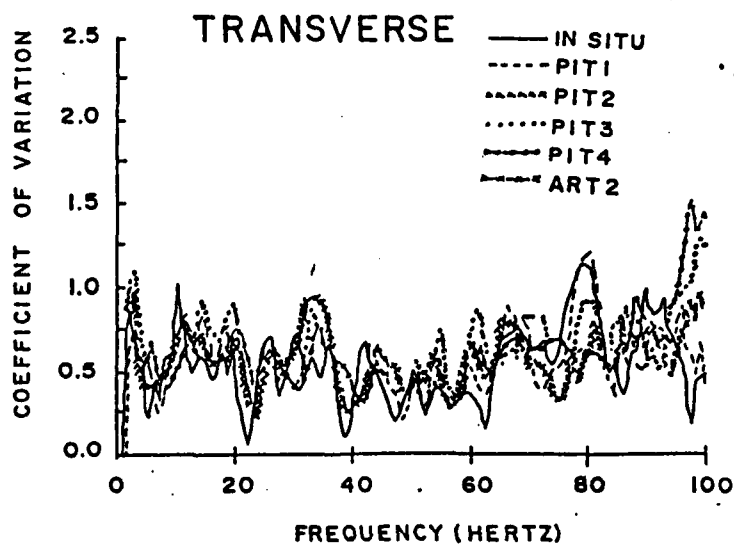
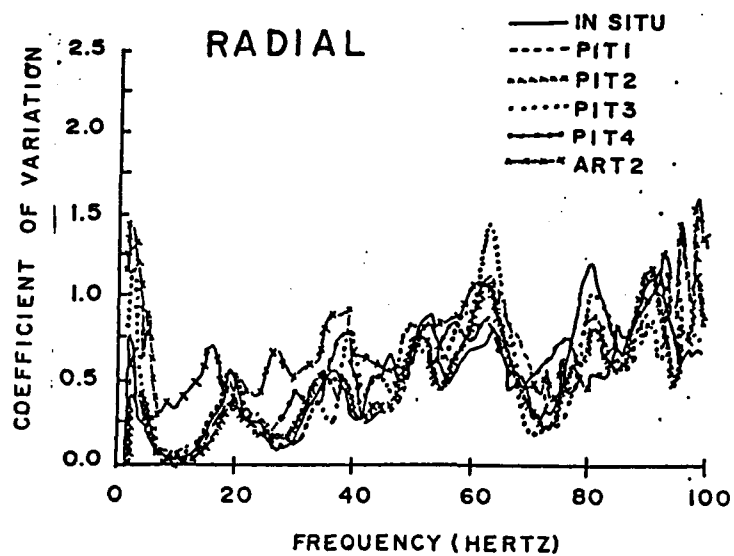
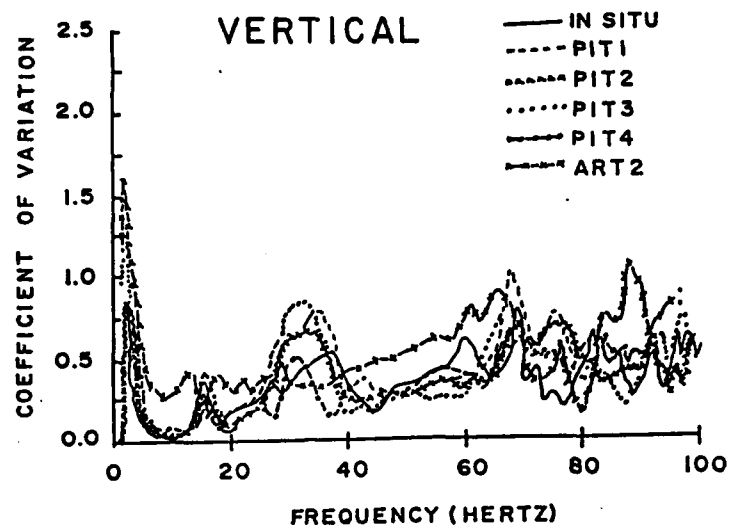


Figure 10.

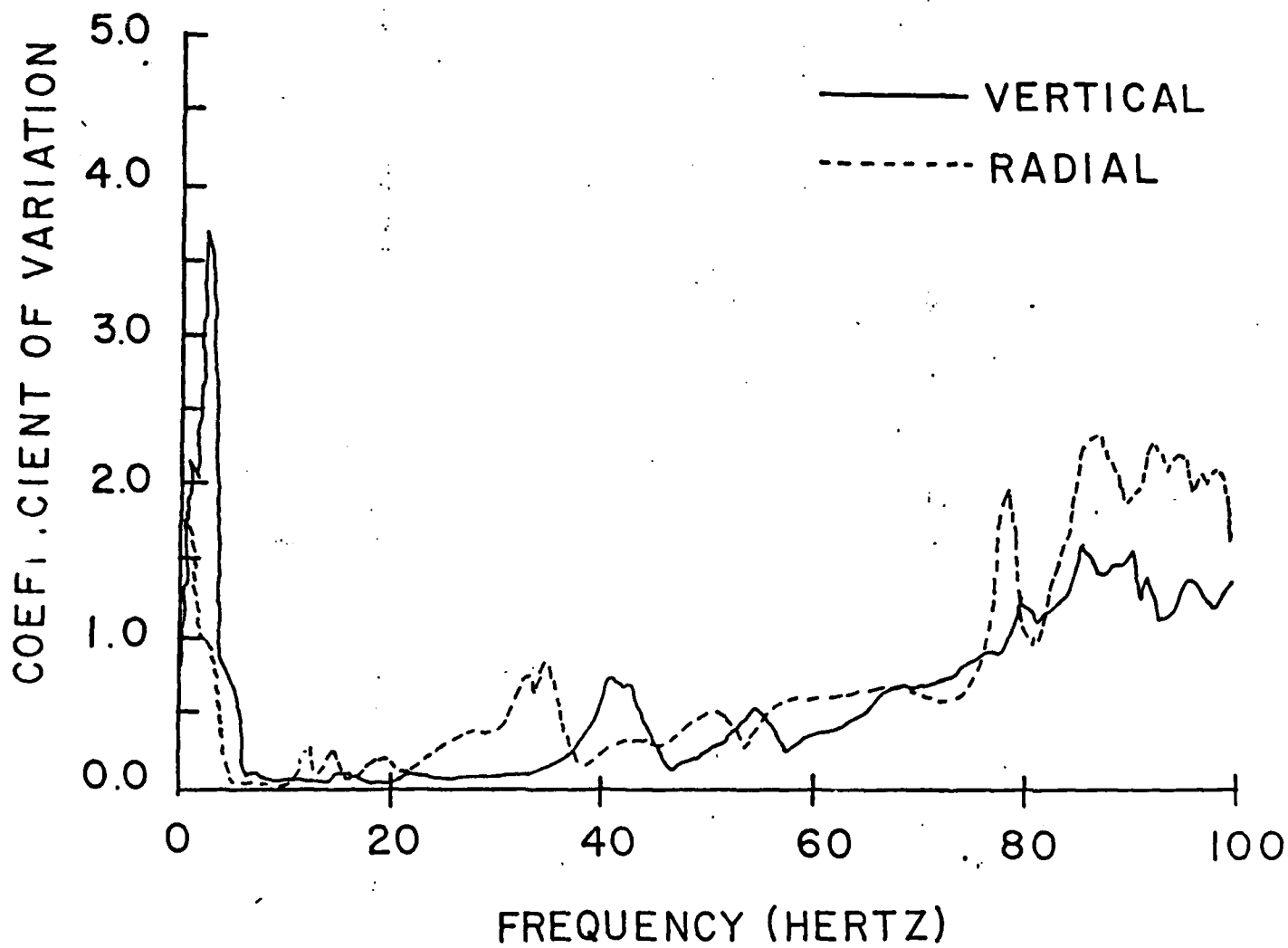


Figure 11.

VERTICAL

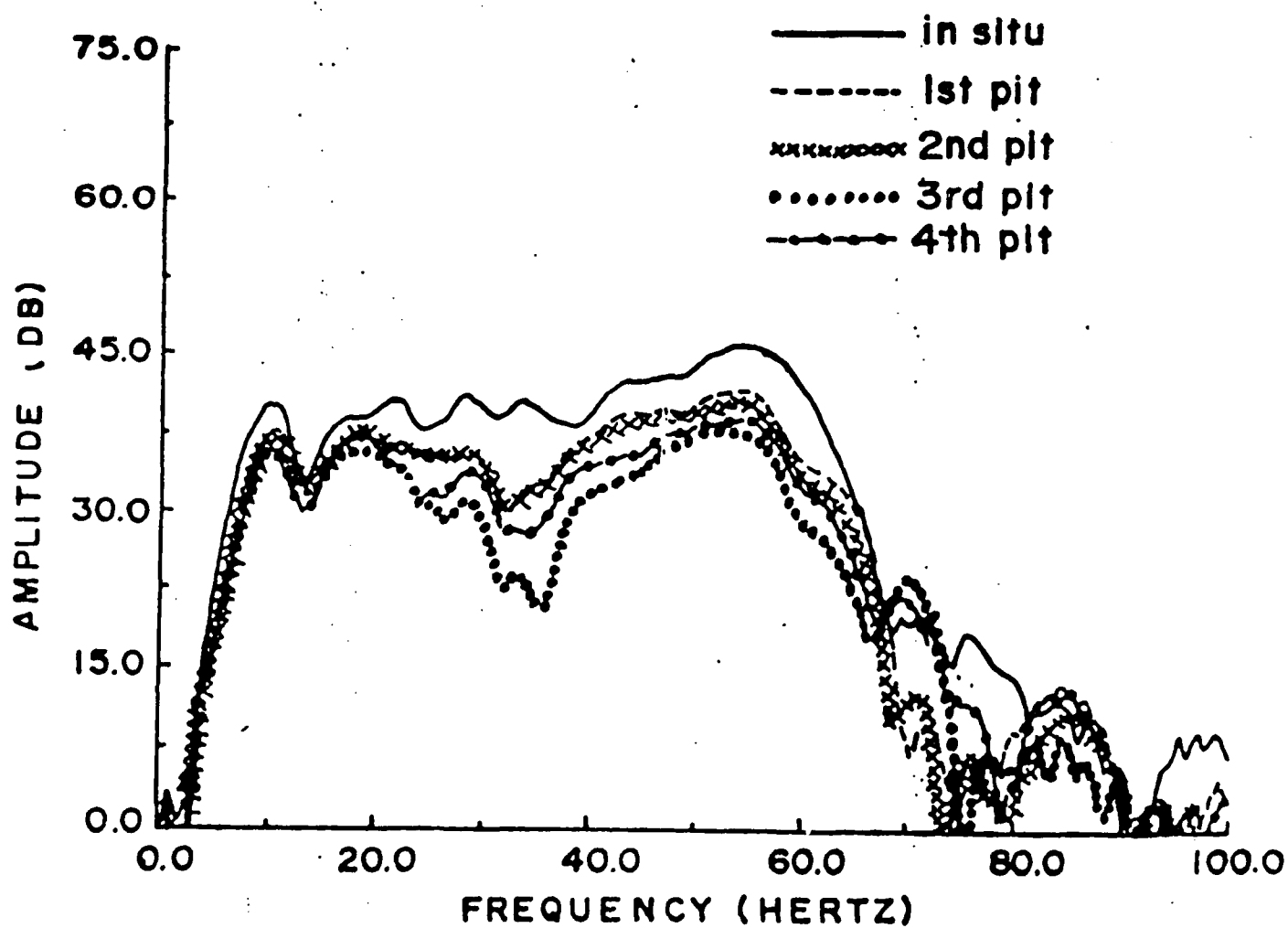


Figure 12.

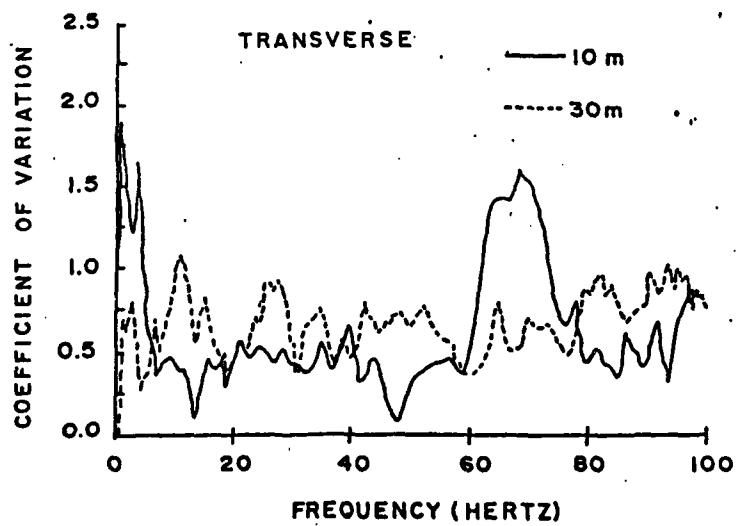
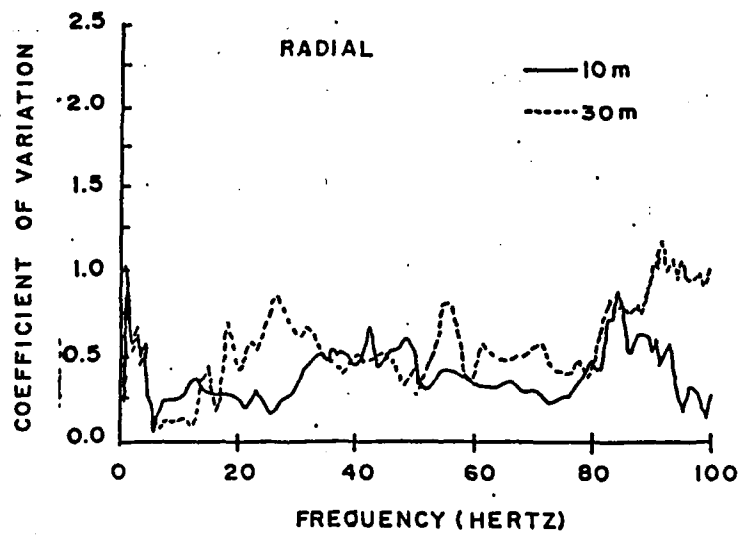
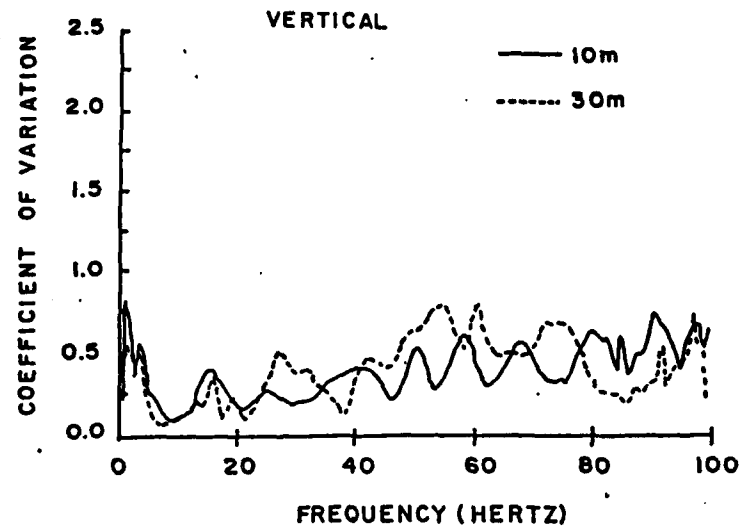


Figure 13.

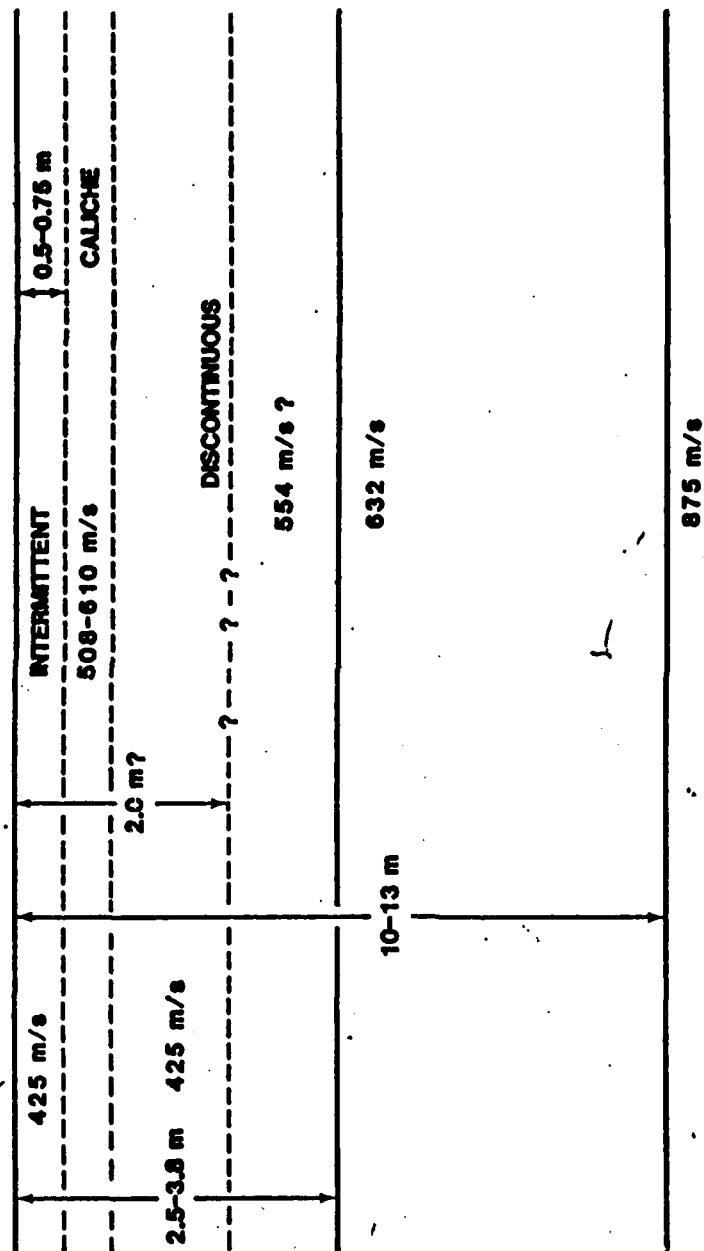


Figure 14.

PENETRATION TEST — ARTS

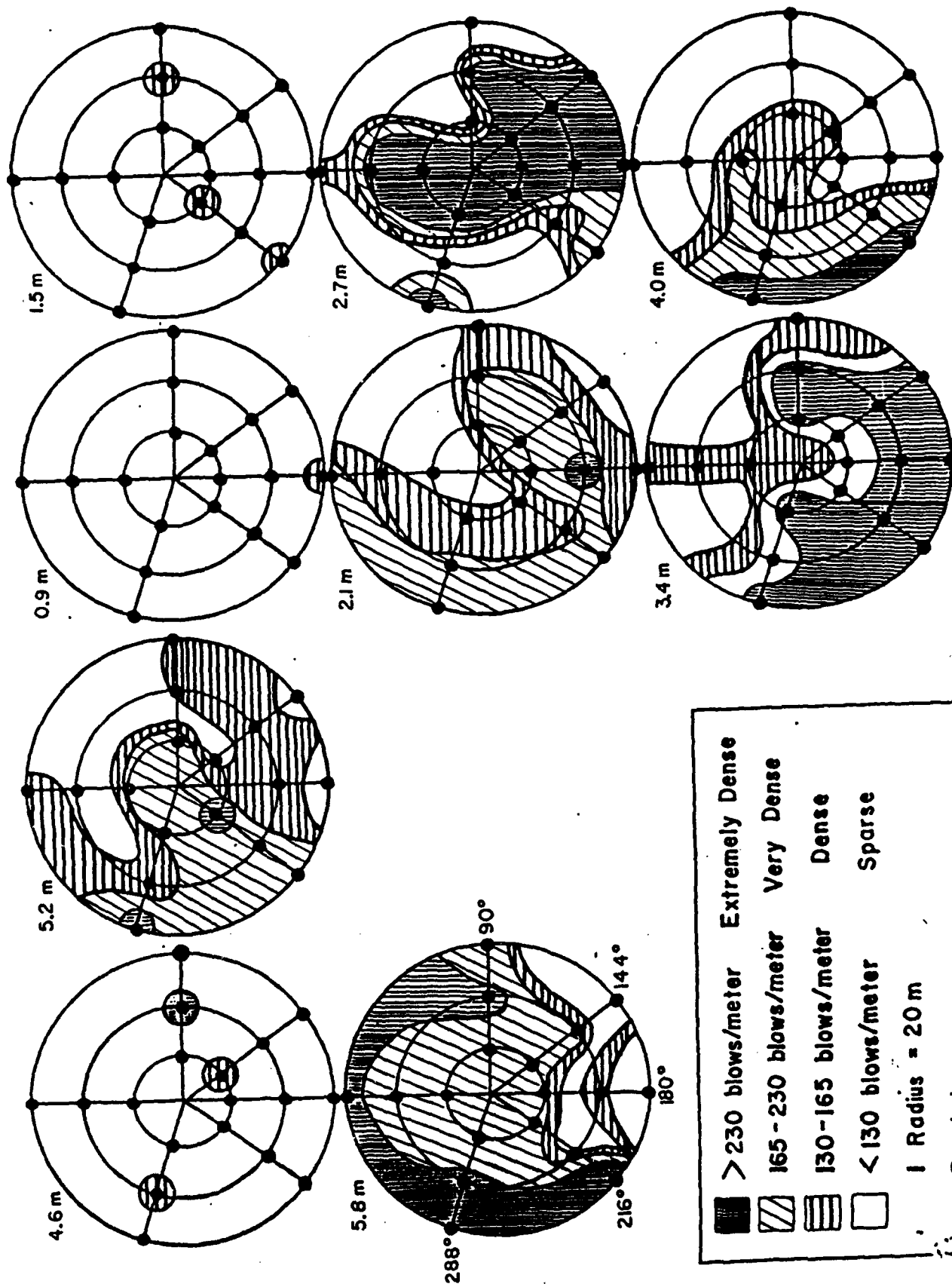


Figure 15.

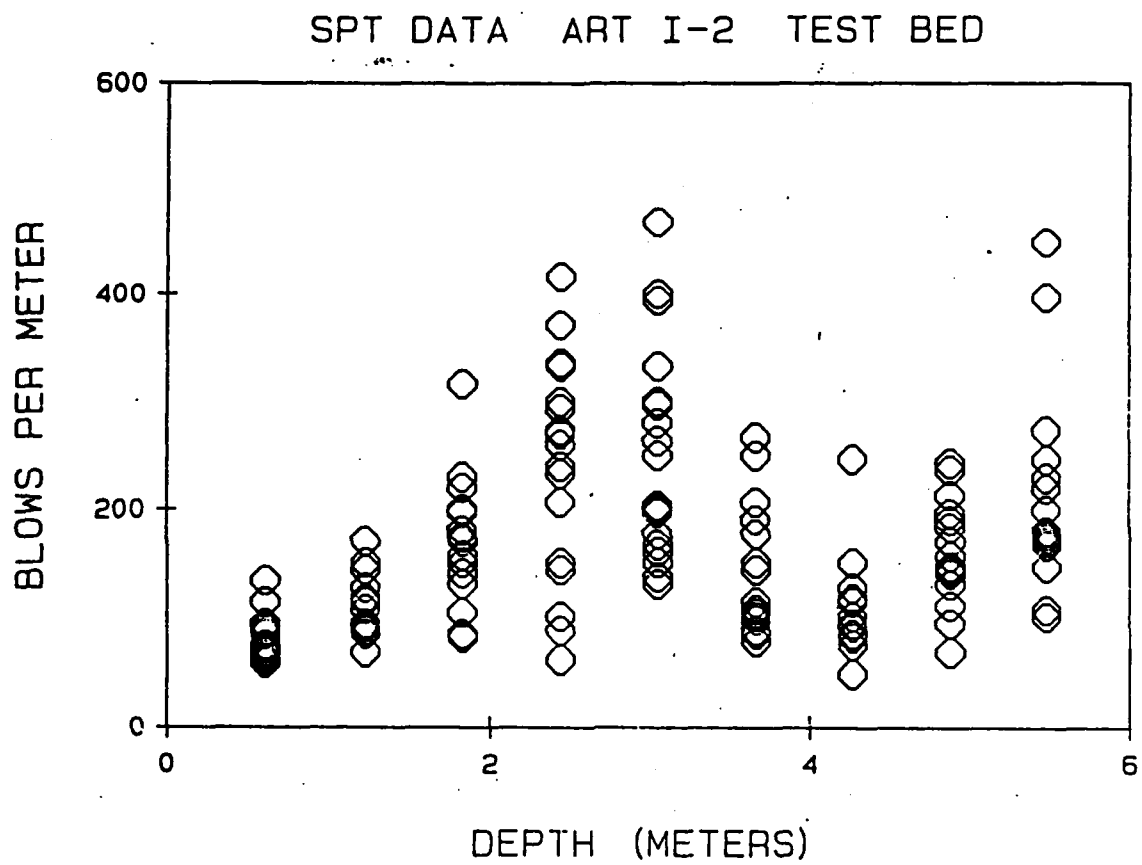


Figure 16.

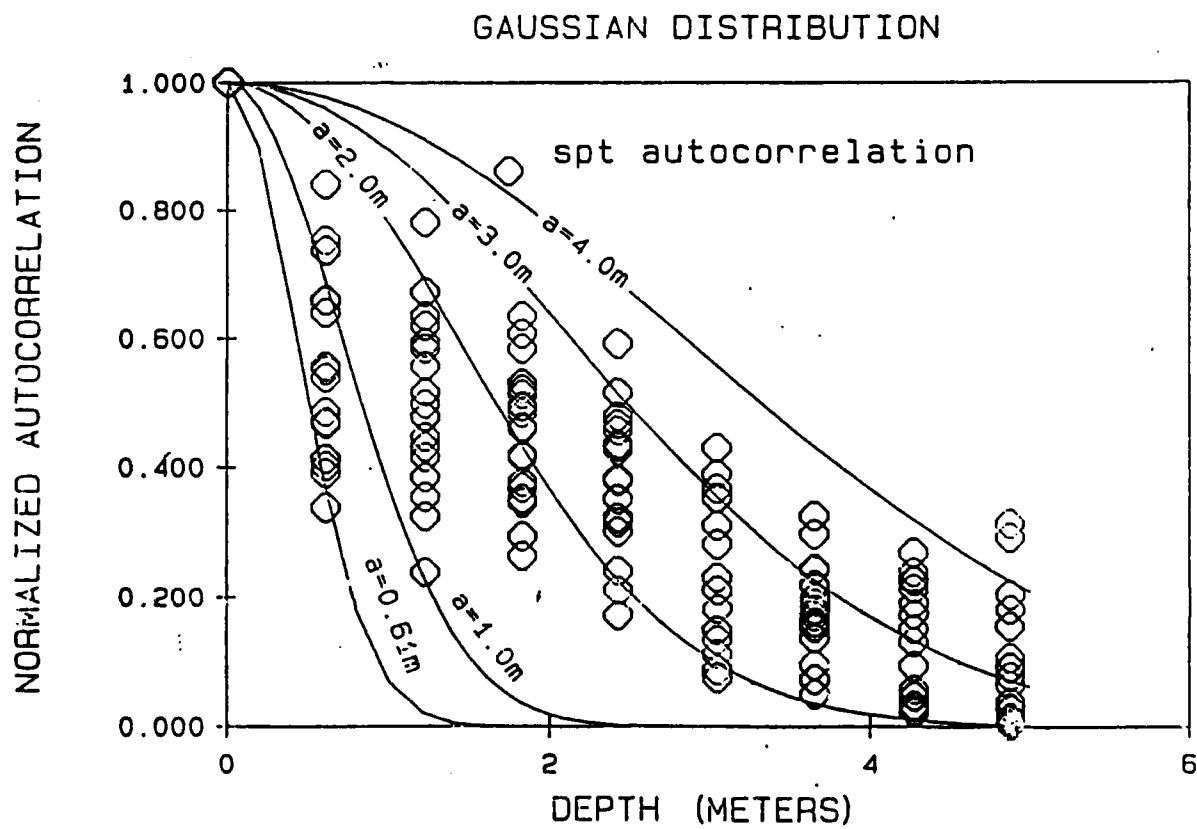
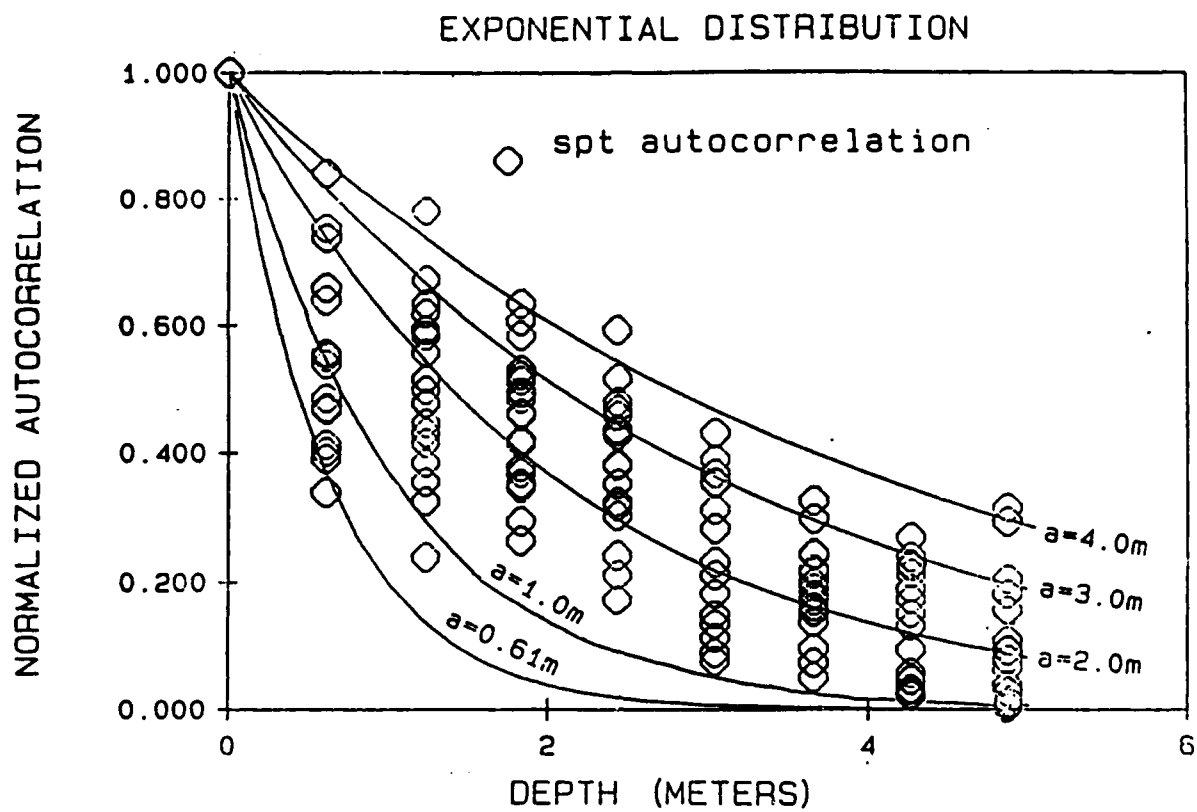


Figure 17.

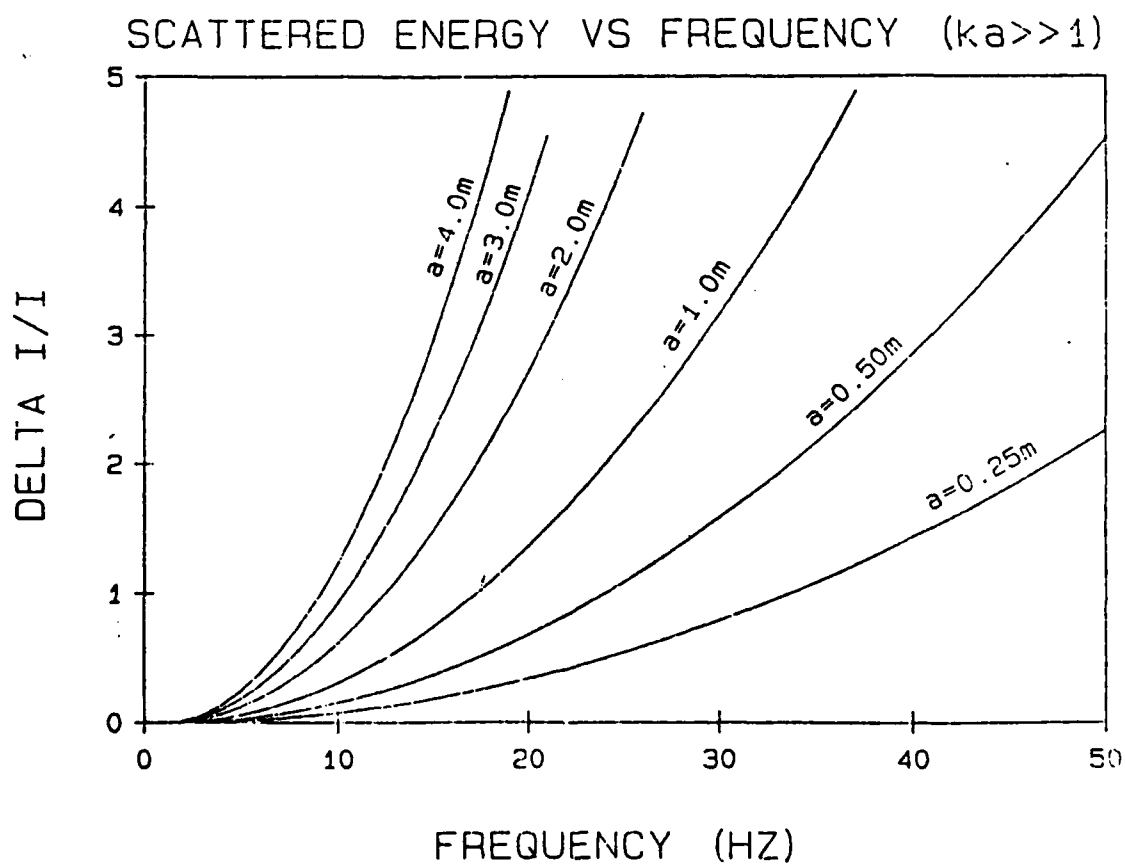
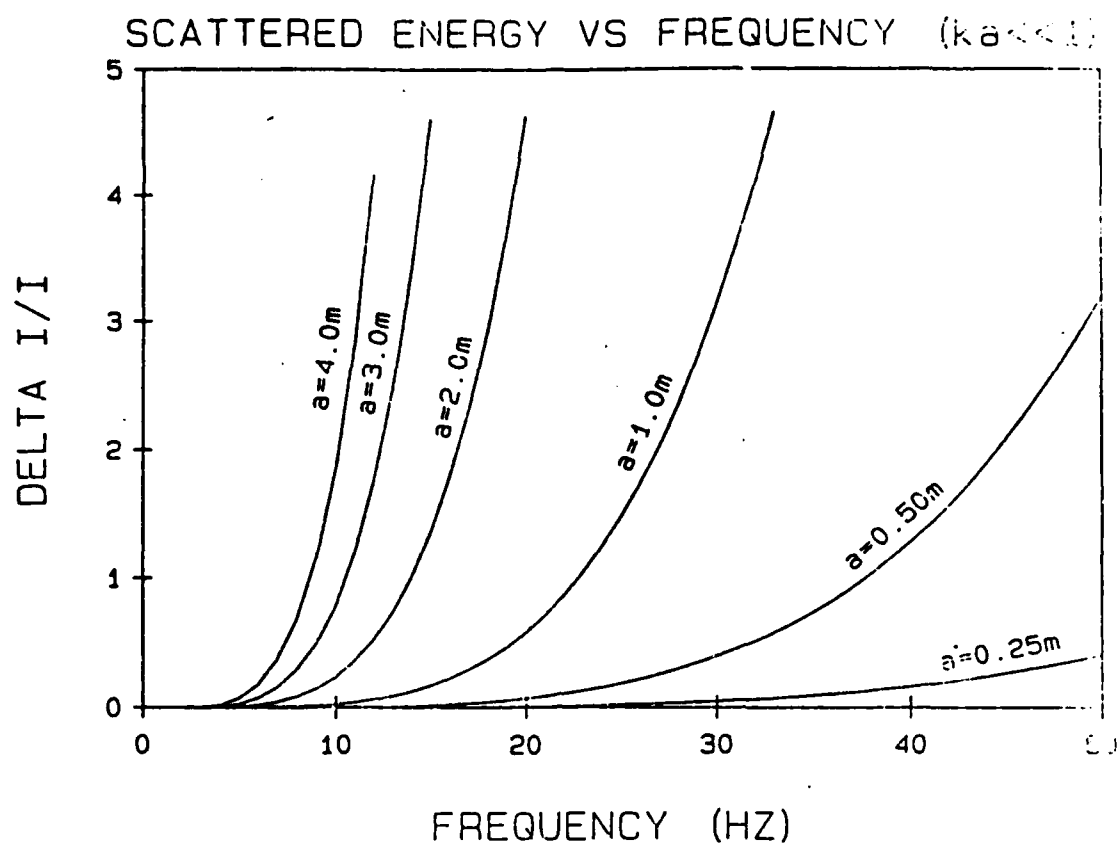


Figure 18.

**EXPERIMENTAL CONFIRMATION OF
SUPERPOSITION FROM SMALL SCALE EXPLOSIONS**

Brian W Stump
Southern Methodist University
Department of Geological Sciences
Dallas, Texas 75275

Robert E Reinke
Air Force Weapons Laboratory/NTESC
Kirtland AFB, New Mexico 87117-6008

ABSTRACT

An in situ experimental program in alluvium is implemented and analyzed to test linear superposition. After separating stochastic and deterministic propagation path effects, direct superposition is experimentally validated at 20m for two 5 lbs charges spaced as close as 2 m in alluvium. The charges are separated by the scaled range of $147 \text{ m/kt}^{1/3}$ and observed at the scaled range of $1470 \text{ m/kt}^{1/3}$. Finite spatial source effects are observed and modeled in the plane passing through two charges separated by 2 to 10 m. The deterministic single burst waveforms are used to model the multiple burst data. The effects observed and modeled include direct superposition below the corner frequency, shift to lower corner frequency with increasing charge separation, and spectral scalloping. For charges closely spaced (up to 4 m, observed at 20 and 24 m) the primary effect on the waveform is replicated by a constant delay time between two identical waveforms. For charges spaced by 10 m (observed at 20 and 30 m) the effects of propagation path differences must be included. These effects result in smoothed spectra.

AD-A181 092

DETERMINISTIC AND STOCHASTIC WAVEFIELD IN THE
NEAR-FIELD FROM EXPLOSIVE S... (U) SOUTHERN METHODIST
UNIV DALLAS TX DEPT OF GEOLOGICAL SCIENCES...
B W STUMP ET AL. 03 APR 87 SMUG-3

3/3

UNCLASSIFIED

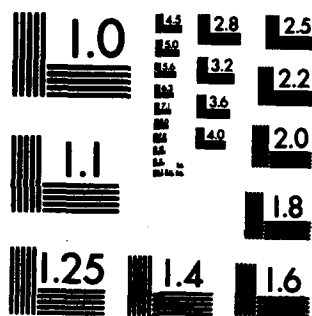
F/G 8/11

NL

[REDACTED]

[REDACTED]

[REDACTED]



MICROCOPY RESOLUTION TEST CHART
NATIONAL BUREAU OF STANDARDS-1963-A

INTRODUCTION

The effect of finite sources on radiated wavefields has received considerable attention from the earthquake source community. Such work has increased the understanding of source phenomenology while improving the ability to estimate ground motions from broad classes of earthquake sources. Finite explosive array effects have received far less attention within the seismological literature.

The primary focus of this study is the investigation of finite spatial source effects from chemical explosions. In particular, the interaction of deterministic and stochastic wave propagation with the source characterization problem will be discussed. Evidence supporting linear superposition will be shown. The assumption of linear superposition leads to a predictive capability.

Spatial arrays of chemical explosions are used in a number of different fields. The mining industry uses arrays of explosives in both open pit and subsurface excavation. The spatial distribution of charges and timing of their detonation are used to control the extent of material excavated, the size of the rubble, and the far-field ground

(motion levels (Winzer, S. R., 1978; Bergman et al, 1974; Hagan and Just, 1974). The majority of work in this area has dealt with laboratory and field data resulting in the development of practical relationships for explosive array design (Winzer et al, 1980; Winzer et al, 1981; Anderson et al, 1982). Little theoretical work or numerical modeling of these effects has been completed. This type of investigation has not been necessary since the properly scaled experiments in the materials of interest can be conducted.

(The second area where arrays of explosives are employed is in the simulation of ground motions from earthquakes (Higgins et al, 1978 and Bleisweis et al, 1973). Although data from natural events are available, the recurrence interval of great earthquakes has retarded the development of adequate natural data sets. Where site specific data are required and the historical data base is absent, explosive simulation of earthquake environments may help refine loads on engineering structures.

O Since the onset of the above ground test ban treaty, the utilization of high explosive arrays in simulating ground motion environments from nuclear explosions has been the only way to exercise engineering structures (Cooper, 1970). These studies have focused upon regions where the stress-strain relations are apparently nonlinear. The spatial and

temporal dimensions of the source are adjusted to produce motion environments with prescribed amplitudes and pulse widths.

In each of the three previous applications of explosive arrays, the focus has been upon the near-source wave field. The radiated energy from these explosive arrays in the far-field is of interest to the community responsible for discriminating earthquakes from explosions. In the advent of a comprehensive test ban treaty, one would have to be able to discriminate between a mining blast which might be as large as several hundred thousand pounds of explosives and a low-yield nuclear explosion. Quantification of the effects of arrays of chemical explosions may aid in this discrimination. Preliminary work in this area has been completed by Greenhalgh (1980). A complete understanding of the problem relies upon relating the near-source models and data to the far-field environment.

The investigation of superposition from in situ experiments is of interest as it relates to the intermediate stress level response of the media. The distance at which the transition from linear to nonlinear response occurs has been questioned by a number of investigators (Trullio, 1978; Larson, 1982; Minster and Day, 1986). Larson (1982) reports that linear superposition holds in the plane of symmetry

from two small charges in salt in the laboratory (range of $168 \text{ m/kt}^{2/3}$).

The approach to finite explosive arrays reported here relies on a characterization of the single burst ground motion. The specific quantification used is from Reinke and Stump (1987) referred to as Paper I. In that work the single burst is experimentally quantified with consideration given to source symmetry, propagation path, and scattering. The wave field is experimentally divided into a deterministic and stochastic component with the deterministic component utilized in predictions. Practically, the single burst quantification is completed in both the time and frequency domains yielding mean and variance estimates.

The single burst source quantification will be used to test for linear superposition with multiple burst experimental data. This model will also be used to explore finite spatial source effects in the observational data base.

EXPERIMENTAL DESIGN AND IMPLEMENTATION

Each experiment discussed in this report is summarized in Figure 1. The 5 lbs charges were placed in 1.22 m holes with a diameter of 0.15m. Charges were placed at the bottom of the hole. The holes were then backfilled with sand.

Force-balance accelerometers were used as sensors. The three components (housed in a single case) were oriented in the radial (positive away), transverse (positive clockwise), and vertical (positive up) directions with respect to the source. The case was buried in the alluvium so that its top was flush with the free surface. Paper I reports the good coherence between 1 and 70 hz observed when all instruments were placed side-by-side in a huddle test. The accelerometer outputs were passed through a 12-bit analog to digital converter in the field and recorded on cassette tape with a sample rate of 200 samples per second. A five pole antialias filter was palced at 70 hz.

The test site was chosen for its apparent homogeneity and consisted of dry alluvium. Further discussion of its properties are given in Paper I.

As reported in Paper I, a number of single burst experiments were conducted to characterize the source and media with offsets between 10 and 30 m. The finite source data focused upon the two explosion case since this data can be used to constrain the basic characteristics of source interaction. As Figure 1 illustrates, charge separation was varied between 2 and 10 m at 2 m increments. The proximity of the charges to the free surface (1.22 m) resulted in significant venting to the free surface at detonation and the formation of craters. Ground motion from the airblast arrival was not perceptible in the data due to the 1.22 m source burial depth. Crater diameters are given as the solid lines bounding the charge locations in Figure 1 and were typically near 2 m. ARTS 3 produced a single elongated crater since the lateral charge separation was only 2 m.

Gauge arrays for the two explosion tests can be separated into two categories. The first set of gauges (primary-P or center-C) were placed at right angles to the plane passing through the charges. These gauge lines intersected either the midpoint between the two charges (C) or one of the charges (P) and were emplaced to check direct superposition. The second set of gauges (secondary-S) were placed in the plane of the charges and thus the effects of source finiteness were maximized by the travel path and time differences between the two sources (Figure 1).

SUMMARY OF SINGLE BURST CHARACTERIZATION

In order to check linear superposition and quantify the effects of spatial finiteness, the single explosion source and wave propagation to a variety of distances must be quantified. ARTS 2 in Figure 1 is one such test designed to quantify the single source and propagation. A complete discussion of the single source is given in Paper I. The time domain records from ARTS 2 are given in Figure 2. When the records are low pass filtered at 30 hz they appear identical to one another. The high pass filtered records show significant variation above 40 hz. A variety of tests were conducted and reported in Paper I to quantify the cause of these high frequency amplitude variations. Strong evidence supported scattering within the geological media as the cause of this variation.

This realization led to the calculation of mean and variance estimates for the waveforms from a single explosion. Figure 3 is the mean ± 1 standard deviation spectra for the 20 m range from the single burst. Figure 4 is a similar representation but in the time domain.

() The ensemble estimates for the spectra show small variances between 3 and 35 hz for the 20 m range. Beyond this 'coherent frequency' the scatter with azimuth in the data becomes large as exemplified in the band pass seismograms of Figure 2. The 20 m data exhibit 8 db scatter at 40 hz.

As reported in Paper I, a series of tests were conducted to separate the effects of gauges, gauge placement, source asymmetry, and propagation path on the high frequency data. The variation in the data was attributed to the geological media. Therefore, the deterministic part of the wavefield is defined as the azimuthally symmetric data below 35 hz.

SUPERPOSITION

The single burst ensemble spectral estimates are used to check the applicability of linear superposition by direct comparison to the multiple burst data from ARTS 3 and 7 (Figure 1). The first quantification of these effects considers the case where each source is equidistant from the charge, thus time delays between the two sources are nonexistent. The primary (P) and center (C) gauge lines are used to check for superposition. Comparisons between the ensemble estimates and the data will be reported only for the 20 m range. Similar conclusions follow from the analysis of data at the 30 m range.

Based upon the 3-35 hz coherent bandwidth from the 20 m ensemble estimates, this frequency band is chosen to check superposition. The criterion chosen to test for superposition is that the multiple burst data fall within ± 1 standard deviation of the ensemble estimate of the multiple burst environment. Since the stochastic component of the wave field leads to large variances beyond 35 hz, the criterion is not robust beyond this frequency. Within the coherent bandwidth the ± 1 standard deviation bounds are 3-4 db for the Z component and 4-5 db for the R component. The

variability in the geological structure limits checks on superposition to within these bounds when in situ measurements are made.

The 20 m ensemble estimate of the superposed spectra with variances is compared to the P and C gauges for ARTS 3 and 7 in Figure 5. The vertical observational data compares well with the superposed spectra between 3-35 hz. Comparison of the predicted spectra with the observations from ARTS 4 (Figure 1) led to similar conclusions. Each test bed was displaced approximately 30 m from the previous test so that between ARTS 2 (used to make single source ensemble estimates) and ARTS 7 the test bed was displaced by 150 m. Subtle changes in the geology over these scale lengths may explain the systematic changes in the multiple burst spectra.

The conclusion to be drawn from this analysis is that within the variance of the multiple source estimate, superposition holds for 5 lbs charges 20 m from the receiver over the frequency band 3-35 hz. This includes two charges spaced as close as 2 m where individual craters overlap. Larson (1982) reports superposition in laboratory salt validated for two charges separated by $168 \text{ m/kt}^{1/3}$ from the observer. In these in situ results superposition is validated within the data scatter (3-35 hz) for two charges separated by $147 \text{ m/kt}^{1/3}$ at an observation range of $1470 \text{ m/kt}^{1/3}$.

These results can be compared qualitatively with the reduced displacement potential (RDP) predicted from the Mueller-Murphy (1971) scaling relation. Figure 6 gives the RDP for 5 and 10 lbs explosions respectively. The source corner frequency is between 6 and 9 hz remarkably close to what one would estimate from the acceleration spectra (Figures 3 and 4). The model predicts that below the corner that a single charge of 10 lbs will nearly match twice the 5 lbs result. Above the corner frequency, the single 10 lbs charge will not reach twice the 5 lbs result. The critical region in the data for testing superposition falls between 10 and 35 hz at the 20 m range. The exact location of this band is subject to some error since the Mueller-Murphy (1971) scaling relations were developed for nuclear sources of much greater yields. The critical point is that the principle region of interest for checking superposition is beyond the source corner. The experimental results in Figure 5 support strict superposition well beyond the source corner with an apparent corner frequency shift.

RESOLUTION OF SPATIAL FINITENESS

In an attempt to characterize the finite spatial effects of the multiburst environment, synthetics are compared to data recorded in the plane of the linear array of sources (Figure 1, secondary lines). The predictions are made using mean seismograms constructed from data such as that generated in the ARTS 2 experiment (Figure 4).

These mean seismograms are computed by time aligning the direct P wave from each observation and then computing a mean. The 20 m seismogram from the ARTS 2 experiment along with its ± 1 standard deviation bound is given in Figure 4. The mean radial and vertical accelerograms show little scatter while the transverse component has standard deviations comparable to the mean. This observation is in agreement with the coherent nature of the radial and vertical motions between 3 and 35 hz and the large scatter for all frequencies of the transverse motion. Since the deterministic component of the wave field is of primary interest in the superposition study, the transverse motion will not be considered.

When two sources are displaced from a receiver at different distances, the following effects occur: (1) A change in arrival time of the radiated energy for one source relative to the other; and (2) A change in the waveform shape since one contribution has traveled a greater distance than the other. If the receiver to charge separation is large relative to the spacing of the two charges, one may neglect the change in wave shape for the two charges. This case is investigated first by superposing the mean seismograms from Figure 4 with an appropriate delay time for charge separation. The delay time becomes:

$$T_D = X_{12}/V$$

where X_{12} is the difference in length of the two propagation paths and v is the velocity of the media. The material at the test site has typical near surface velocities ranging from 244 to 366 m/s. These values, coupled with charge separation of 2 to 10 m, led to consideration of time delays of 5 to 40 ms. The time domain results of this delay and sum procedure are given in Figure 7. Qualitative analysis of these results show constructive interference for the direct arriving body waves for short delay times (5 ms) with destructive interference leading to complex waveforms for delays between 15 and 30 ms. For delay times greater than 30 ms one can observe the individual body waves from the two sources. The surface waves (which arrive at 200 ms) show a gradual decay in amplitude over all delay times. The 40 ms

delay yields a peak amplitude which is 60% that of the 5 ms delay. When the delay times between the two sources are small compared to the single burst pulse width, constructive interference occurs while complex waveforms with reduced amplitudes are predicted for delay times comparable to the pulse width from the single source. Amplitude changes as a function of delay time for these synthetics are summarized in Figure 8.

The frequency domain representation of the superposed waveforms more explicitly exhibits the constructive-destructive interference. The superposed acceleration spectra are compared against the single burst mean observation in Figure 9. As quantified by Pilant and Knopoff (1964), spectral modulation is given by:

$$\cos(\omega t_D/2)$$

where ω is the angular frequency of interest.

Four qualitative observations of the multiburst spectra are made: (1) The low frequency level of all spectra are identical reflecting constructive superposition; (2) The point that the spectra diverge from the long period level occurs at lower frequencies with increasing time delays (arrows in Figure 9); (3) Large spectral holes are observed as predicted with the frequency domain spacing decreasing

(with increasing time delay between sources; and, (4) A return to constructive interference occurs between holes.

These results assume no change in the Green's functions or propagation path effects as the charge separation increases. The validity of this assumption can be checked against the multiburst observational data (Figure 1). The secondary gauge lines in the plane of the charge array yield the necessary data.

(The primary, secondary, and A2MEAN (superposed single burst) acceleration spectra for ARTS 4 (4 m separation) at 20 m range and ARTS 7 (10 m separation) at 20 m range are given in Figures 10a and 10b. As noted in the superposition discussion, the primary gauge and A2MEAN prediction overlay one another between 3 and 35 hz. The effect of charge separation is maximized for the secondary gauges. For ARTS 4 the two charges are 20 and 24 m from the gauge. For ARTS 7 the two charges are 20 and 30 m from the gauge. The spectral scalloping already noted in the synthetics is well defined for ARTS 4 while reduced in scope for ARTS 7. The overall amplitudes for the secondary gauges are reduced throughout the bandwidth for both experiments.

O The secondary gauge data for ARTS 4 and prediction utilizing the 20 m mean data (15 ms delay) is given in Figure 11. The prediction closely replicates the observational data

including the large spectral hole at 32 Hz. The 15 ms delay time represents a propagation velocity of 266 m/s between the two closely spaced charges. This velocity is near the surface wave velocity suggesting the surface wave contribution is dominant. Over these close ranges the Green's functions change slowly and the primary effect on the superposed waveforms is a time delay.

For event 7, the twenty meter secondary observation is 20 and 30 m from the two charges. The change in propagation path effects for the 20 and 30 m ranges were dramatic enough that successful prediction required the use of mean seismograms from single bursts observed at 20 and 30 m respectively. The 30 m mean seismogram was calculated in the same manner as that for the 20 m given in Figure 4. Figure 12 displays the prediction and observation for event 7. The spectral nulls are more closely spaced than in the ARTS 4 data, representative of the 25 ms arrival time difference. Due to the change in propagation path between the two sources, the spectral nulls are not as pronounced as those observed when two identical waveforms are superposed (Figure 10).

There are three propagation effects which lead to the necessity of including mean seismograms from each of the two sources in ARTS 7: (1) A change in $t_a - t_s$ time; (2) Geometrical spreading effects; and (3) Attenuation. A

simple analysis of these effects can explain the success of the ARTS 4 superposition using the 20 m mean seismograms and the failure of ARTS 7 utilizing only the 20 m waveforms. Taking the near surface velocities as $V_p = 366$ m/s, $V_s = 244$ m/s (Stump and Reinke, 1982) the $t_s - t_p$ time differences are 0.005 s for ARTS 4 and 0.014s for ARTS 7. The 0.005 s change is one sample interval in the observational data and corresponds to a 31° phase shift at 17 Hz and a 63° phase shift at 35 Hz. For ARTS 7 the phase shift is 86° at 17 Hz and 176° at 35 Hz. The phase shifts for ARTS 7 are dramatic enough to jeopardize the single waveform superposition procedure. At higher frequencies the ARTS 4 results should also deteriorate.

Geometrical spreading will lead to amplitude differences from the two sources which are not accounted for in the single seismogram superposition. Experimental determination of geometrical decay rates for this test site give $r^{-1.6}$ for the body waves and $r^{-0.8}$ for the surface waves (Stump, 1983). For ARTS 4 with charges at 20 and 24 m the ratio of body wave amplitudes from the two ranges is predicted to be 0.75 while the ratio for the surface wave amplitudes is 0.93. Similar calculations for ARTS 7 give the body wave ratio as 0.54 and the surface wave ratio as 0.82. These calculations indicate that at least for the body waves the single range superposition procedure for ARTS 7 is inadequate.

Finally, the effect of attenuation must be quantified. The range of Q values for the dry alluvium environment can be bounded between 10 and 40 (Flynn, 1986). Taking the simple exponential Q model $e^{-\pi f t / Q}$, where f is the frequency and t is the shear arrival time, Table 1 was developed to quantify these effects for the 3-35 Hz band. The 24 m to 20 m ratios show only moderate Q effects even at the highest frequencies and smallest Q. The 30 m to 20 m ratios give a value of 0.63 for Q=10 and f=35 Hz. Although Q effects are less dramatic than the phase shifts and geometrical spreading terms, they may become significant for ARTS 7.

CONCLUSION

The series of small scale explosive experiments tested the applicability of linear superposition in the near-field. The study has shown that one must separate stochastic and deterministic propagation path effects from the single burst wave field prior to testing for superposition. Once this process has been completed (Paper I), then superposition is verified as the two burst wave fields fall within ± 1 standard deviation of the ensemble estimate (3-35 hz). Thus superposition is supported for two, five lbs charges spaced as close as 2 m ($147 \text{ m/kt}^{1/2}$). Comparison with the Mueller-Murphy source function for five and ten pounds shows that superposition must be checked above the corner frequency.

Finite spatial source effects are experimentally quantified by recording data in the plane of the two charges. These finite effects in the near-field include: (1) A rise in long period spectral values that match direct superposition; (2) Lowering of corner frequency with increased source separation; and (3) Spectral scalloping at high frequencies. Comparison of superposed ensemble spectra (time delayed) show that when travel time differences between the two sources are the primary effects in the observed wavefield

then the observed data are replicated which include large interference holes in the spectra. As propagation path differences between the two charges result in waveform changes, the superposition procedure can be applied using separate ensemble estimates for each range. The resulting waveforms again match the observations. Interference holes that were so prevalent when only source delay time was present (ARTS 4) are not as well defined when wave shape changes due to propagation are present in the superposition (ARTS 7). These propagation effects were quantified with the change in $t_s - t_r$ from the two charges leading to large phase shifts for ARTS 7. Differences in geometrical spreading and Q for the two charges in ARTS 7 were important although not as strong.

Utilizing the principles of superposition as applied to the deterministic portion of the wavefield, a procedure has been developed which can be used to predict waveforms from arrays of explosives. This procedure assumes that the single burst environment has been characterized and may require the environment to be quantified at a number of ranges when arrival time differences, geometrical spreading differences, and attenuation differences are important. The effect of arrival time and attenuation differences increases with frequency.

References

Bergman, O. R., Wu, F. C. and Edl, J. W., 1974. Model rock blasting measures effects of delays and hole pattern on rock fragmentation, *Engineering Mining Journal* 175, 6, 124-127.

Bleisweis, 1973. Simulation of strong motion earthquake effects on structures using explosive blasts, *Nuclear Engineering and Design* 25, 126-149.

Cooper, H. F., 1970. On the simulation of ground motions produced by nuclear explosions, AFWL-WLC-TN-70-001, Air Force Weapons Laboratory, Kirtland AFB, NM.

Flynn, E. C., 1986. Effects of source depth on near source seismograms, M. S. Thesis, Southern Methodist University, Dallas, Texas.

Greenhalgh, S. A., 1980. Effect of delay shooting on the nature of P-wave seismograms, *Bull. Seism. Soc. Am.* 70, 2037-2050.

Hagan, T. N. and Just, G. D., 1974. Rock breakage by explosives: Theory, practice, and optimization, Proc. Third Int. Soc. Rock Mech. 2, 1349-1358.

Higgins, C. J., Johnson, R. L., and Triandafilidis, G. E., 1978. The simulation of earthquake-like ground motions with high explosives, Report CE-45 (78) NSF-507-1, Department of Civil Engineering, University of New Mexico, Albuquerque, New Mexico.

Larson, D. B., 1982. Inelastic wave propagation in sodium chloride, Bull. Seism. Soc. Am. 72, 2107-2130.

Minster, J. B. and S. M. Day, 1986. Decay of wave fields near an explosive source due to high-strain nonlinear attenuation, J. Geophys. Res. 91, 2113-2122.

Mueller, R. A. and J. R. Murphy, 1971. Seismic characteristics of underground nuclear detonations: Part I, seismic scaling law of underground nuclear detonations, Bull. Seism. Soc. Am. 61, 1975.

Pilant, W. L. and L. Knopoff, 1964. Observations of multiple seismic events, Bull. Seism. Soc. Am. 54, 19-39.

Reinke, R. E. and B. W. Stump, 1987. Stochastic geologic effects on near-field ground motions in alluvium, submitted Bull. Seism. Soc. Am.

Stump, B. W. and R. E. Reinke, 1982. Spall-like waveforms observed in high-explosive testing in alluvium, AFWL-TR-82-15, Air Force Weapons Laboratory, Kirtland AFB, NM

Stump, B. W., 1983. Source characterization of bermed surface bursts, Bull. Seism. Soc. Am. 73, 979-1003.

Trulio, J. G., 1978. Simple scaling and nuclear monitoring, Applied Theory, Inc. Report ATR-77-45-2, Los Angeles, California.

Winzer, S. R., 1978. The firing times of ms delay blasting caps and their effect on blasting performance, Report to the National Science Foundation, Contract DAR-77-05171. Martin Marietta Laboratories, Baltimore, Maryland.

Winzer, S. R. and A. Ritter, 1980. The role of stress waves and discontinuities in rock fragmentation: A study of fragmentation in large limestone blocks, Proc. 21st U.S. Symposium on Rock Mechanics, University of Missouri, Rolla, p. 362-370.

Winzer, S. R., D. A. Anderson, A. P. Ritter, 1981.

Application of fragmentation research to blast design:
relationships between blast design for optimum fragmentation
and frequency of resultant ground vibration, Proc. 22nd U.S.
Symposium on Rock Mechanics, MIT, Cambridge, Mass., p. 237-
241.

Figure Captions

Figure 1: Gauge layout for ARTS 2, 3, 4, 7. The solid lines indicate crater diameters. Charge placement is illustrated in the lower left hand corner.

Figure 2: The vertical acceleration records from ARTS 2. All gauges are at 20 m and azimuths range from 0° to 288°. Unfiltered, low pass filtered (30 hz), and high pass filtered (40 hz) accelerograms are given.

Figure 3: The mean (dark line) and mean ± 1 standard deviation (dotted line) spectral estimate from the 20 m records of ARTS 2. The vertical (3a), radial (3b), and transverse (3c) acceleration spectra are given.

Figure 4: The mean (solid line) and mean ± 1 standard deviation (dotted line) time domain estimates for ARTS 2.

Figure 5a: Predicted and observed acceleration spectra for ARTS 3 with 5 lbs charges separated by 2 m.

Figure 5b: Predicted and observed acceleration spectra for ARTS 7 with 5 lbs charges separated by 10 m.

Figure 6: The displacement spectra from a Mueller-Murphy source model for 5 and 10 lbs of explosive.

Figure 7: Vertical accelerations from two explosions using the time domain mean seismogram from ARTS 2 and summing with an identical record delayed in time between 5 and 40 ms.

Figure 8: Peak amplitudes of the superposed seismograms given in Figure 7 plotted against delay time between the two sources.

Figure 9: The spectral estimates of the superposed accelerations given in Figure 7.

Figure 10: The primary (P), secondary (S) observations and predicted superposition (A2mean) for ARTS 4 (a) and ARTS 7 (b).

Figure 11: The predicted superposition spectra for two charges at 20 and 24 m (ARTS 4 - secondary) compared to the data and superposition with no delay time (mean).

Figure 12: The predicted superposition spectra for two charges at 20 and 30 m (ARTS 7 - secondary) compared to data and superposition with no delay time or propagation differences (mean).

EXPERIMENTAL LAYOUT

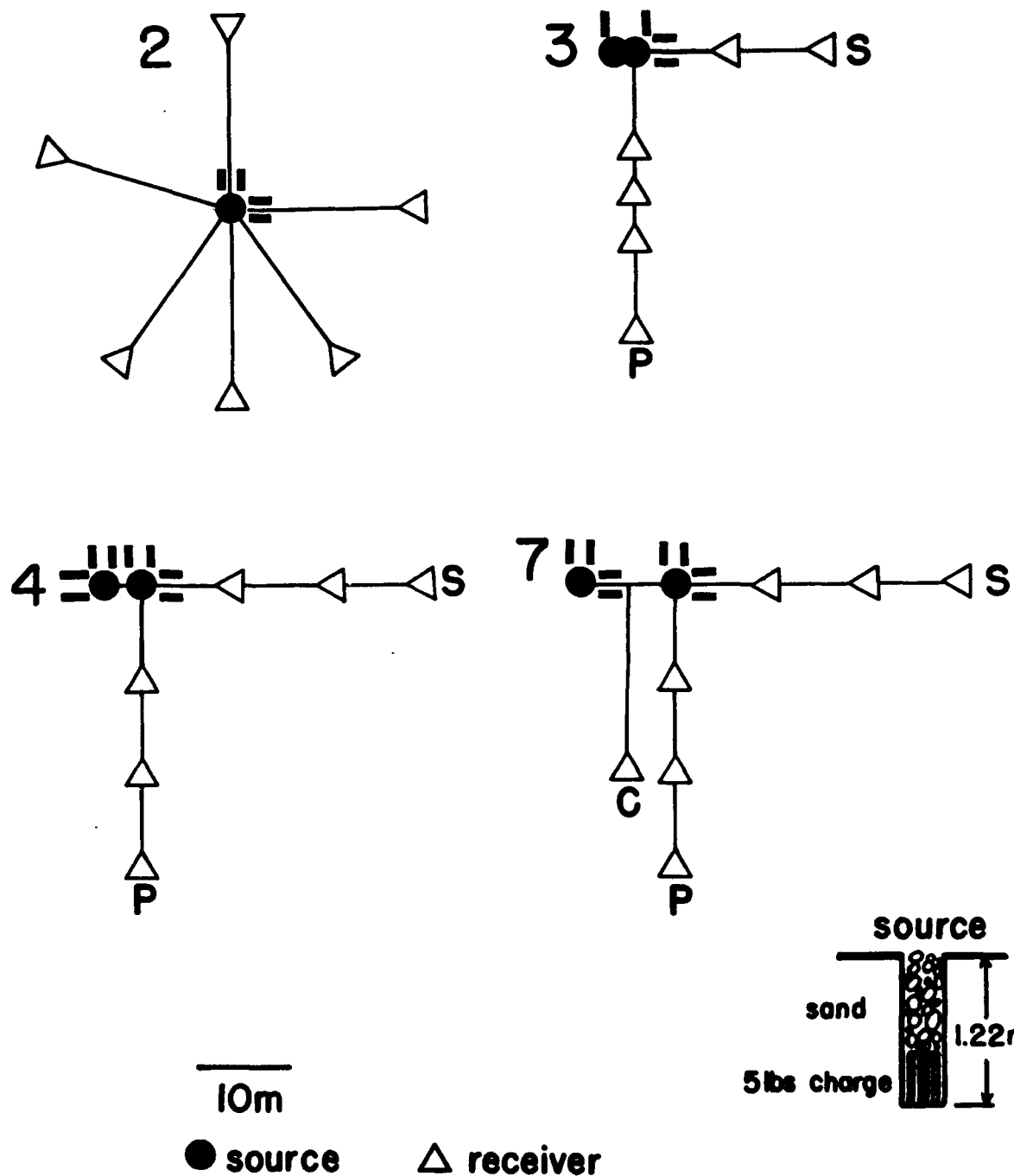
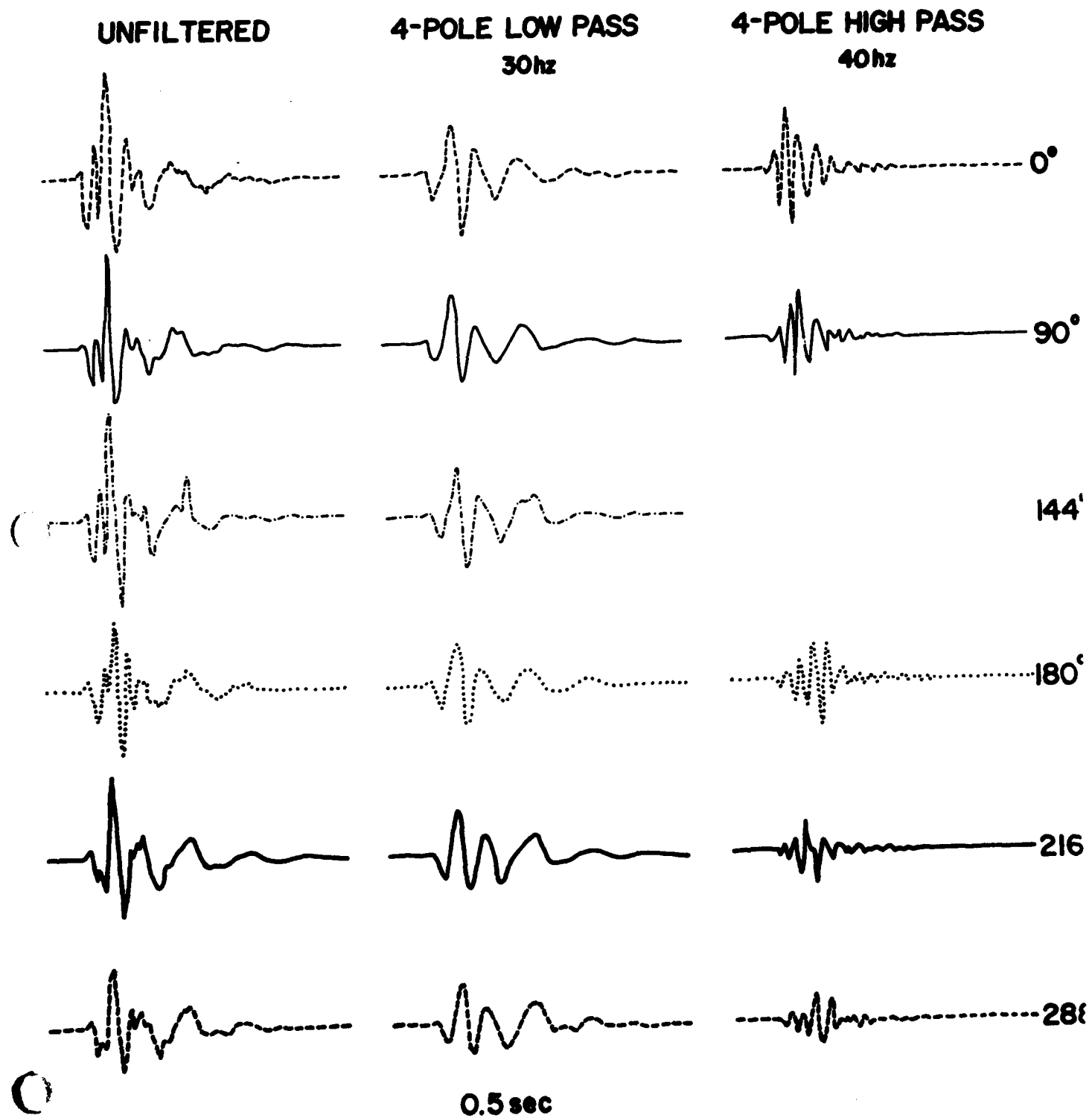


Figure 1.

ARTS 2 VERTICAL (ACC)

C



O

Figure 2.

ART 2 SCATTER Z

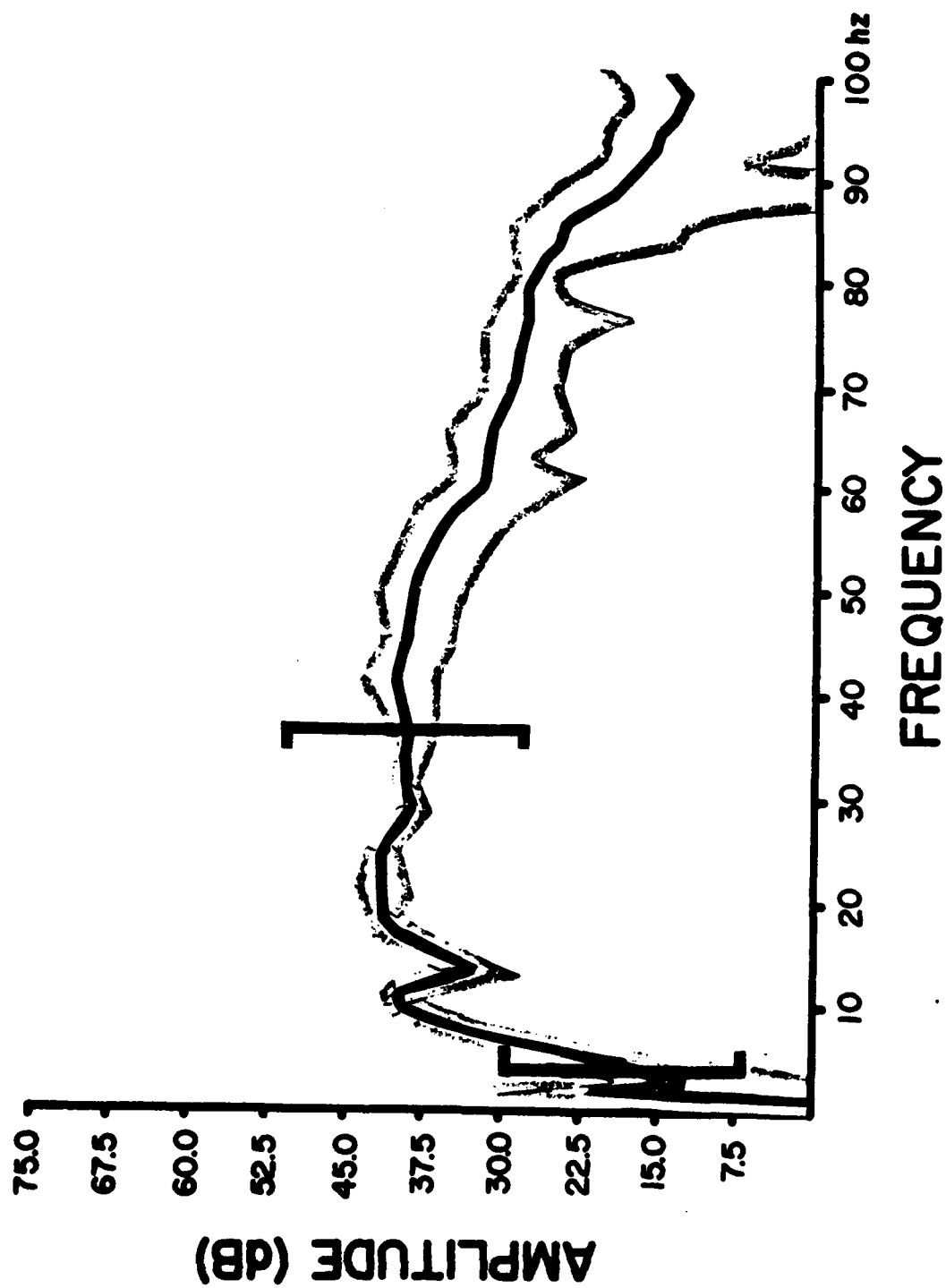
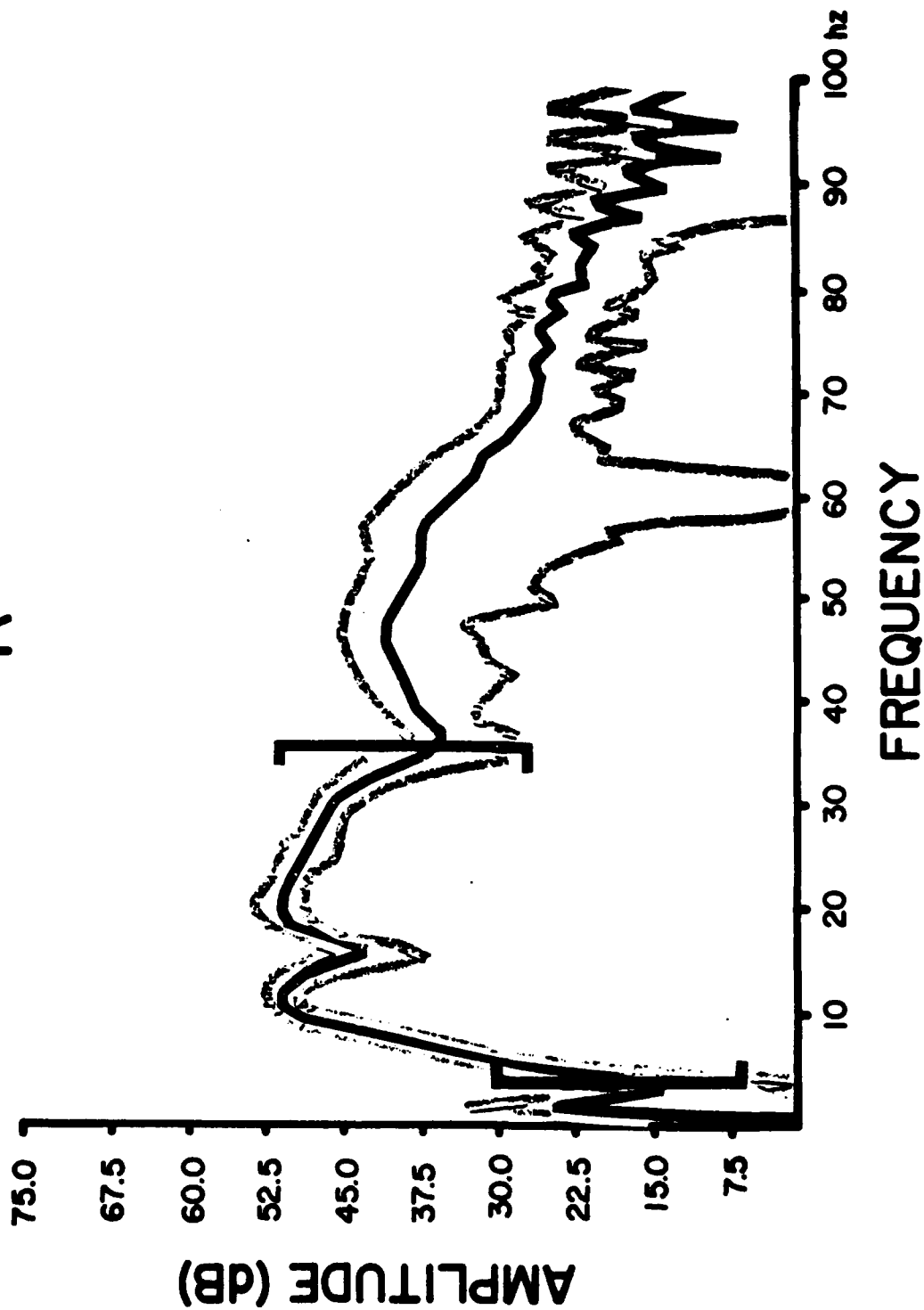


Figure 3a

ART 2 SCATTER R



Figure

ART 2 SCATTER

T

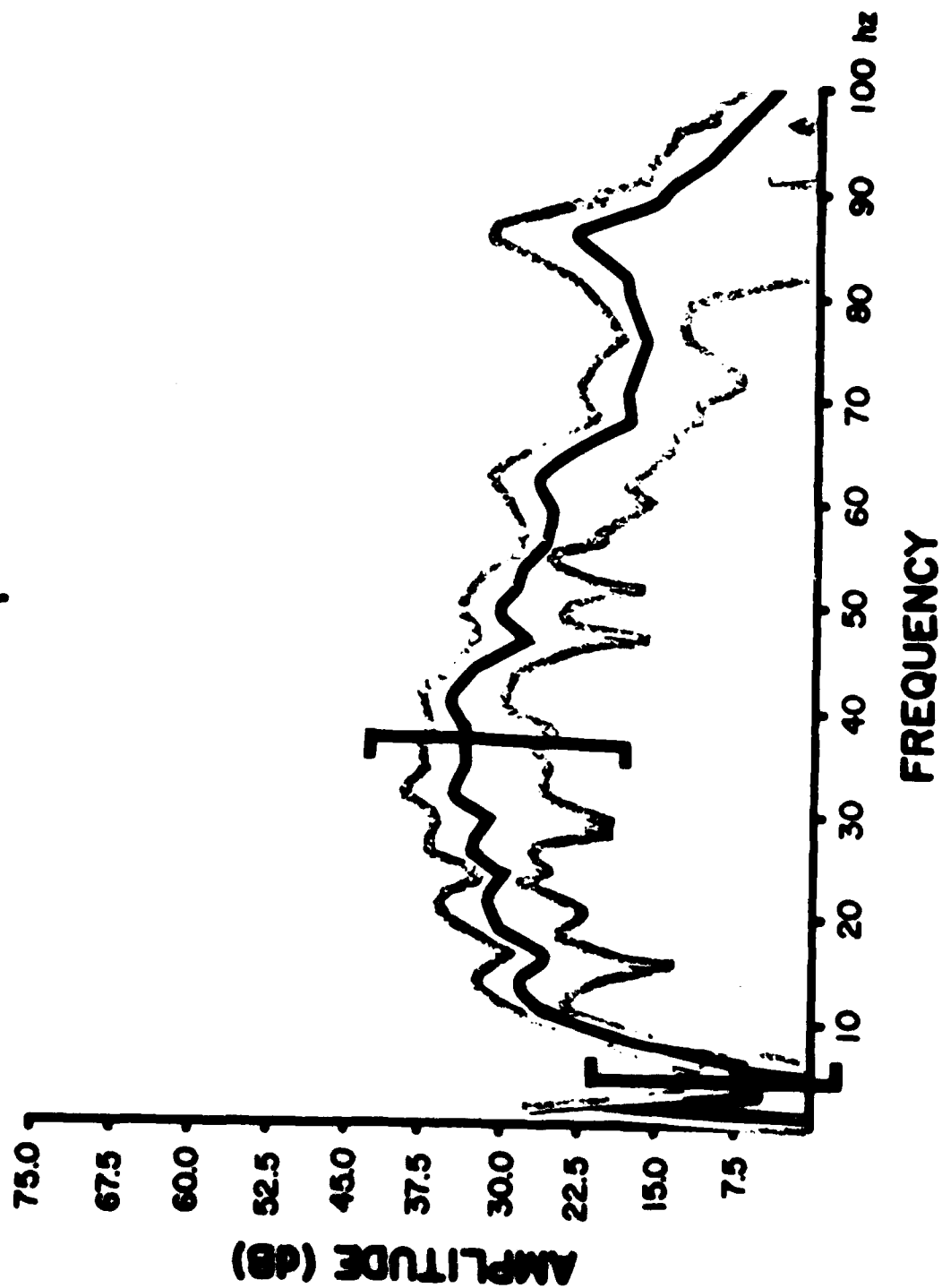


Figure 3c

ARTS 2

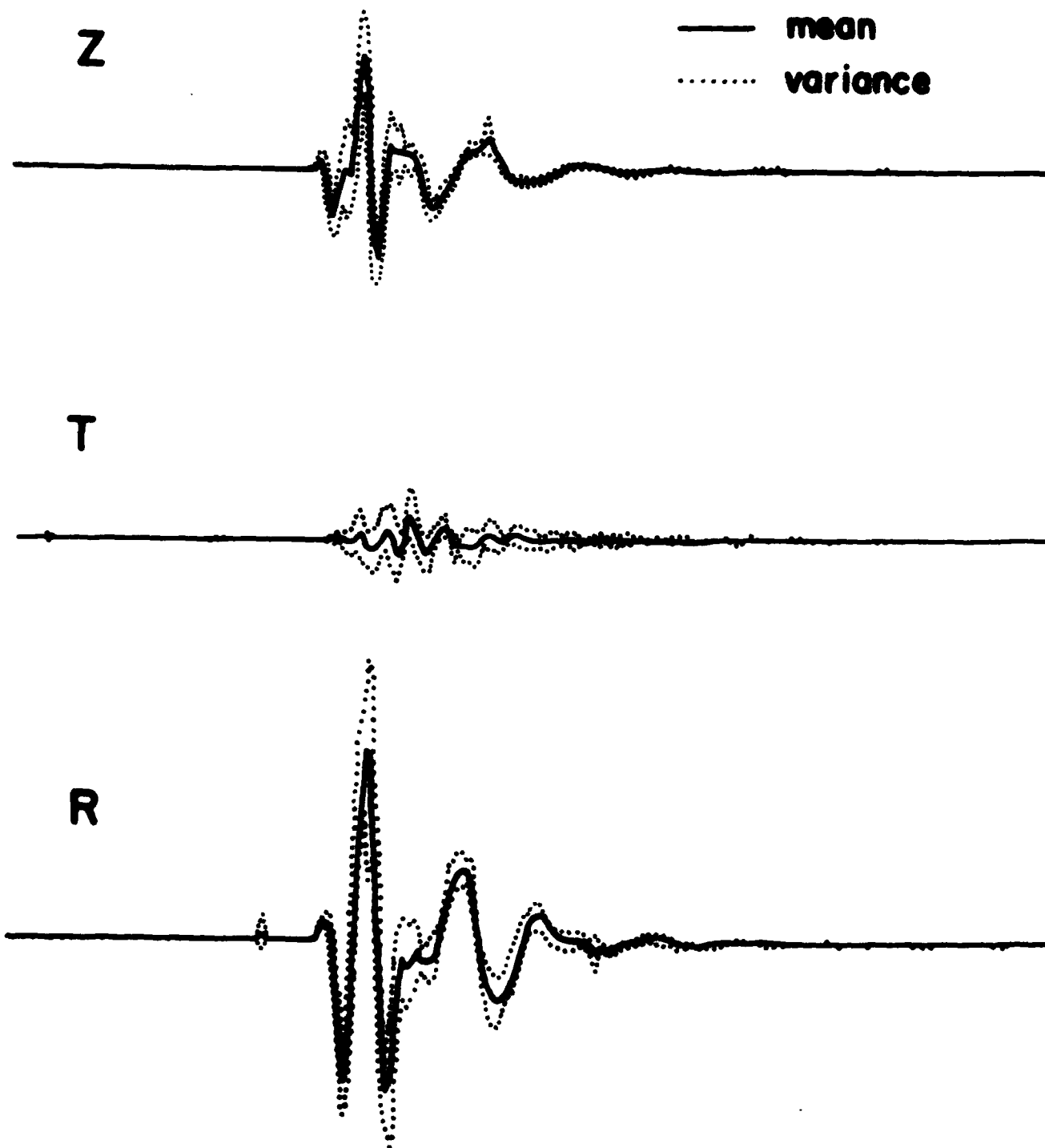


Figure 4

VERTICAL 3-20

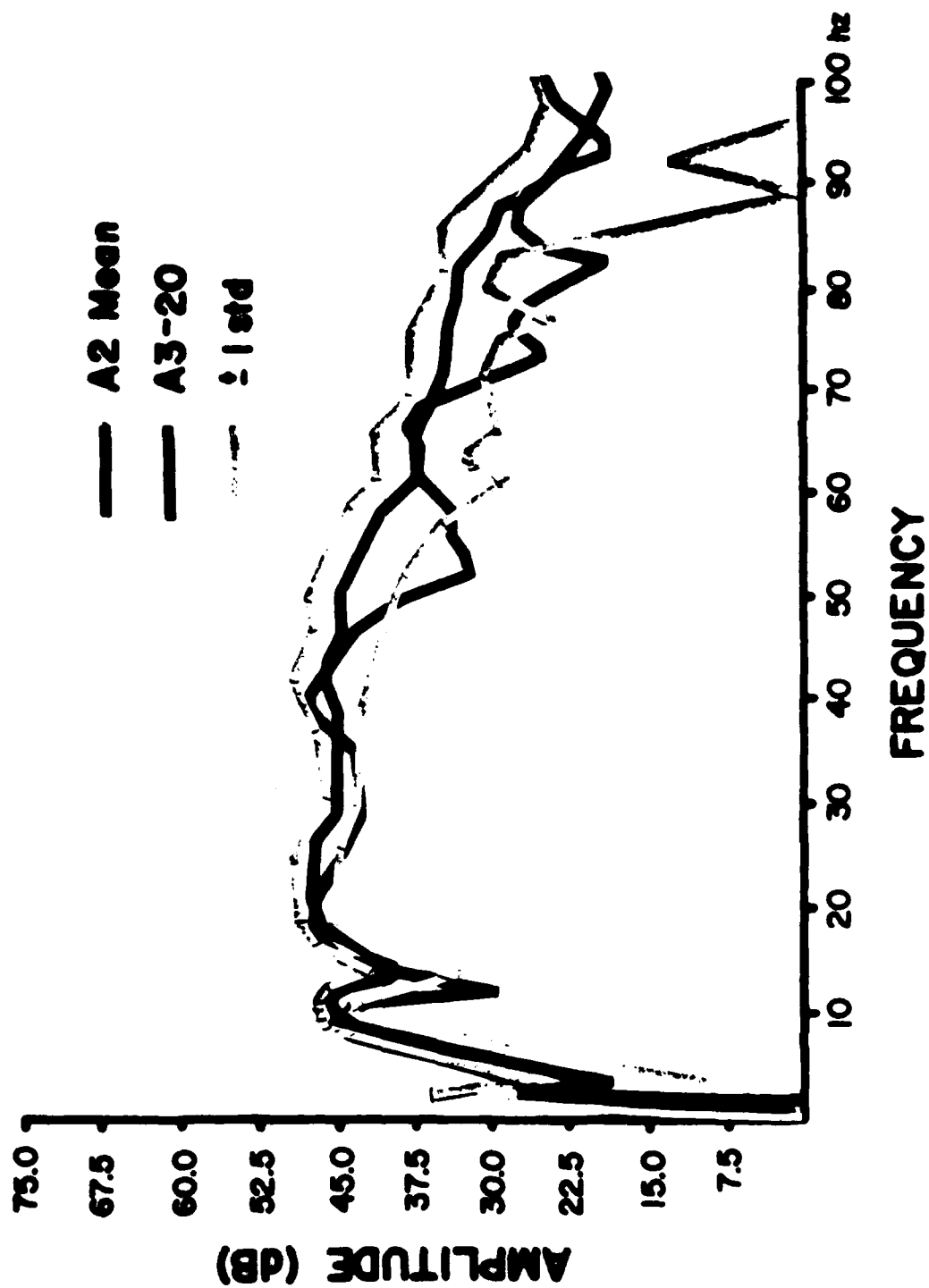


Figure 5a

VERTICAL 7-20

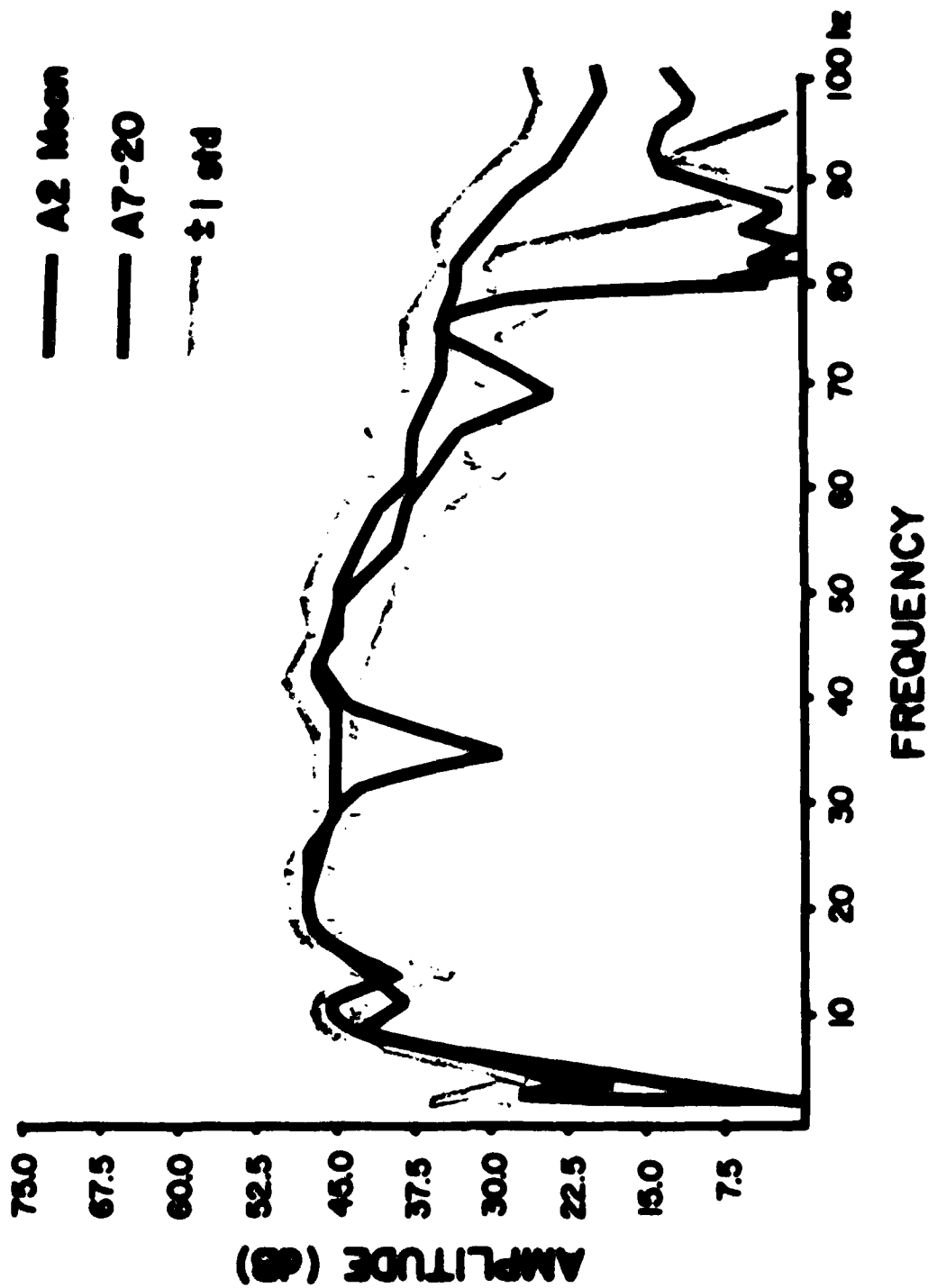


Figure 5b

MUELLER - J. J. J. SOURCE

depth = 1 m

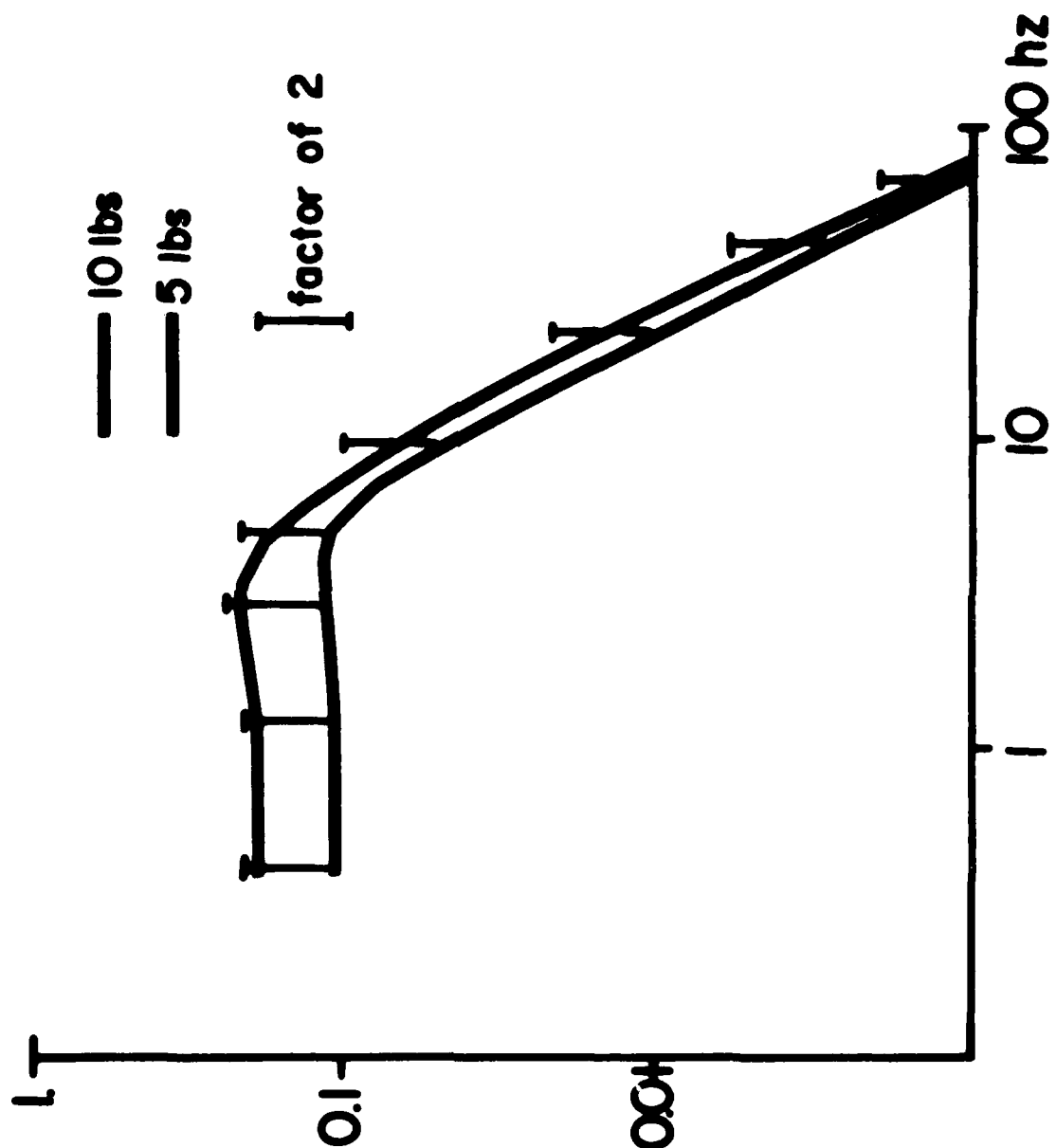


Figure 6

SUPERPOSITION VERTICAL

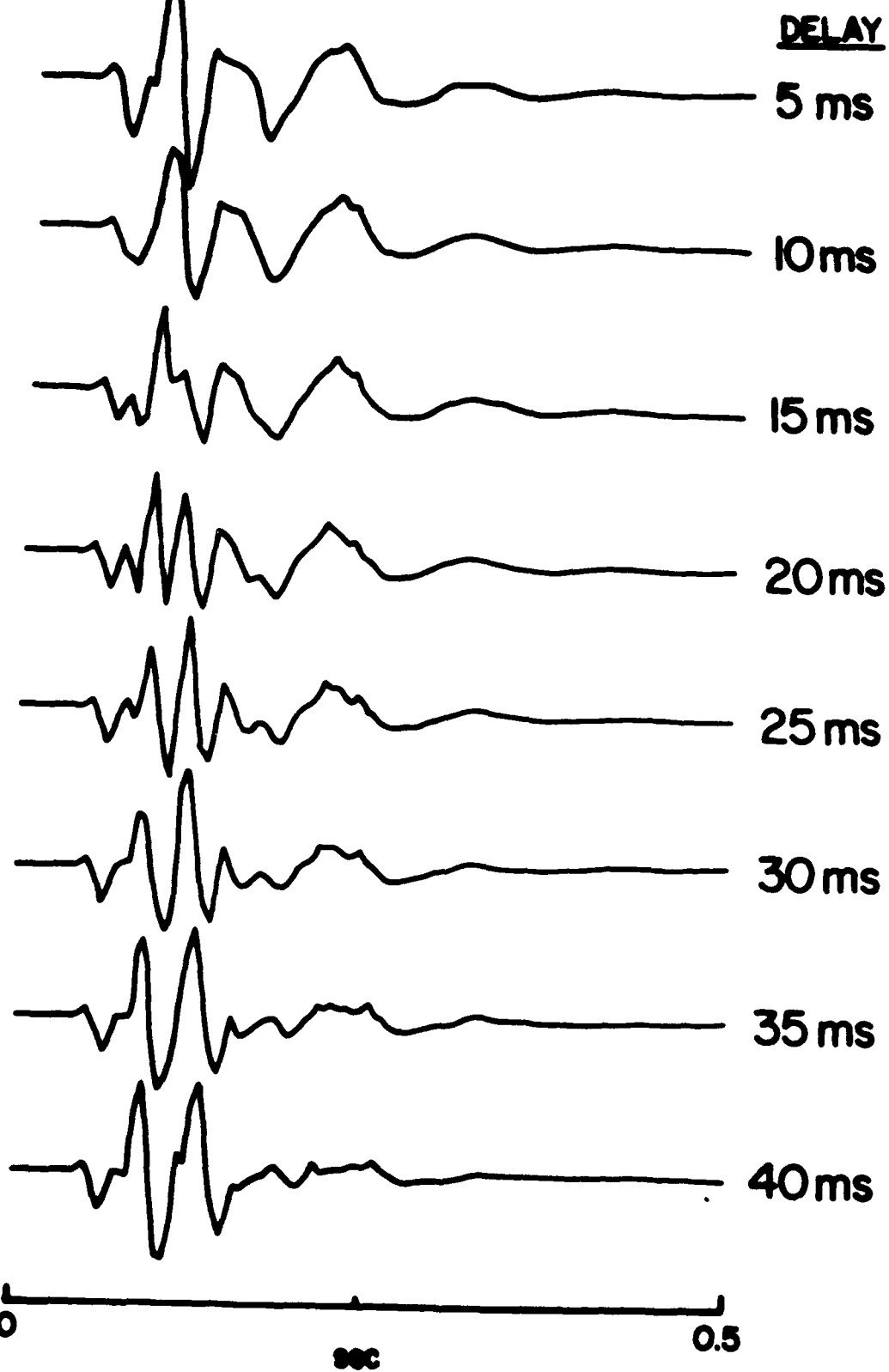


Figure 7

SUPERPOSITION PEAK AMPLITUDES

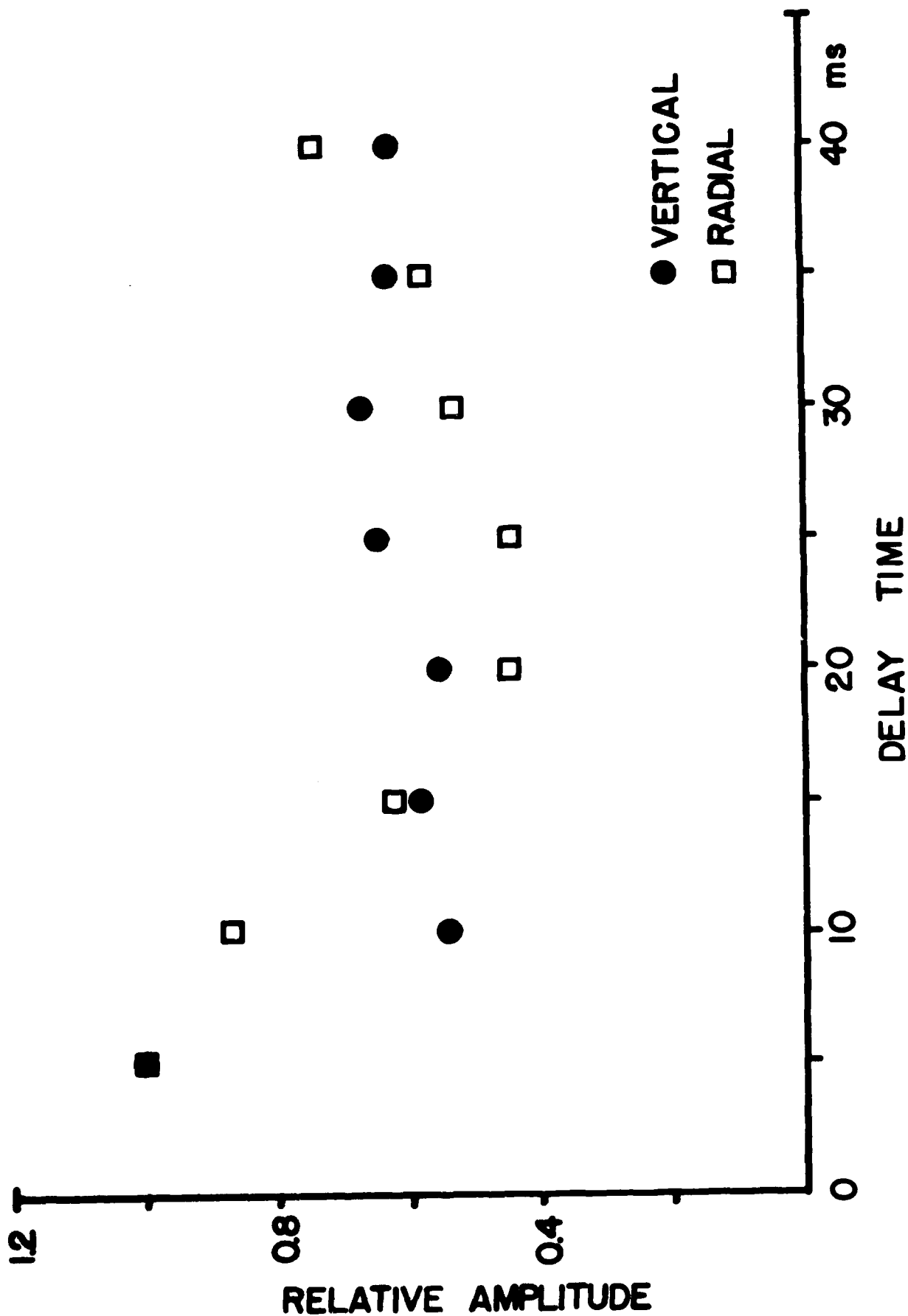


Figure 8.

SUPERPOSITION 20m Z

— MEAN (I)
 - - - 10 ms
 20 ms
 — 30 ms
 + + + + 40 ms

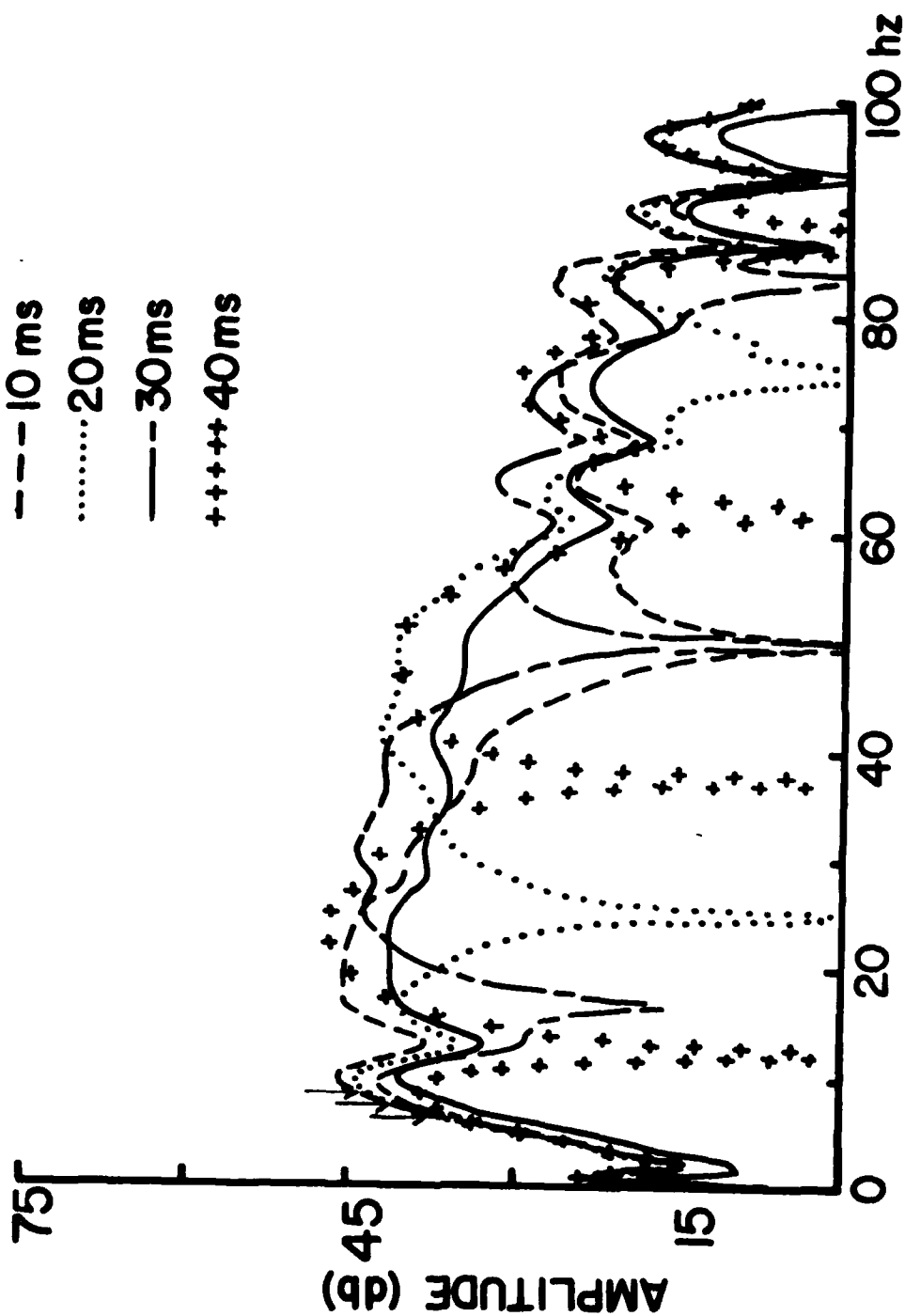


Figure 9

VERTICAL-at 420

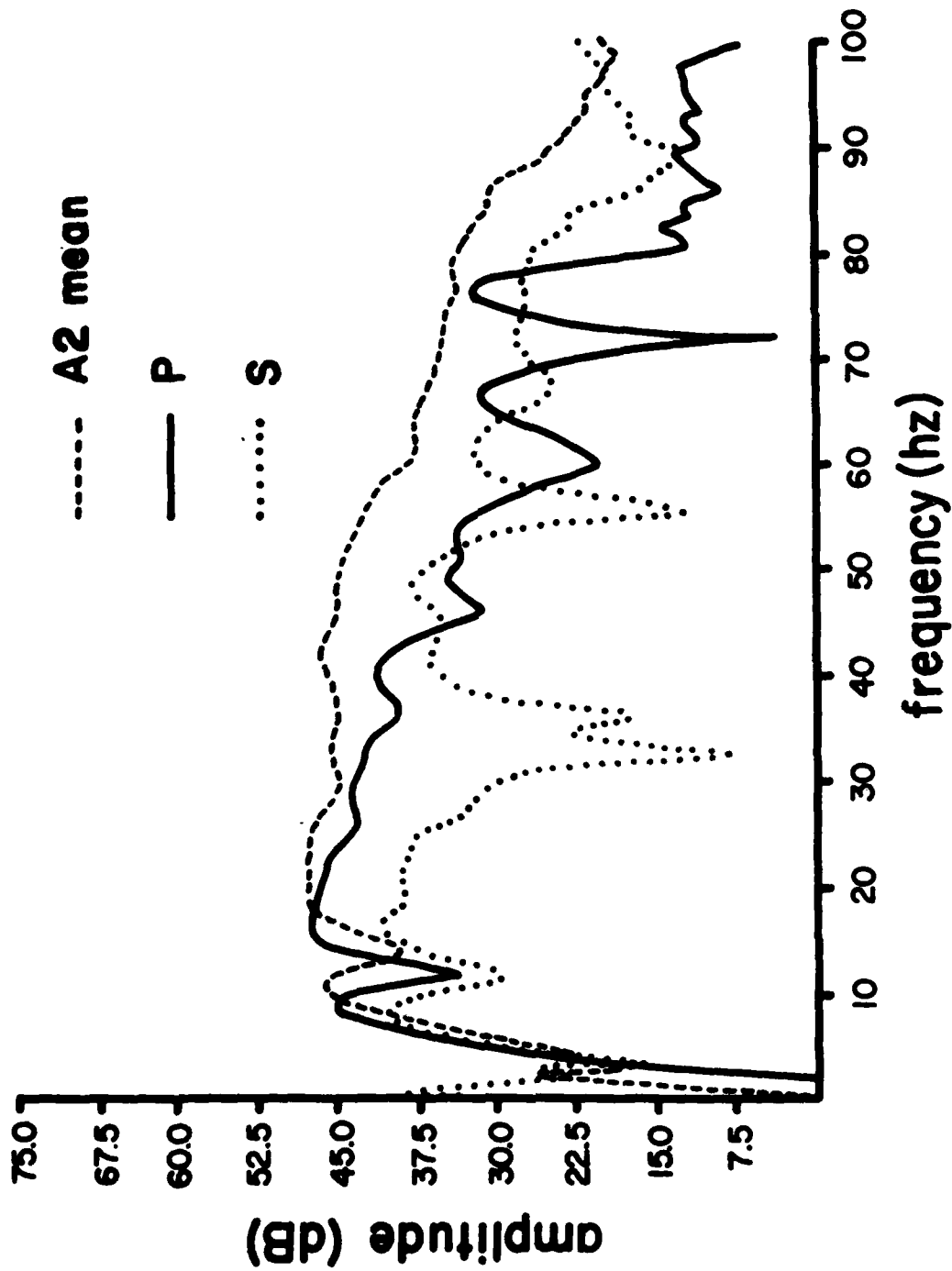


Figure 10a

VERTICAL-720

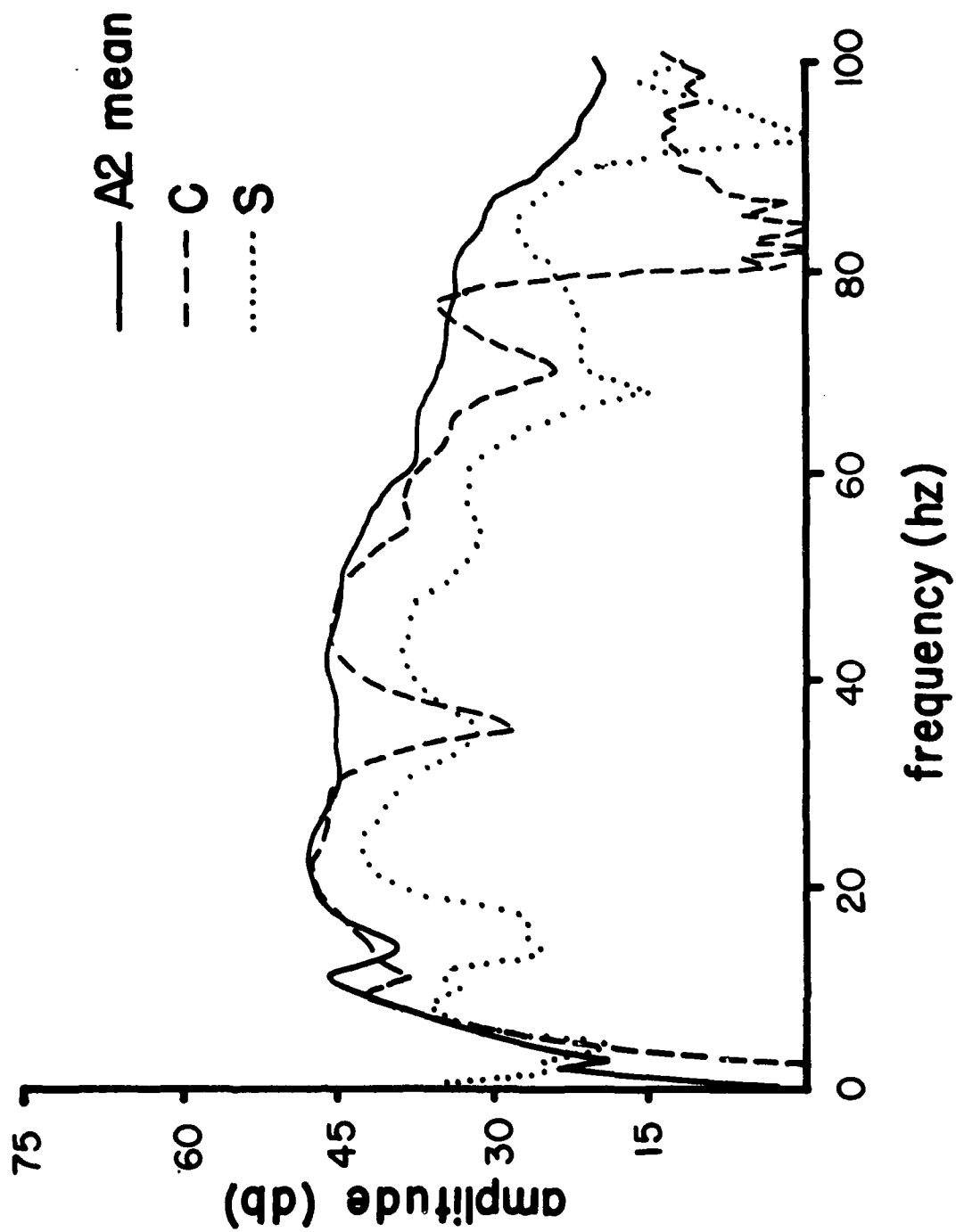


Figure 10b

EVENT 4 VERTICAL

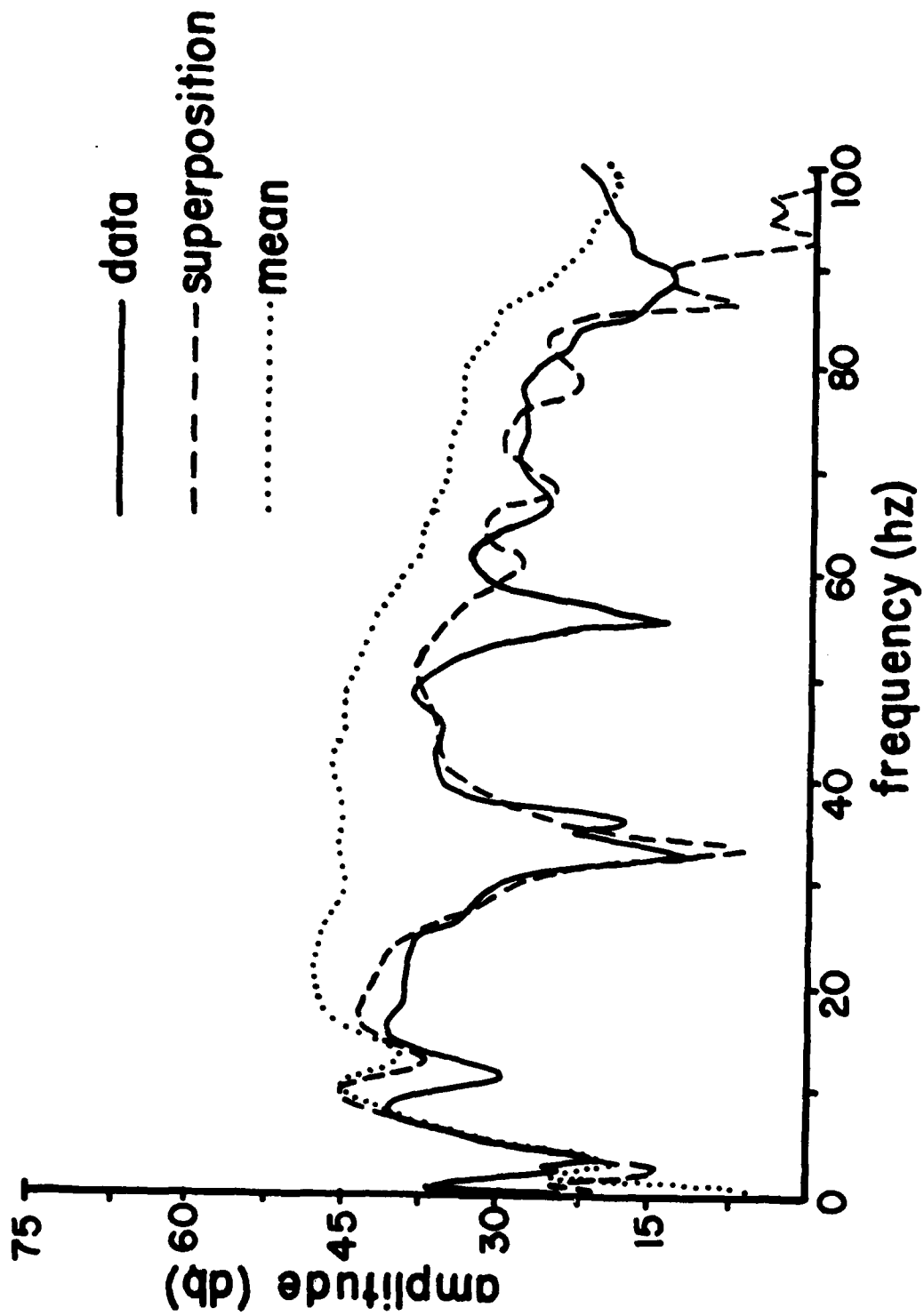


Figure 11

EVENT 7 VERTICAL

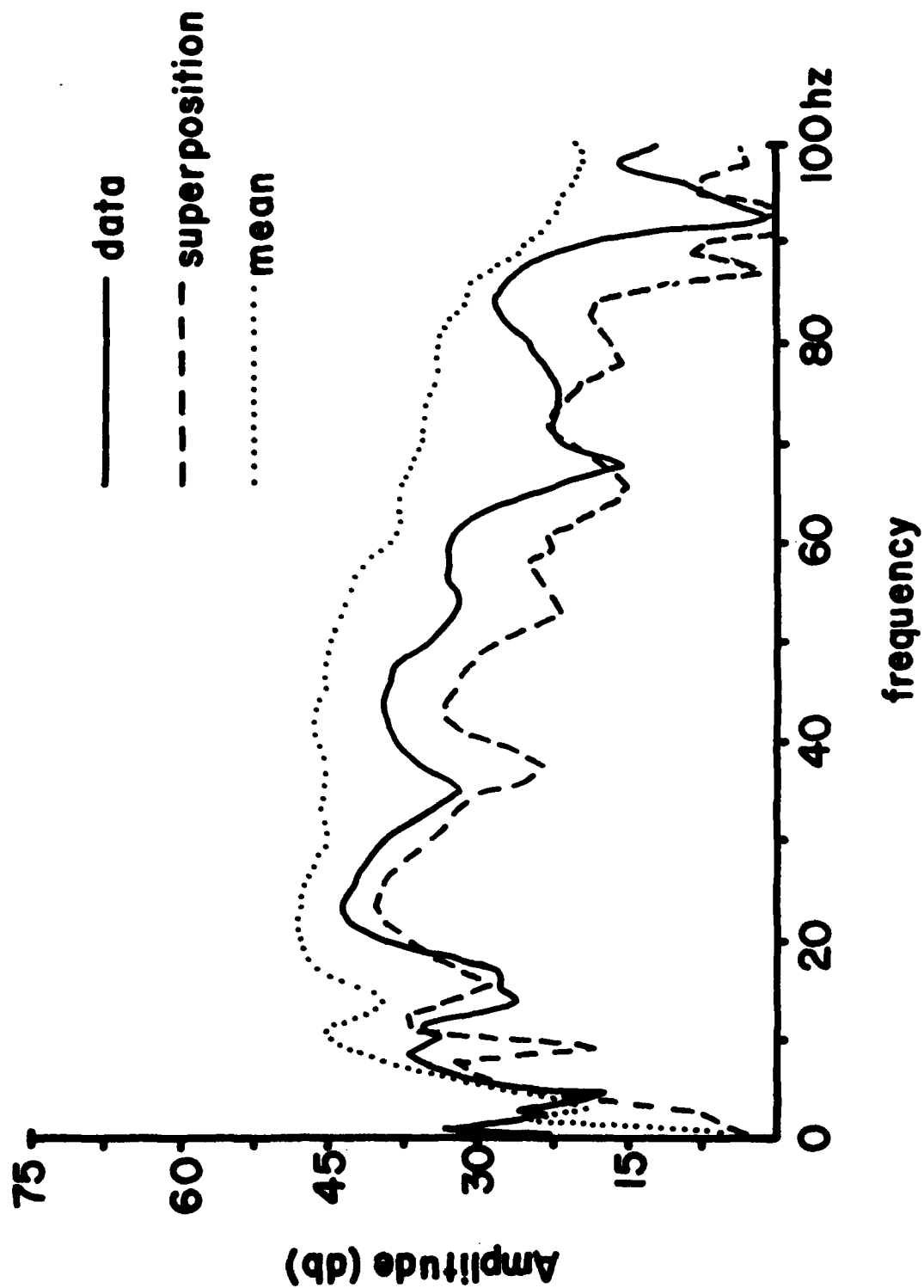


Figure 12

Table 1 (Values of $e^{-\pi ft/Q}$)

20M Range				
	Q	10	20	40
f				
35		.41	.64	.80
17.5		.64	.80	.89
8.75		.80	.89	.95

24M Range				
	Q	10	20	40
f				
35		.34	.50	.76
17.5		.58	.76	.87
8.75		.76	.87	.93

30M Range				
	Q	10	20	40
f				
35		.26	.51	.71
17.5		.51	.71	.84
8.75		.71	.84	.92

Ratio 24M/20M				
	Q	10	20	40
f				
35		.83	.91	.95
17.5		.91	.95	.98
8.75		.95	.98	.98

Ratio 30M/20M				
	Q	10	20	40
f				
35		.63	.78	.89
17.5		.79	.89	.94
8.75		.89	.94	.97

Acknowledgements

Part of support for B.W.S. came from the grant AFOSR-84-0016.